

INFORMATION TO USERS

This manuscript has been reproduced from the microfilm master. UMI films the text directly from the original or copy submitted. Thus, some thesis and dissertation copies are in typewriter face, while others may be from any type of computer printer.

The quality of this reproduction is dependent upon the quality of the copy submitted. Broken or indistinct print, colored or poor quality illustrations and photographs, print bleedthrough, substandard margins, and improper alignment can adversely affect reproduction.

In the unlikely event that the author did not send UMI a complete manuscript and there are missing pages, these will be noted. Also, if unauthorized copyright material had to be removed, a note will indicate the deletion.

Oversize materials (e.g., maps, drawings, charts) are reproduced by sectioning the original, beginning at the upper left-hand corner and continuing from left to right in equal sections with small overlaps.

ProQuest Information and Learning
300 North Zeeb Road, Ann Arbor, MI 48106-1346 USA
800-521-0600

UMI[®]

THE FLORIDA STATE UNIVERSITY

COLLEGE OF ARTS AND SCIENCE

EDDIES ALONG WESTERN BOUNDARIES

By

WILTON ZUMPICHIATTI ARRUDA

**A dissertation submitted to the
Department of Oceanography
in partial fulfillment of the
requirements for the degree of
Doctor of Philosophy**

**Degree Awarded:
Summer Semester, 2002**

UMI Number: 3061084

UMI[®]

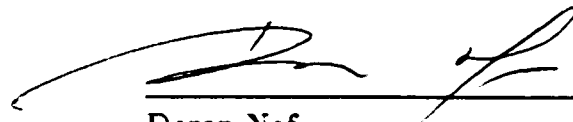
UMI Microform 3061084

Copyright 2002 by ProQuest Information and Learning Company.

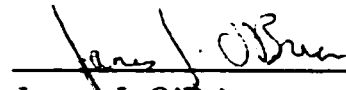
All rights reserved. This microform edition is protected against
unauthorized copying under Title 17, United States Code.

ProQuest Information and Learning Company
300 North Zeeb Road
P.O. Box 1346
Ann Arbor, MI 48106-1346

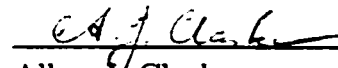
The members of the Committee approve the dissertation of Wilton Z. Arruda defended on July 10 2002.



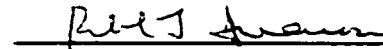
Doron Nof
Professor Directing Thesis



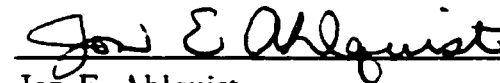
James J. O'Brien
Professor Co-Directing Thesis



Allan J. Clarke
Committee Member



Richard L. Iverson
Committee Member



Jon E. Ahlquist
Outside Committee Member

Approved:



David Thistle, Chair
Department of Oceanography

To My Wife Cristina and My Sons Gabriel and Rafael.

ACKNOWLEDGEMENTS

I would like to thank my major professor, Dr. Doron Nof, for suggesting this dissertation topic to me, and for his dedication and care to make this work meaningful. On every challenge during this work his comments taught me a lot of ocean dynamics. I thank my co-advisor Dr. James O'Brien for giving me the opportunity to come to Florida State and participate in the COAPS family. His guidance was essential during these four years. I thank to my committee members for their availability and comments. I thank Dr. Nobuo Sugimoto for his comments and careful reading of my manuscripts and for the discussions we had about various topics of physical oceanography. I would like also to thank Steve VanGorder for helping me with the numerical model code and all the COAPS computing people for making all necessary resources available to me.

Cristina, thanks for your patience for my endless hours of study. I could not have done it without you. Gabriel and Rafael thanks for the happiness I felt as I returned home each day.

My stay at Florida State University was supported by a scholarship from "Conselho Nacional de Desenvolvimento Científico e Tecnológico" (CNPq), of the Ministry of Science and Technology of Brazil. I am also grateful for a fellowship from Inter-American Institute for Global Change Research (IAI) through South Atlantic Climate Consortium (SACC).

TABLE OF CONTENTS

List of Tables	vii
List of Figures	viii
Abstract	x
1. INTRODUCTION	1
1.1 Objectives	1
1.2 The Present Work	1
2. THE ULLEUNG EDDY OWES ITS EXISTENCE TO β AND NONLINEARITIES	2
2.1 Introduction	2
2.1.1 Observational Background	2
2.1.1.1 The EKWC separation.	5
2.1.1.2 The EKWC and NKCC momentum fluxes.	6
2.1.1.3 The mechanism forcing the EKWC separation.	6
2.1.2 Objectives of the Present Study	8
2.2 Formulation	8
2.2.1 North-South Momentum Balance	10
2.2.2 Scaling	13
2.2.3 Solution	15
2.2.3.1 Zero potential vorticity boundary current.	15
2.2.3.2 Zero potential vorticity eddy.	16
2.2.3.3 Radius estimate.	18
2.3 Numerical Simulations	18
2.3.1 Numerical Model Description	19
2.3.2 General Results	21
2.4 The Linear Dynamics	26
2.4.1 Momentum Balance in the Whole Domain	28
2.4.2 The Interior Balance	29
2.4.3 The Western Boundary Layer Balance	29
2.5 Conclusions	30

3. THE MINDANAO AND HALMAHERA EDDIES ARE DUE TO THE BENDING OF THEIR PARENT CURRENTS, NONLINEARITIES AND β	32
3.1 Introduction	32
3.1.1 The Mindanao Current	34
3.1.2 Mindanao Eddy	34
3.1.3 The South Equatorial Current	35
3.1.4 The Halmahera Eddy	35
3.1.5 The Indonesian Throughflow	36
3.2 Flow in a Concave Solid Corner	39
3.2.1 Formulation	39
3.2.2 The f-plane Limit	42
3.2.3 The β -plane Limit	44
3.3 Numerical Simulations for a Flow in a Concave Solid Corner	44
3.3.1 Numerical Model Description	45
3.3.2 Northward Flowing WBC in a Concave Solid Corner	45
3.3.3 Southward Flowing WBC in a Concave Solid Corner	50
3.4 Estimates of the Eddy Radius Generated by a Flow in a Concave Solid Corner on a β -plane	54
3.4.1 Formulation	54
3.4.2 Northward Flowing WBC	55
3.4.2.1 Scaling	56
3.4.2.2 Expansions	57
3.4.2.3 Basic state for the northward flowing WBC and anticyclonic eddy	58
3.4.3 Southward Flowing WBC	60
3.5 The Collision Problem	62
3.5.1 Formulation	62
3.5.2 Numerical Simulations for the Collision Problem	66
3.6 The Western Equatorial Pacific	70
3.7 Conclusions	72
4. CONCLUSIONS	75
APPENDIX: LIST OF SYMBOLS AND ACRONYMS	76
REFERENCES	79
BIOGRAPHICAL SKETCH	88

LIST OF TABLES

2.1 List of experiments	21
3.1 List of experiments	46

LIST OF FIGURES

2.1 Schematic diagram of the Tsushima Warm Current (TWC) and the triple branch view with the first, second, and third branches	3
2.2 Bathymetry and horizontal temperature distribution at 200 m depth during July 8-15, 1989, showing the Ulleung Warm Eddy (UWE)	5
2.3 Schematic diagram of the separation of the EKWC (defined as an inflow) forced by the Tsugaru outflow on the eastern side of the basin. .	9
2.4 A close up of the region bounded by the dashed-dotted line in Fig. 2.3	11
2.5 Contour maps of the upper layer thickness nondimensionalized by $H = 300$ m for the f-plane run (experiment E3 in Table 2.1) at days: (a) 100; (b) 500; (c) 1000; (d) 3000	22
2.6 Snapshots at day 3000	23
2.7 Superposition of the 0.3 contours for the f-plane run (experiment E3 in Table 2.1) at day 100, 500, 1000, and 3000, showing the offshore movement of the system.	24
2.8 Estimate of the terms in the equation (2.31) from the experiment E1 (Table 2.1)	26
2.9 Estimates of the eddy radius	27
2.10 Schematic representation of the linear limit, i.e., here we take the boundary current to be a linear frictional current rather than inertial. .	28
3.1 The flow pattern in the western equatorial Pacific (adapted from Ffield and Gordon 1992)	33
3.2 Schematic diagram of the model	40
3.3 Schematic three-dimensional diagram of the upper layer thickness on the boundaries of a northward flowing western boundary current on an f-plane (upper panel) and on a β -plane (lower panel)	43
3.4 Upper layer thickness contours (upper left) and streamfunction contours (lower left) for the f-plane experiment E1 (Table 3.1) at day 2500; Upper layer thickness contours (upper right) and streamfunction contours (lower right) for the β -plane experiment E3 (Table 3.1) at day 25000. .	47

3.5	f-plane upper layer thickness h (in meters) along the western boundary (upper left) and along the zonal wall (lower left) at day 2500; β -plane upper layer thickness h (in meters) along the western boundary (upper right) and along the zonal wall (lower right) at day 25000.	48
3.6	Terms of the momentum balance (3.10) computed from the f-plane experiment E1 (upper panel), and the β -plane experiment E3 (lower panel)	49
3.7	Upper layer thickness contours (upper left) and streamfunction contours (lower left) for the f-plane experiment E2 (Table 3.1) at day 2500; Upper layer thickness contours (upper right) and streamfunction contours (lower right) for the β -plane experiment E4 (Table 3.1) at day 25000 ..	51
3.8	f-plane upper layer thickness h (in meters) along the western boundary (upper left) and along the zonal wall at day 2500; β -plane upper layer thickness along the western boundary (upper right) and the zonal wall (lower right) at day 25000.	52
3.9	Terms of the momentum balance (3.11) computed from the f-plane experiment E2 (upper panel), and the β -plane experiment E4 (lower panel)	53
3.10	Schematic representation of a radial section of the Csanady (1979) cyclonic eddy.	61
3.11	Schematic diagram of the collision between a northward flowing boundary current (Main current) and a southward flowing boundary current (Counter current) on a β -plane	63
3.12	Upper layer thickness contours (left panel) and streamfunction contours (right panel) for the collision experiment E8 (Table 3.1) on a β -plane at day 2500.	67
3.13	Upper layer thickness h (in meters) along the western boundary (upper panel) and along the offshore branch of $\psi = 0$ (lower panel) for the collision experiment E8 at day 2500.	68
3.14	Momentum balance (3.38) for area containing both colliding currents (upper panel); Momentum balance (3.39) for the area south of the zero streamfunction (middle panel); Momentum balance (3.40) for the area north of the zero streamfunction (lower panel). All terms were computed from experiment E8.	69
3.15	Schematic representation of the convergence of the Mindanao Current (MC) and South Equatorial Current (SEC)	71

ABSTRACT

The Ulleung eddy owes its existence to β and nonlinearities: A nonlinear theory for the generation of the Ulleung Warm Eddy (UWE) (formed close to the separation of the East Korea Warm Current in the Japan/East Sea) is proposed. Using the nonlinear reduced gravity (shallow water) equations, it is shown analytically that the eddy is established in order to balance the northward momentum flux exerted by the separating western boundary current. In this scenario the presence of β produces a southward (eddy) force balancing the northward momentum flux imparted by the separating East Korean Warm Current.

The solution is derived using an expansion in powers of $\epsilon^{1/6}$ (here $\epsilon = \beta R_d / f_0$ where R_d is the Rossby radius based on the undisturbed upper layer thickness H). It is found that, for a high Rossby number western boundary current (i.e., highly nonlinear current) the eddy radius is roughly $2R_d/\epsilon^{1/6}$ implying that the UWE has a scale larger than that of most eddies (R_d). This solution shows that, in contrast to the familiar idea attributing the formation of eddies to instabilities (i.e., the breakdown of a known *steady* solution), the UWE is an integral part of the *steady* stable solution.

A reduced gravity numerical model is used to further analyze the relationship between beta, nonlinearity and eddy formation. First, we show that high Rossby number western boundary current which is forced to separate from the wall on an f-plane does not produce an eddy near the separation. To balance the northward momentum force imparted by the nonlinear boundary current the f-plane system moves offshore producing a southward Coriolis force. We then show that as, β is introduced to the problem, an anticyclonic eddy is formed. The numerical balance of

forces shows that, as suggested by the analytical reasoning, the southward force produced by the eddy balances the northward force imparted by the boundary current. We also found that the observed eddy scale in the Japan/East Sea agrees with the analytical and numerical estimate for a nonlinear current.

The Mindanao and Halmahera eddies are due to the bending of their parent currents, nonlinearities and β : Starting with the simple case of a northward (southward) western boundary current (WBC) flowing along a concave solid boundary with a sharp corner on an β -plane, it is shown that an anticyclonic (cyclonic) eddy is established to balance the upstream momentum flux. (On an f -plane no eddy is established because a pressure force which balances the WBC momentum flux is generated.) The solution is derived by expanding the dependent variables in powers of $\epsilon^{1/6}$ for the northward current (anticyclonic eddy) and $\epsilon^{1/2}$ for the southward current (cyclonic eddy). Here $\epsilon = \beta R_d / f_0$, where R_d is the Rossby radius based on the undisturbed upper layer thickness H . It is found that, for a high Rossby number (i.e., highly nonlinear current), the length scales are $R_d / \epsilon^{1/6}$ and $R_d / \epsilon^{1/2}$ for the anticyclonic and cyclonic eddies (respectively) implying that these eddies are larger than most eddies in the ocean (which scale with R_d). A reduced gravity numerical model is used to validate these analytical results. The balance of forces and the eddy size estimates (derived from the numerical simulations) agree with the analytical results.

With the aid of the above analysis we then examine the collision of two opposing western boundary currents on a β -plane. It is shown that this problem can be conceptually reduced to the above problem of two WBCs turning in a solid corner on a β -plane where the streamline separating the two colliding currents acts like a “zonal wall.” We show that an eddy is established (to balance the momentum flux of the respective WBC) on each side of the dividing streamline. Comparison of the analytical momentum balances and the eddy radius estimates with those derived from a numerical model show that the two are in very good agreement.

Based on the above collision problem, an explanation for the generation of the Mindanao and Halmahera eddies in the equatorial western Pacific is proposed. It is argued that these eddies are required to balance the nonlinear momentum fluxes of their colliding parent currents, the southward flowing Mindanao Current (MC) and the northward flowing South Equatorial Current (SEC). Hellerman and Rosenstein wind stress is used to estimate the offshore thickness and the radii of the Mindanao and Halmahera eddy. The obtained values are in excellent agreement with observations.

CHAPTER 1

INTRODUCTION

1.1 Objectives

The objective of this study is to explain the existence of permanent eddies associated with: (a) Separation of a western boundary current (WBC) from the coast in absence of any opposing current. Observations off East Australia Current and numerical simulations (Olson, 1991) suggest the formation a permanent eddy so-called “intrusion eddy”. (b) Collision of opposing western boundary currents forming a joined eastward flowing current. This process would lead to the formation of an anticyclonic eddy on the northward flowing WBC side and a cyclonic eddy on the southward flowing WBC side.

1.2 The Present Work

Even though the Chapters are related we chose to write them in a self-contained form, what makes the presentation clearer.

In Chapter 2 we present a nonlinear theory for the generation of the Ulleung Warm eddy attached to the separating East Korea Warm Current in the Japan/East Sea. The Ulleung Warm eddy is a typical case of “intrusion eddy”. In Chapter 3 we present a nonlinear theory for the generation of the Mindanao and Halmahera eddies in the equatorial western Pacific asociated with the collision of two opposing western boundary currents: The southward flowing Mindanao Current and the northward flowing South Equatorial Current. In Chapter 4 we presents the conclusions.

CHAPTER 2

THE ULLEUNG EDDY OWES ITS EXISTENCE TO β AND NONLINEARITIES

2.1 Introduction

The Japan/East Sea (JES) is a part of a chain of marginal seas adjacent to the northwestern Pacific. It is a deep semi-enclosed sea bounded by the Japanese Islands, the Korean Peninsula, and the Asian continent. With dimensions of about 1600×900 km and a maximum depth about 3700 m, it contains large-scale circulation features resembling those in major ocean basins (e.g., cyclonic and anticyclonic gyre systems and deep homogeneous water mass). The JES also contains wind-driven and thermohaline-driven circulation, deep convection, ice-sea interactions, and mesoscale circulation features. Here, we focus on one of the most prominent features of the JES, the Ulleung Warm Eddy (UWE).

2.1.1 Observational Background

The northward flowing Tsushima Warm Current (TWC) has a major impact on the hydrography and circulation in the JES. Its minimum transport is in the summer-autumn, with an annual mean of 2 Sv and a seasonal variation of about 1.3 Sv (peak to peak) [Preller and Hogan 1998]. Perkins et al. (2000) and Jacobs et al. (2001) verified the earlier ideas that, within the Tsushima Strait, the TWC is divided into two different currents, one flowing through the eastern channel and the other through the western channel. This so-called “primary branching”

(**Fig. 2.1**) is thought to be due to the Tsushima Island and the topography but Ou (2001) proposed an alternative splitting mechanism. According to the classical interpretation of Suda and Hidaka (1932) and Uda (1934), the northern part of the TWC ultimately splits again forming a total of three distinct branches (**Fig. 2.1**) originally named (from east to west) first, second and third branches. The structure

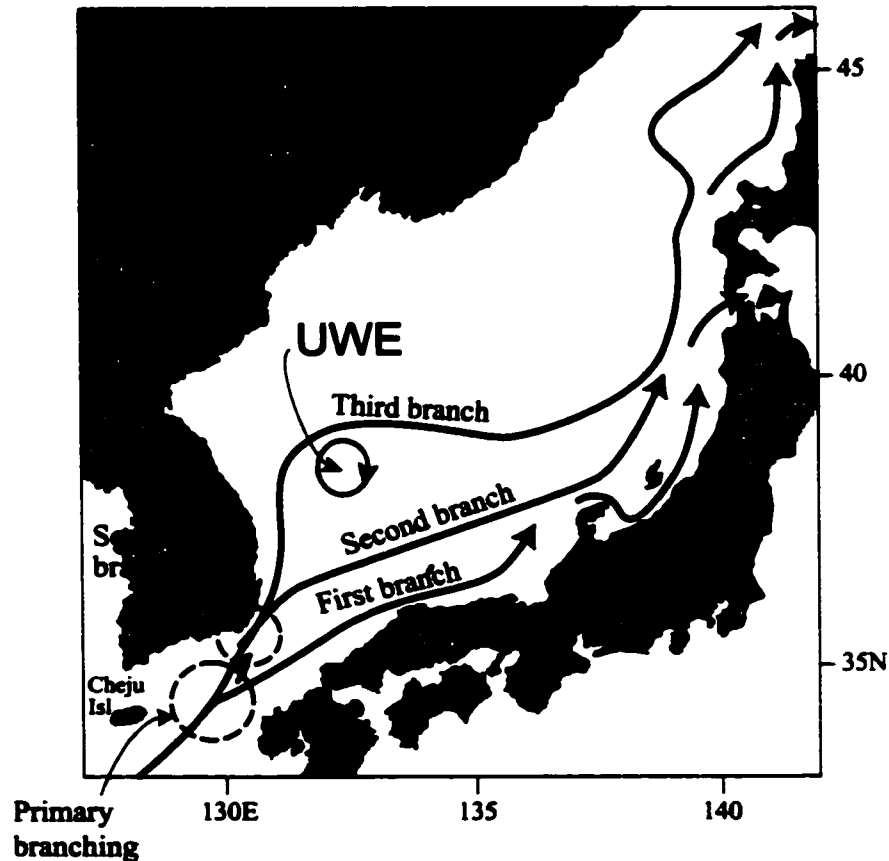


Figure 2.1. Schematic diagram of the Tsushima Warm Current (TWC) and the triple branch view with the first, second, and third branches [sometimes referred to as the East Korean Warm Current (EKWC)]. The broken circles show the splitting of the TWC and the closed circle represents the Ulleung Warm Eddy (UWE). (Adapted from Preller and Hogan 1998)

and variability of the TWC were studied using a variety of data sets: hydrographic (Kawabe 1982a; Lie 1984; Lie and Byun 1985; Kim and Kim 1983; Katoh 1994; Preller and Hogan 1998), satellite-derived sea-surface temperature (SST) (Kim and

Legeckis 1986; Cho and Kim 1996), and numerical models experiments (Kawabe 1982b; Hogan and Hurlburt 2000).

For clarity we shall refer to the East Korean Warm Current (EKWC) as the "third branch" of the TWC. The EKWC flows northward along the continental slope off the east coast of Korea up to about 37-38°N, where it meets the much weaker southward-flowing North Korea Cold Current (NKCC) (Suda and Hidaka 1932; Kim and Kim 1983; Kim and Legeckis 1986). At the confluence, the currents separate from the coast and flows east-northeast toward the Tsugaru Strait. This separation appears to be analogous to the classical western boundary current separation which occurs around 37-38°N (e.g. Gulf Stream), but it is probably forced by the Tsugaru strait outflow situated to the east.

Using ADCP (Acoustic Doppler Current Profiler) data, Katoh (1994) estimated that the transport of the EKWC amounted to about 1.54 Sv in June 1998, 0.70 Sv in August 1998, and 1.77 Sv in June 1989. Tanioka (1968) argues that 80-90% of the volume transport of the EKWC returns southward around Ulleung Island forming the Ulleung Warm Eddy (UWE) (Ichiye and Takano 1988; Kang and Kang 1990; Kim et al. 1991; Katoh 1994). The UWE is located in the central part of the Ulleung Basin (where the depth exceeds 1500 m) and has a diameter of approximately 150 km (Fig. 2.2).

Lim and Kim (1995) argued that topography is controlling the eddy's position, and Isoda and Saitoh (1993) reported the formation of a large-scale northward flow near the Korean coast when the eddy approaches the western slope of the continental margin. However, the eddy does not always migrate. Using satellite-tracked drifters, Lie et al. (1995) showed that the eddy was almost stationary from December 1992 to September 1993. They also suggested that the EKWC splits further into two parts: the main stream, which meanders around Ulleung Island, and a branch flowing northeast along the Korean coast. Besides the UWE, the JES shows a high eddy activity and various studies examined the horizontal eddy scales in the basin (Toba

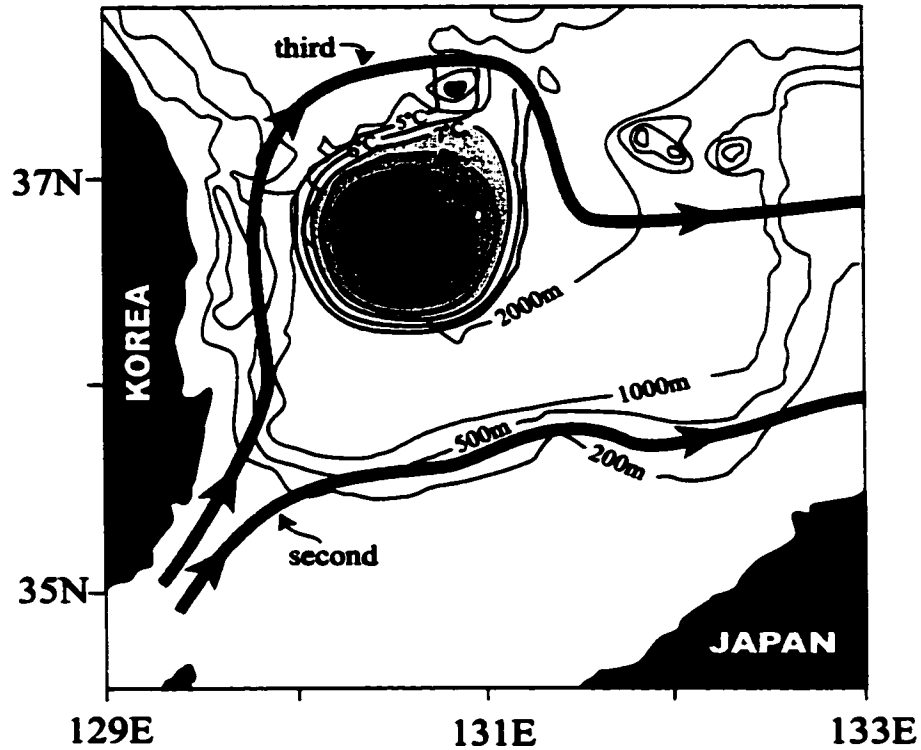


Figure 2.2. Bathymetry and horizontal temperature distribution at 200 m depth during July 8-15, 1989, showing the Ulleung Warm Eddy (UWE). The temperature contour interval is 1°C. The arrowed lines show the third branch (EKWC) and the second branch. (Adapted from Lim and Kim 1995)

et al. 1982; Kim and Legeckis 1986; Ichiye and Takano 1988; Tameishi 1987; Isoda and Nishihara 1992; Sugimoto and Tameishi 1992; Matsuyama et al. 1990; Miyao 1994).

2.1.1.1 The EKWC separation. Our aim is to provide an explanation for the establishment of the UWE. To do so we shall assume that the EKWC leaves the coast due to a vanishing thermocline depth induced by the Tsugaru outflow to the East. There have been numerous studies of western boundary current separation and the reader is referred to: Parsons (1969), Veronis (1973), Huang and Flierl (1987), and Dengg et al. (1996). Two related aspects need to be addressed here. First, we shall examine the issue of whether the momentum flux of the opposing NKCC is

negligible and, second, we shall show that the outflow through the Tsugaru strait in the eastern JES is most likely the cause of the separation.

2.1.1.2 The EKWC and NKCC momentum fluxes. We shall neglect the momentum flux of the NKCC on the ground that it is small in most of the time when compared with the momentum flux of the EKWC. To see this we note that the momentum flux of each boundary current can be approximated as

$$\int_0^\infty h v^2 dx \simeq \bar{v} \int_0^\infty h v dx , \quad (2.1)$$

where \bar{v} and $\int_0^\infty h v dx$ are the average speed and the transport over the boundary current respectively. Observations (Gordon 1990; Preller and Hogan 1998; Rostov et al. 2001) suggest that on average, the EKWC has a transport of ~ 1.5 Sv and a speed of ~ 25 cm s $^{-1}$ while the NKCC has a transport of ~ 0.5 Sv and a speed ~ 5 cm s $^{-1}$. This gives a momentum flux ratio of 1/15 indicating that the momentum flux of the NKCC is usually negligible. Note, however, that these values change on various time spans and that, consequently, the momentum flux of NKCC is not always negligible. Using ADCP data collected during June-July 1999, Ramp et al. (2002) computed a transport of 1.45 Sv and a momentum flux of 2.27×10^5 m 4 s $^{-2}$ for the EKWC and a transport of 0.78 Sv and a momentum flux of 1.59×10^5 m 4 s $^{-2}$ for the NKCC. This gives a ratio of 0.7 for the momentum fluxes which is clearly not negligible. It is important to realize that, for the time period considered by Ramp et al. (2002) no UWE was observed. Consequently, they could apply the theory for the collision of boundary currents on an f-plane (Agra and Nof 1992) and conclude that the separated current should leave the coast at a calculated angle of 80° which was in very good agreement with their observations.

2.1.1.3 The mechanism forcing the EKWC separation. To see that, for most of the year, the wind stress (which is the classical force associated with separation) may not play an important role in the EKWC separation, consider the

depth integrated linear reduced gravity x -momentum equation,

$$-fV = -\frac{g'}{2} \frac{\partial(h^2)}{\partial x} + \frac{\tau^x}{\rho}, \quad (2.2)$$

where h is the upper layer thickness, V is the vertically integrated velocity component in the y direction, g' the reduced gravity, τ^x the zonal wind stress component (assumed to be a function of y only) and ρ is the upper layer density. Integrating (2.2) zonally across the basin and temporality assuming that there is no net meridional volume transport through the section (i.e., no “sink”), we have

$$h_{eb}^2 - h_{wb}^2 = \frac{2\tau^x}{\rho g'} L_e,$$

where h_{wb} and h_{eb} are the wind induced upper layer thicknesses on the western boundary and eastern boundary respectively, and L_e is the basin length. At the separation latitude $h_{wb} = 0$, so

$$h_{eb} = \left(\frac{2\tau^x}{\rho g'} L_e \right)^{1/2}. \quad (2.3)$$

Using (2.3) and the climatological Hellerman-Rosenstein zonal wind stress for 37° N, we can calculate monthly values for the no-sink wind-induced upper layer thickness h_{eb} . From November to March the average zonal wind stress is high (0.78 dyn cm⁻² for January) giving a mean value of 57 m for h_{eb} . For the rest of the year the average zonal wind stress is much weaker (giving h_{eb} of 10 m for April) and even negative from May to October. According to Chu et al. (2001), the the upper layer thickness on the eastern boundary is between 150 and 200 m from November to April, indicating that, even during the strong wind stress period, the calculated h_{eb} is too small. We conclude that the JES has a too short zonal width to accommodate a separation of the EKWC by the wind stress, indicating that the Tsugaru strait outflow is the main mechanism responsible for the EKWC separation.

2.1.2 Objectives of the Present Study

Observations off the East Australia Current and numerical simulations of the Brazil Current (Olson 1991) suggest that the separation mechanism of a western boundary current leads to the formation of an “intrusion eddy”¹. In what follows we shall argue that the UWE belongs to the same category. The identification of physical mechanism responsible for the existence of the intrusion eddy is the focus of this paper.

This paper is organized as follows: In section 2 we derive an analytical relationship that represents the balance of forces in a control region surrounding the eddy. In section 3 we derive an estimate for the eddy radius based on the relation found in section 2. In section 4 we describe the comparison between the analytical results from the previous sections and the outputs of a numerical model. In section 5 we investigate the linear limit and in section 6 we discuss the results and present the conclusions.

2.2 Formulation

We shall study the “intrusion eddy” (formed when a western boundary current separates from the coast due to an outflow east of the boundary) in the framework of a baroclinic reduced gravity model on a β -plane (**Fig. 2.3**). Though the wind stress and the ocean interior are responsible for the existence of the western boundary current in the ocean, we assume that their role in the dynamics of the eddy is minor, because the length scale of the wind systems is much greater than that of the boundary current [$\sim O(R_d)$].

Consider a single northward flowing western boundary current in an upper layer (with density ρ) above an infinitely deep layer of slightly denser water (with density

¹This term was first used by Olson (1991) to describe an eddy associated with a western boundary current separation.

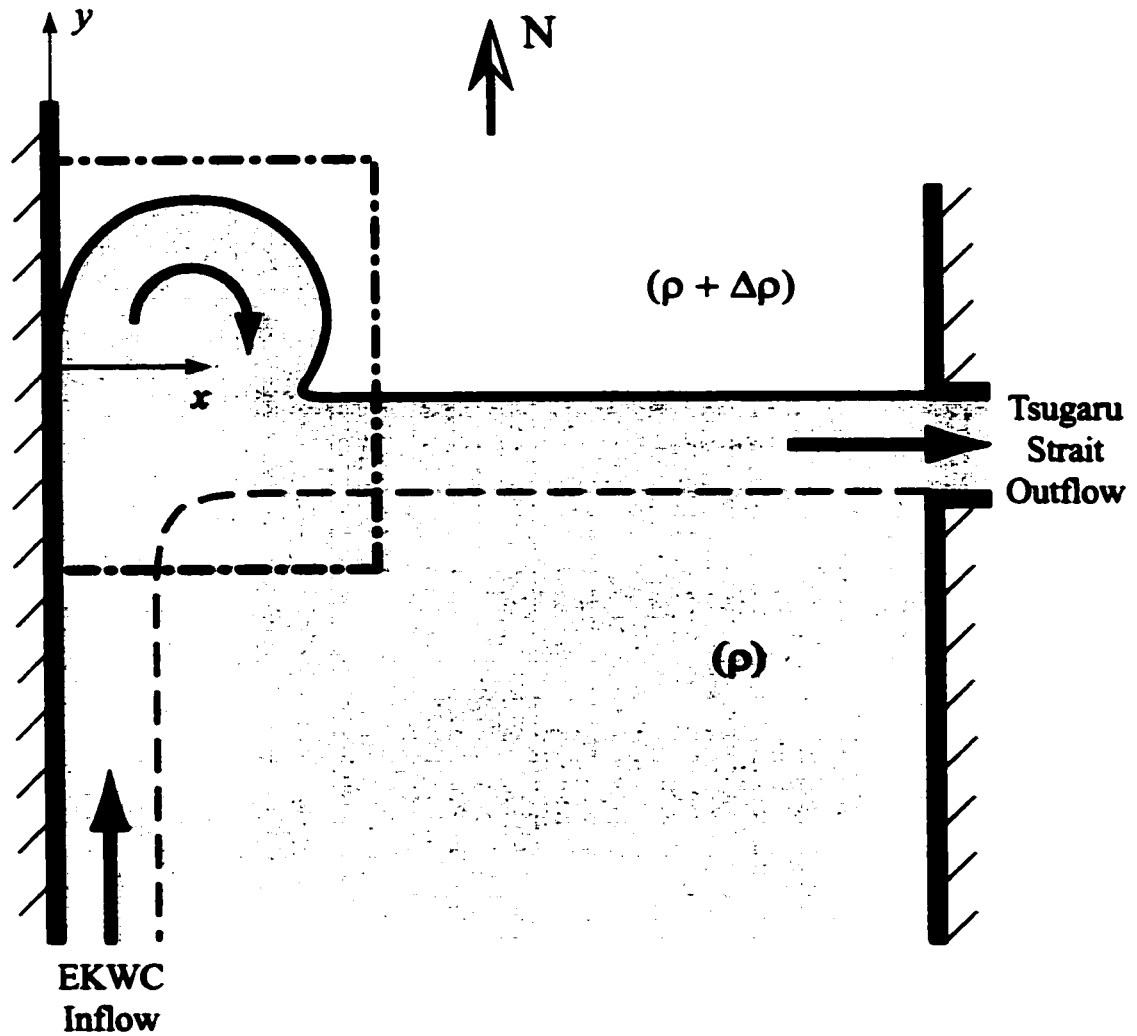


Figure 2.3. Schematic diagram of the separation of the EKWC (defined as an inflow) forced by the Tsugaru outflow on the eastern side of the basin. The shaded area represents the region where the lighter layer is present. The origin of the coordinate system is situated at the separation point. A close up of the region bounded by the dashed-dotted line is shown in Fig. 2.4.

$\rho + \Delta\rho$). As the current flows northward it reaches a latitude where the upper layer thickness vanishes on the wall due to the outflow to the east and, consequently, a separation takes place. We place the origin of our coordinate system right on separation point on the wall and assume that far away from the western boundary and far south from the separation latitude the upper layer thickness approaches an undisturbed value H . As alluded to earlier the effects of an opposing southward flowing boundary current are neglected.

The separated current forms a front where the outcropping streamline divides the domain into two sections. Both layers are present in the southern part of the basin but only one (the motionless denser layer) is present in the northern part. As we shall see later, it will not be necessary for us to derive the solution for the entire region and the separation point because we shall use an integrated approach which that avoids need. A schematic diagram of our domain of study is depicted in **Fig. 2.4**.

2.2.1 North-South Momentum Balance

Assuming a steady state and integrating (after multiplying by h) the steady and inviscid nonlinear y -momentum equation,

$$u \frac{\partial v}{\partial x} + v \frac{\partial v}{\partial y} + f u + g' \frac{\partial h}{\partial y} = 0,$$

over the fixed region S bounded by the dashed line $ABCD$ A shown in **Fig. 2.4**, we get

$$\begin{aligned} \iint_S \left(hu \frac{\partial v}{\partial x} + hv \frac{\partial v}{\partial y} \right) dx dy + \iint_S (f_0 + \beta y) u h dx dy \\ + \frac{g'}{2} \iint_S \frac{\partial(h^2)}{\partial y} dx dy = 0, \end{aligned} \quad (2.4)$$

which, by using the continuity equation and stream function ψ , can be reduced to

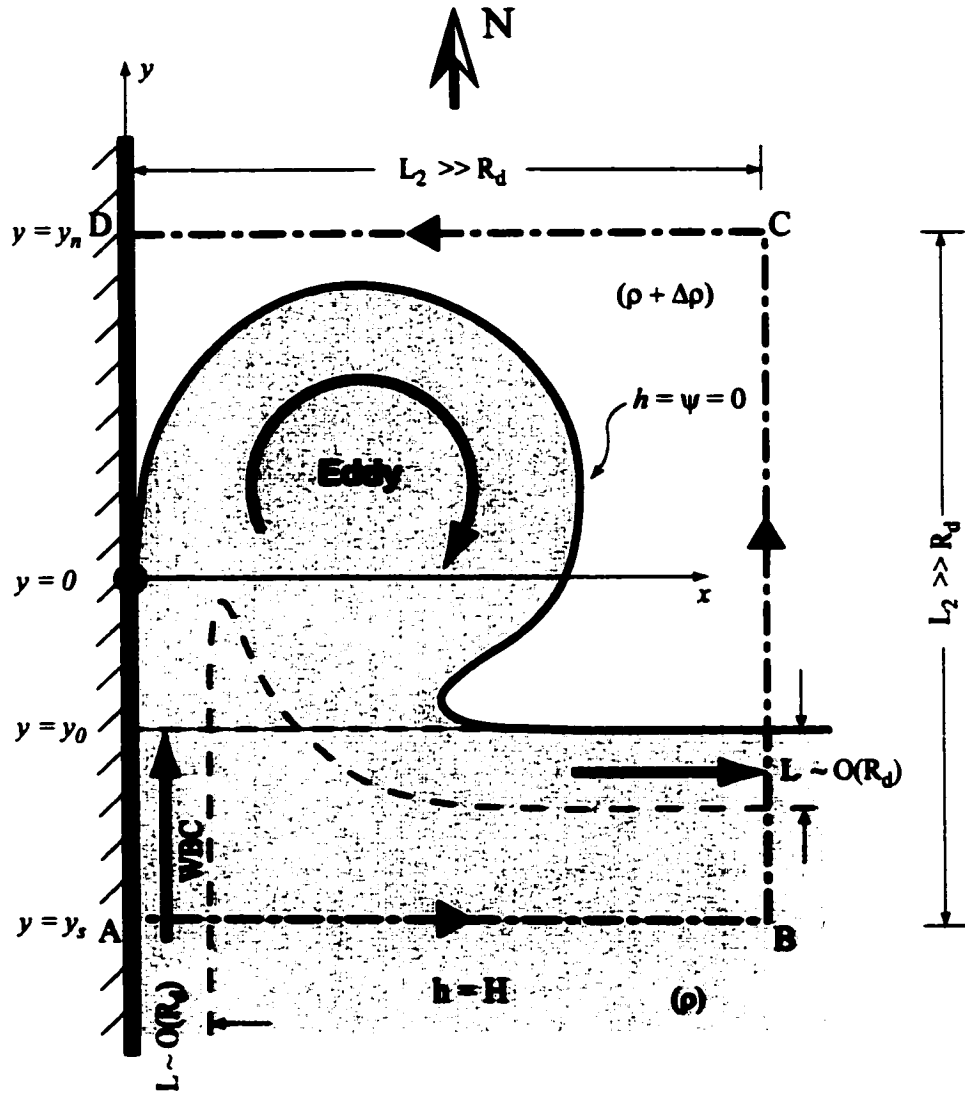


Figure 2.4. A close up of the region bounded by the dashed-dotted line in **Fig. 2.3**. A northward flowing western boundary current (WBC) [with width of $O(R_d)$] in a layer of density ρ separates from the coast and forms an intrusion eddy. After the fluid circles within the eddy it flows zonally eastward. H is the undisturbed upper layer thickness at the basin interior. It will be shown that the eddy scale is of $O(R_d/\epsilon^{1/6})$ and that the momentum imparted on the region bounded by $ABCD$ through AB by the boundary current is balanced by the β -induced force of the anticyclonic eddy.

$$\iint_S \left[\frac{\partial(huv)}{\partial x} + \frac{\partial(hv^2)}{\partial y} \right] dx dy - \iint_S (f_0 + \beta y) \frac{\partial \psi}{\partial y} dx dy + \frac{g'}{2} \iint_S \frac{\partial(h^2)}{\partial y} dx dy = 0. \quad (2.5)$$

Here, the notation is conventional, that is, u and v are the velocity components in the x and the y direction, h is the upper layer thickness, ψ is the transport stream function defined by $\partial \psi / \partial y = -uh$; $\partial \psi / \partial x = vh$, and g' is the reduced gravity, $g\Delta\rho/\rho$ (for convenience variables are defined both in the text and in Appendix).

Eq. (2.5) can be rewritten as,

$$\iint_S \left[\frac{\partial(huv)}{\partial x} + \frac{\partial(hv^2)}{\partial y} \right] dx dy - \iint_S f_0 \frac{\partial \psi}{\partial y} dx dy - \iint_S \left[\frac{\partial(\beta y \psi)}{\partial y} - \beta \psi \right] dx dy + \frac{g'}{2} \iint_S \frac{\partial(h^2)}{\partial y} dx dy = 0, \quad (2.6)$$

and application of Green's theorem gives

$$\oint_{\partial S} huv dy - \oint_{\partial S} \left(hv^2 + \frac{g'h^2}{2} \right) dx + f_0 \oint_{\partial S} \psi dx + \beta \oint_{\partial S} y \psi dx + \beta \iint_S \psi dx dy = 0, \quad (2.7)$$

where ∂S is the boundary of S .

Next, we assume that $\psi = 0$ along the wall and on the outcropping front and note that at least one of the three variables h , u , and v vanishes on every portion of the boundary ∂S . It then follows from (2.7) that

$$\int_A^B \left[hv^2 + \frac{g'h^2}{2} - (f_0 + \beta y)\psi \right] dx - \beta \iint_S \psi dx dy = 0. \quad (2.8)$$

Assuming now that the flow is geostrophic in the cross-current direction, we get [after multiplying the geostrophic relation $(f_0 + \beta y)v = g'\partial h/\partial x$ by h and integrating on the segment AB],

$$(f_0 + \beta y)\psi + C = \frac{g'}{2}h^2, \quad (2.9)$$

where C is the constant to be determined. Note that at $x \rightarrow \infty$ the zonal flow is geostrophic in the y direction so that

$$(f_0 + \beta y)uh = -\frac{g'}{2} \frac{\partial(h^2)}{\partial y},$$

and an integration in y gives,

$$(f_0 + \beta y)\psi \Big|_{y_s}^{y_n} - \beta \int_{y_s}^{y_n} \psi_\infty dy = \frac{g'}{2} h^2 \Big|_{y_s}^{y_n}, \quad x \rightarrow \infty$$

where ψ_∞ (which is a function of y) is the stream function at $x \rightarrow \infty$, and y_s and y_n are the y -components of points A and D (**Fig. 2.4**) respectively. Since $\psi = h = 0$ at $y = y_n$ it follows that $C = \beta \int_{y_s}^{y_n} \psi_\infty dy$ so that (2.8) can be written as,

$$\int_0^L h v^2 dx - \beta \iint_S (\psi - \psi_\infty) dx dy = 0, \quad (2.10)$$

where L is the width of the boundary current. Note that the integrand of the second integral vanishes as $x \rightarrow \infty$ and, consequently, the integral does not change when the zonal extent of S is increased (as should be the case).

Let y_0 be the latitude where $\psi_\infty = 0$. Then, from (2.9)

$$\int_0^L h v^2 dx - \beta \iint_{S^+} \psi dx dy - \beta \iint_{S^-} (\psi - \psi_\infty) dx dy = 0, \quad (2.11)$$

where S^+ and S^- are subsets of S corresponding to $y > y_0$ and $y \leq y_0$, respectively.

We shall now leave (2.11) temporarily aside and discuss the relevant scales.

2.2.2 Scaling

Assuming nonlinear dynamics we take the following scales:

$$L \sim O(R_d); \quad v \sim O((g'H)^{1/2});$$

$$\psi \sim O\left(\frac{g'H^2}{f_0^2}\right) \text{ outside the eddy; } \psi \sim O\left(\frac{g'H_e^2}{f_0^2}\right) \text{ inside the eddy,}$$

where $R_d = (g'H)^{1/2}/f_0$ is the Rossby radius of deformation, and $H_e \gg H$ is the depth scale for the eddy.

Note that the integrand of the third term in (2.11) is zero in the area outside the currents so each term of (2.11) can be scaled as,

$$\int_0^L hv^2 dx \sim O(g'H^2 R_d) \quad (2.12)$$

$$\beta \iint_{S^-} (\psi - \psi_\infty) dx dy \sim O\left(\beta R_d L_2 \frac{g'H^2}{f_0}\right) \quad (2.13)$$

$$\beta \iint_{S^+} \psi dx dy \sim O\left(\beta R_{de}^2 \frac{g'H_e^2}{f_0}\right), \quad (2.14)$$

where $R_{de} = (g'H_e)^{1/2}/f_0$, $|y_s| = L_2 \gg R_d$, and L_2 is the length of the integration domain $ABCD$ (**Fig. 2.4**). Note that the ratio between (2.13) and (2.12) is $\beta L_2/f_0 \ll 1$. Consequently, the only term that can balance the momentum flux (2.12) is the β term (2.14). Taking

$$R_{de} \sim O\left(\frac{R_d}{\epsilon^{1/6}}\right), \text{ and} \quad (2.15)$$

$$L_2 \sim O(R_{de}), \quad (2.16)$$

where $\epsilon = \beta R_d/f_0 \ll 1$, we have a balance between (2.12) and (2.14) and the ratio between (2.12) and the two other terms is $O(\epsilon^{5/6})$.

Two comments should be made with regard to (2.14). First, as is frequently the case, the scaling may conceal potentially large numbers such as powers of the known $2\sqrt{2}$ ratio between the eddy radius and the Rossby radius (see, e.g. Nof 1981; Killworth 1983). Second, the $1/6$ power of ϵ implies that, for most cases [$\epsilon \sim O(0.1)$], R_{de} will be comparable to R_d (though it will be somewhat larger).

2.2.3 Solution

The scale analysis performed in the last section shows that the leading order nonlinear balance is,

$$\int_0^L h v^2 dx = \beta \iint_{S^+} \psi dx dy . \quad (2.17)$$

To find an estimate for the eddy radius, we shall first look at the case where both the eddy and the western boundary current have zero potential vorticity, i.e., the highly nonlinear case. Note that this zero potential vorticity limit makes the solutions for the boundary current and the eddy straightforward despite the nonlinearity. We shall see later that, for this limit, we obtain a lower bound estimate for the eddy radius.

2.2.3.1 Zero potential vorticity boundary current. For a zero-pv northward flowing boundary current,

$$v = \begin{cases} f(L-x) & , \quad x \leq L \\ 0 & , \quad x > L \end{cases} \quad (2.18)$$

$$h = \begin{cases} H - \frac{f^2(L-x)^2}{2g'} & , \quad x \leq L \\ H & , \quad x > L , \end{cases} \quad (2.19)$$

where, as mentioned, L is the width of the current. From (2.19) it follows that along the wall ($x = 0$),

$$h(0, y) = H - \frac{f^2 L^2}{2g'} , \quad y < 0. \quad (2.20)$$

Since the transport of the geostrophic boundary current through the zonal segment AB (**Fig. 2.4**) must be the same as the transport of the separated geostrophic current through the meridional segment BC (**Fig. 2.4**), we have

$$\frac{g'}{2f} (H^2 - h^2(0, y_s)) = \frac{g'}{2f_0} H^2 ,$$

implying that

$$h(0, y) = H \left(\frac{\beta|y|}{f_0} \right)^{1/2}, \quad y < 0. \quad (2.21)$$

Combining (2.20) and (2.21), we get an expression for the upstream boundary current width L ,

$$L = \frac{(2g'H)^{1/2}}{f} \left[1 - \left(\frac{\beta|y|}{f_0} \right)^{1/2} \right]^{1/2}.$$

Note that the upper layer thickness h in (2.21) vanishes at $y = 0$ so that the separation condition is satisfied. The actual separation latitude is a Rossby radius upstream from $y = 0$, because the geostrophic assumption is not valid in the vicinity of the separation point.

Since $|y_s| \sim O(R_{de})$, it follows that $\beta|y_s|/f_0 \sim O(\epsilon^{5/6})$, implying that to leading order,

$$L = 2^{1/2} R_d. \quad (2.22)$$

By combining (2.18), (2.19), and (2.22), we find that the momentum flux imparted on the region S by the upstream boundary current through the zonal segment AB (**Fig. 2.4**) is to leading order,

$$\int_0^L h v^2 dx = \frac{1}{15} 2^{5/2} f_0^2 H R_d^3. \quad (2.23)$$

This relationship will be employed shortly.

2.2.3.2 Zero potential vorticity eddy. The right hand side of (2.17) includes contributions from both the eddy and the separated current surrounding it. It is easy to see that the second contribution can be scaled as $O(\beta R_d R_{de} g' H^2 / f_0)$ and that its ratio to $\beta \iint_{eddy} \psi dx dy$, is of $O(\epsilon^{5/6})$. So, to find an estimate for the β term we can take $\psi = \psi_e$, where ψ_e is the zero potential eddy stream function.

For a zero-pv eddy,

$$v_\theta = -\frac{f_0 r}{2}, \quad r \leq R_1 \quad (2.24)$$

$$h_e = H_e \left(1 - \frac{r^2}{R_1^2}\right), \quad r \leq R_1, \quad (2.25)$$

where, v_θ is the orbital speed, r is the radial distance from the center of the eddy, h_e is the eddy upper layer thickness, H_e is the maximum thickness, and $R_1 = (8g'H_e)^{1/2}/f_0$. It follows from (2.25) that the eddy radius is,

$$R = \left[\frac{8g'(H_e - H_b)}{f_0^2} \right]^{1/2}, \quad (2.26)$$

where H_b is the depth on the closed stream line bounding the eddy. The corresponding stream function for the eddy is,

$$\psi_e = \frac{f_0^3}{2^6 g'} (R_1^2 - r^2)^2 + K,$$

where the constant K is found by matching the transport of the separated boundary current with the value of the stream function along the eddy boundary ($\psi_e = g'H_b^2/2f_0$ at $r = R$). This gives $K = -g'H_b^2/2f_0$ so that,

$$\psi_e = \frac{f_0^3}{2^6 g'} (R_1^2 - r^2)^2 - \frac{g'H_b^2}{2f_0}, \quad y \leq R. \quad (2.27)$$

It is worth pointing out here that it is obvious that this solution conserves the potential vorticity along the streamlines but it is less obvious that it conserves the Bernoulli function. It is easy to see, however, that the Bernoulli is also conserved because the eddy's streamlines are closed so that the Bernoulli function inside the eddy ($g'H_e$) need not be equal to that outside the eddy ($g'H$).

As a consequence of (2.15), we have $H_e \sim O(\epsilon^{-2/6}H)$, and in view of (2.26) and (2.27) it follows that to the leading order,

$$R = R_1 \text{ and } \psi_e = \frac{f_0^3}{2^6 g'} (R^2 - r^2)^2, \quad r \leq R. \quad (2.28)$$

Then, integrating (2.28) over the eddy we get,

$$\iint_{\text{eddy}} \psi_e \, dx \, dy = 2^{-6} \left(\frac{\pi}{3} \right) \frac{f_0^3}{g'^2} R^6, \quad (2.29)$$

which just like (2.23) will be shortly used to get our solution.

2.2.3.3 Radius estimate. By combining (2.17), (2.23), and (2.29), we obtain our desired nonlinear eddy scale

$$R = 2 \left(\frac{2^{5/2}}{5\pi} \right)^{1/6} \frac{R_d}{\epsilon^{1/6}}. \quad (2.30)$$

Relation (2.30) is an analytical estimate for the eddy radius based on our momentum balance approach. It relates the eddy size to the known physical parameters upstream. It is opportune to point out that (2.30) is a lower bound estimate for the eddy radius, because the zero pv eddy is highly nonlinear and, as a consequence, it is the steepest anticyclonic eddy possible.

2.3 Numerical Simulations

In order to test our analytical result and further investigate the role of β in the eddy formation, numerical simulations are performed and the results are quantitatively analyzed. In these simulations we compare the evolution of the system on both f-plane and β -plane (for the same set of physical parameters).

2.3.1 Numerical Model Description

We use a reduced gravity version of the isopycnic model developed by Bleck and Boudra (1981,1986) and later improved by Bleck and Smith (1990). This model is suitable for our study since it allows isopycnic outcropping by using the “Flux-Corrected Transport” algorithm (Boris and Book 1973; Zalesak 1979) in the continuity equation.

The equations of motion are the two momentum equations,

$$\begin{aligned}\frac{\partial u}{\partial t} + u\frac{\partial u}{\partial x} + v\frac{\partial u}{\partial y} - (f_0 + \beta y)v &= -g'\frac{\partial h}{\partial x} + \frac{\nu}{h}\nabla \cdot (h\nabla u) \\ \frac{\partial v}{\partial t} + u\frac{\partial v}{\partial x} + v\frac{\partial v}{\partial y} + (f_0 + \beta y)u &= -g'\frac{\partial h}{\partial y} + \frac{\nu}{h}\nabla \cdot (h\nabla v),\end{aligned}$$

and the continuity equation

$$\frac{\partial h}{\partial t} + \frac{\partial(hu)}{\partial x} + \frac{\partial(hv)}{\partial y} = 0,$$

where ν is the friction coefficient.

The model uses the Arakawa (1966) C-grid where the u -velocity points are shifted one-half grid step to the left from h points, the v -velocity points are shifted one-half grid step down from the h points, and vorticity points are shifted one-half grid step down from the u -velocity points. The integration domain is rectangle with a closed western and northern boundaries, open eastern boundary, and imposed inflow on the southern boundary. The Orlanski (1976) second-order radiation boundary condition was implemented on the open boundary .

Three extensive experiments were performed and the respective parameters are listed in Table 2.1. Additional experiments are not necessary for two reasons. First, the parameter controlling the experiment is the undisturbed upper layer thickness H as it sets up both the the boundary current transport ($g'H/2f_0$) and the Rossby radius of deformation R_d . So, all boundary current parameters are determined by

H , and consequently, after nondimensionalizing the equations of motion of any two runs would differ only by the nondimensional β ($\beta R_d/f_0$) and the nondimensional coefficient of friction ($\nu/f_0 R_d^2$). As long as the western boundary current is inertial the parameter $\beta R_d/f_0$ is the only one that is controlling the experiment. In midlatitude the parameter $\beta R_d/f_0$ does not have a significant variation so three experiments are sufficient. Second, for each of the three experiments that are conducted, we let the model run for 10,000 days, giving a massive data set.

The parameters adopted for the main experiment E1 are indicated in Table 2.1. The baroclinic Rossby radius of deformation is 25 km and the transport of the boundary current is about 7.7 Sv ($1 \text{ Sv} = 10^6 \text{ m}^3 \text{ s}^{-1}$). Due to computer time limitation we take a time step of 720 seconds and a grid size of 15 km, so that we are barely resolving the Rossby radius. Since the eddy is greater than the Rossby radius this is not an issue. It would, of course, been better to use a higher resolution but, as we shall see, the results are so robust that this apparent weakness is not significant. We adopt the free slip boundary condition and a relatively large horizontal friction ($\nu = 1500 \text{ m}^2 \text{ s}^{-1}$) in order to smooth out transient features. The initial condition for the β -plane experiments is the day 200 fields of an f -plane run with a zonal wall dividing the domain (the f -plane experiment will be discussed later). On the southern edge we use the same parameters as above and on the northern edge the upper layer thickness is zero. We then take the wall out and, at the same time turn beta on. We then let the system evolve for 10,000 days.

For economical reasons the parameters used in the numerical experiment E1 are not identical to those of the JES, where the EKWC has transport of merely 1.5 Sv (which would imply an undisturbed upper layer thickness $H = 133 \text{ m}$). For the real JES the Rossby radius of deformation would be smaller and we would have to decrease the integration time step, making our runs more time consuming. This is not an issue even though our β effect is stronger than that in the JES, because it merely makes our runs spin up faster.

Table 2.1. List of experiments

Experiment	Parameters	Resolution, Time Step	Basin size
E1	$f_0 = 0.8573 \times 10^{-4} \text{ s}^{-1}$, $\beta = 1.849 \times 10^{-11} \text{ m}^{-1} \text{ s}^{-1}$, $g' = 0.014 \text{ m}^2 \text{ s}^{-1}$, $H = 300 \text{ m}$, $\nu = 1500 \text{ m}^2 \text{ s}^{-1}$	15 km, 12 min	1500 km \times 3000 km
E2	$f_0 = 0.8573 \times 10^{-4} \text{ s}^{-1}$, $\beta = 1.849 \times 10^{-11} \text{ m}^{-1} \text{ s}^{-1}$, $g' = 0.014 \text{ m}^2 \text{ s}^{-1}$, $H = 300 \text{ m}$, $\nu = 500 \text{ m}^2 \text{ s}^{-1}$	15 km 12 min	1500 km \times 3000 km
E3	$f_0 = 0.8573 \times 10^{-4} \text{ s}^{-1}$, $\beta = 0$, $g' = 0.014 \text{ m}^2 \text{ s}^{-1}$, $H = 300 \text{ m}$, $\nu = 500 \text{ m}^2 \text{ s}^{-1}$	15 km, 12 min	1500 km \times 3000 km

2.3.2 General Results

Fig. 2.5 and **Fig. 2.6b,d** show the contour plots of the nondimensional upper layer thickness for the f-plane run (experiment E3 in Table 2.1) at days 100, 500, 1000, and 3000. The most important aspect is that there is no eddy. Even though there is an area of increased upper layer thickness and transport due to accumulation of fluid displaced from the western boundary, the resulting circulation is much weaker than that of the β -plane run (**Fig. 2.6a,c**). It can be seen that the entire system moves

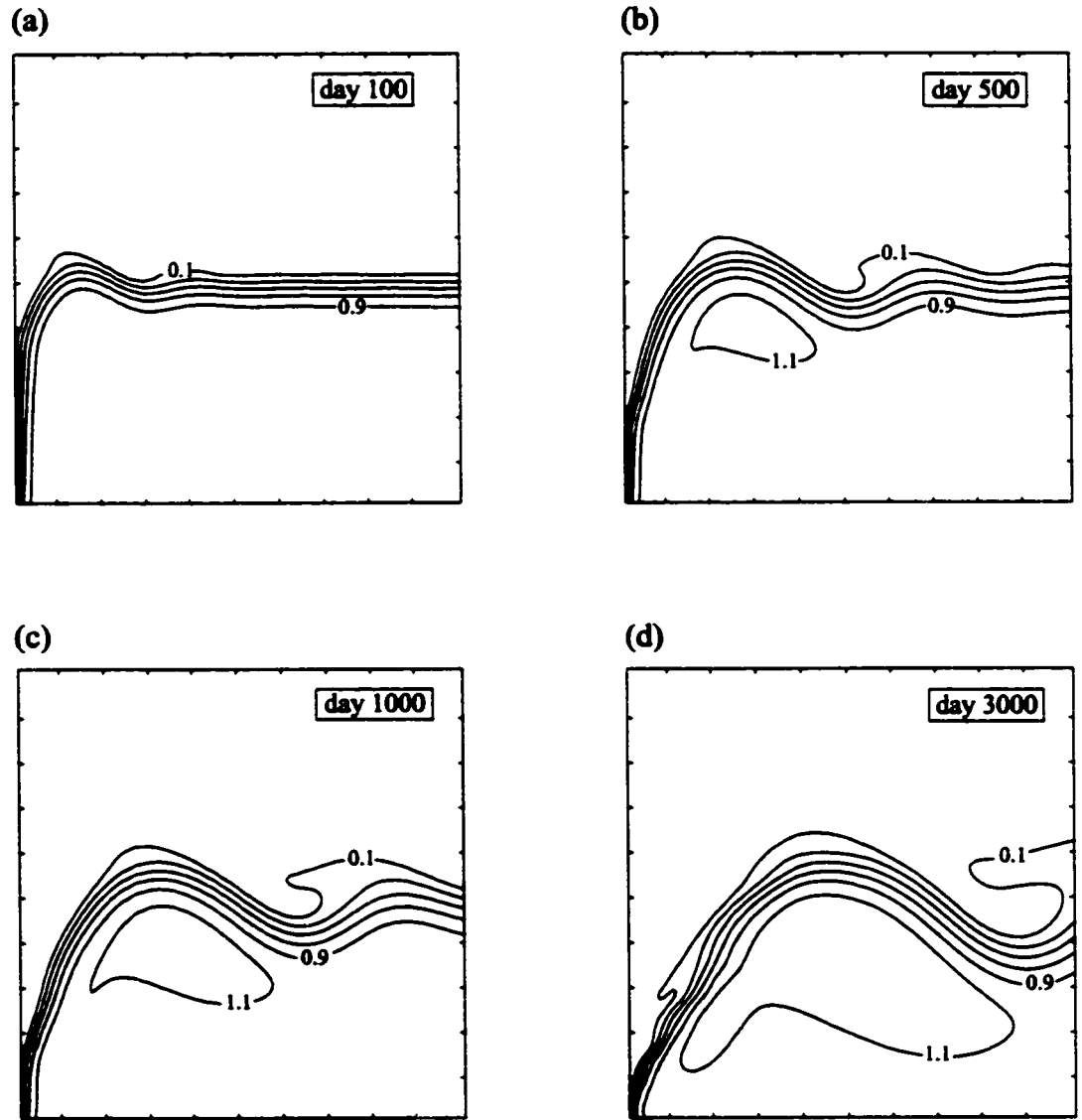
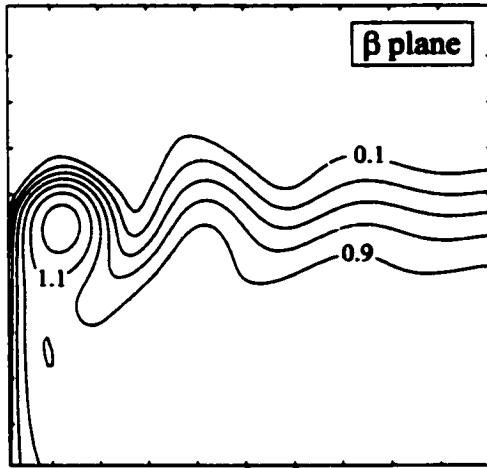
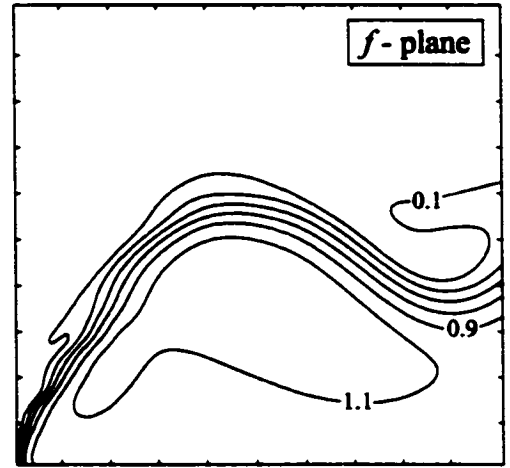


Figure 2.5. Contour maps of the upper layer thickness nondimensionalized by $H = 300$ m for the f -plane run (experiment E3 in Table 2.1) at days: (a) 100; (b) 500; (c) 1000; (d) 3000. The contour spacing is 0.2. The axes marks are 10 grid points (150 km) apart.

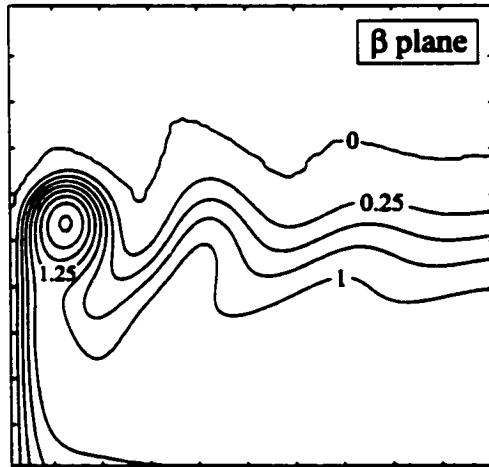
(a) Nondimensional upper layer depth



(b) Nondimensional upper layer depth



(c) Nondimensional streamfunction



(d) Nondimensional streamfunction

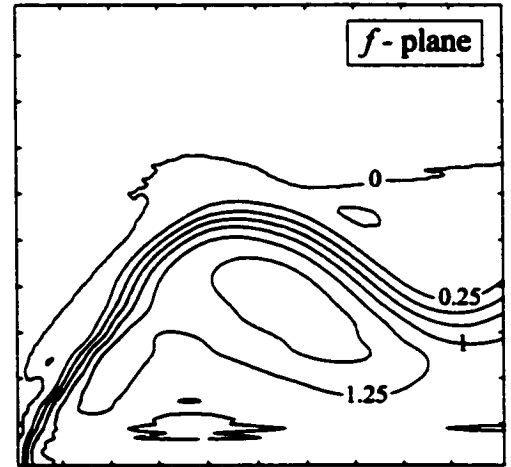


Figure 2.6. Snapshots at day 3000: (a) Contour map of the nondimensional upper layer thickness (h/H) for the β -plane run (experiment E1 in Table 2.1). Contour spacing of 0.2; (b) Same as in (a) for the f -plane run (experiment E3 in Table 2.1); (c) Contour map of the nondimensional stream function [$\psi/(g'H/2f_0)$] for the β -plane run (experiment E1 in Table 2.1). Contour spacing of 0.25; (d) Same as in (c) for the f -plane run (experiment E3 in Table 2.1). The axes marks are 10 grid points (150 km) apart.

offshore and, consequently, it cannot reach a steady state. In order to highlight the offshore movement of the system we plot in **Fig. 2.7**, the 0.3 contour for each of the

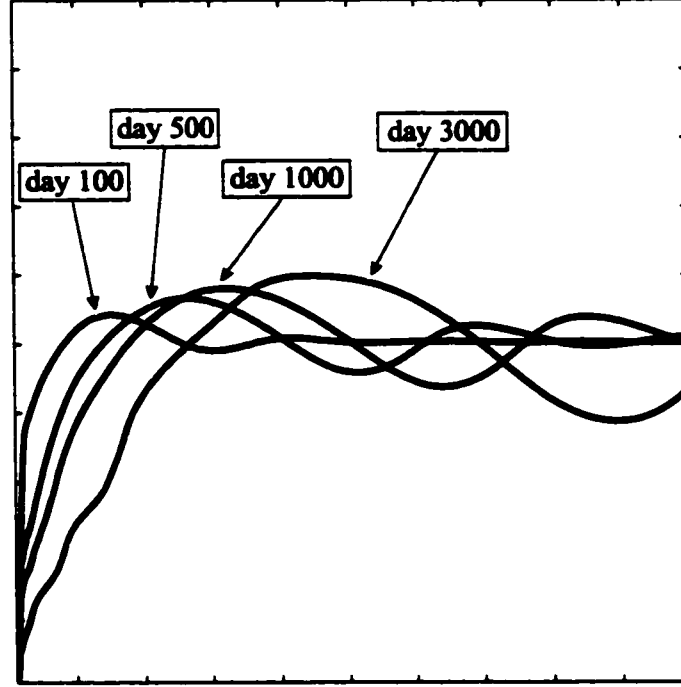


Figure 2.7. Superposition of the 0.3 contours for the f-plane run (experiment E3 in Table 2.1) at day 100, 500, 1000, and 3000, showing the offshore movement of the system.

days depicted in **Fig. 2.5**. In analogy with the ballooning outflow situation studied by Nof and Pichevin (2001), the eastward movement of the separated boundary current produces a Coriolis force directed to the south. This force balances the northward momentum flux of the separated boundary current.

In **Fig. 2.6**, we plot side by side snapshots of the nondimensional upper layer thickness and nondimensional streamfunction at day 3000 for the β -plane experiment E1 and f-plane experiment E3 (Table 2.1). This day is chosen as a representative of the entire experiment E1 because it reflects a steady solution. We see that the intrusion eddy is a very prominent feature on the β -plane plots [**Fig. 2.6a,d**] with

maximum nondimensional upper layer thickness greater than 1.3 and maximum nondimensional transport of 2. It is important to note that the boundary current is inertial (i.e., nonlinear) as its width is $O(R_d) = 25$ km, much smaller than the frictional boundary layer width $O[(\nu/\beta)^{1/3}] = 200$ km. Here, the friction used is high enough to avoid the transient features but not so large to change the dynamics of the boundary current. The downstream zonal flow is broad compared with the upstream boundary current due to friction diffusivity. To go further with the comparison of the numerical results to our analytical relations, let's rewrite (2.8), using (2.9) evaluated at $x = 0$ and assuming that $\psi = 0$ on the wall. Then

$$\underbrace{\int_0^L h v^2 dx}_{\text{WBC momentum flux}} + \underbrace{\frac{g'}{2} h^2(0, y_s) L_2}_{\text{pressure}} - \underbrace{\beta \iint_S \psi dx dy}_{\beta\text{-force}} = 0, \quad (2.31)$$

where L is the boundary current width and L_2 is the length of the segment AB (see **Fig. 2.4**). In this form (2.31) represents a balance between three forces. The first is the northward force associated with the momentum flux of the alongshore current. The second is a northward pressure force due to the difference in thickness on the wall between points A and D (**Fig. 2.4**). The third term is a southward β -force resulting from the fact that a particle circulating anticyclonically within the eddy senses a larger Coriolis force on the northern than it senses on the southern side of the path.

Fig. 2.8 displays each term of (2.31). It is evident that the intrusion eddy exists in order to balance the northward momentum flux of the western boundary current because, according to (2.17) and the scale analysis, the eddy is the major contributor for the net β term [combination of the second and third terms in (2.31)].

As stated before, the frictional coefficient used acts merely to smooth out transient features and does not play an important role in the integrated momentum balance. To verify that this is indeed the case, we performed experiment E2 (Table 2.1) with

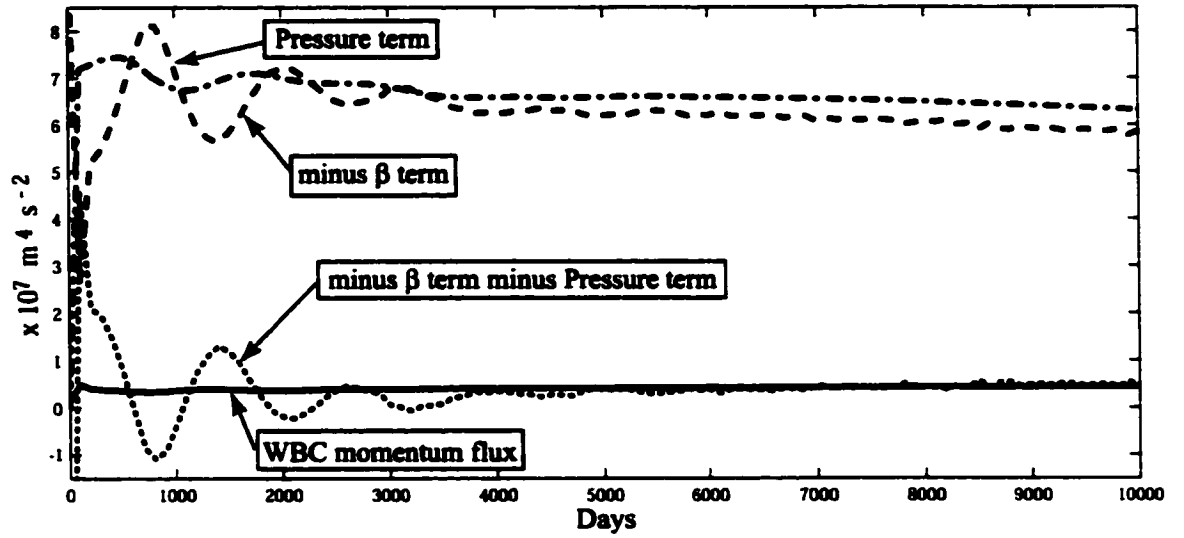


Figure 2.8. Estimate of the terms in the equation (2.31) from the experiment E1 (Table 2.1).

lower friction and we got essentially the same results as in E1. The only difference between the two is that here the separated current showed meanders that eventually closed upon themselves pinching off eddies that died off (or were reattached to the main flow after some time).

In Fig. 2.9 we show the analytical estimate of the eddy radius from (2.30) against the numerical estimate [taking the 1.3 closed (nondimensional) streamline as the eddy boundary (Fig. 2.6c)]. As expected, the radius based on the zero potential vorticity assumption is a lower bound for the actual eddy radius because the zero pv eddy is the steepest possible eddy (Nof 1981; Killworth 1983). Nevertheless, the agreement is pretty good, as we get $4.2 R_d$ for the analytical estimate and about $5 R_d$ (after day 1000) for the numerical estimate.

2.4 The Linear Dynamics

We shall now show that for a small Rossby number flow (i.e., a linear geostrophic flow) there is no eddy associated with the current separation from the coast. In

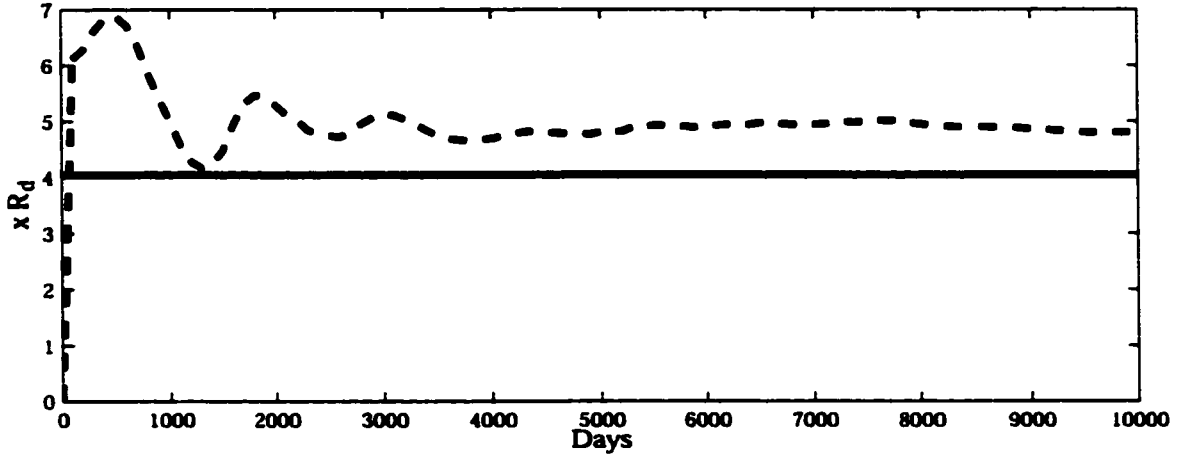


Figure 2.9. Estimates of the eddy radius. Solid line: Analytical [from equation (2.30)]. Dashed line: Numerical (taking the value of 1.3 for the nondimensional streamline as the eddy boundary). Both plots are scaled by the Rossby radius.

the linear limit, the boundary current width is large (due to the frictional nature of the boundary layer) compared with the Rossby radius so that the current is slower and the associated momentum flux is negligible. As we will see, in this situation the frictional dissipation balances the β term in the boundary layer and no eddy is necessary.

Consider the familiar, steady linear reduced-gravity (depth integrated) equations of motion for the upper layer

$$-f v h = -\frac{g'}{2} \frac{\partial(h^2)}{\partial x} + \frac{\tau^x}{\rho} \quad (2.32)$$

$$f u h = -\frac{g'}{2} \frac{\partial(h^2)}{\partial y} - \kappa v h \quad (2.33)$$

$$\frac{\partial(uh)}{\partial x} + \frac{\partial(vh)}{\partial y} = 0, \quad (2.34)$$

where κ is the interfacial friction coefficient and the rest of the notation was previously defined. In the inviscid interior, Sverdrup dynamics dominates the field. Within the western boundary current interfacial friction dissipates the energy input of the wind over the entire basin.

2.4.1 Momentum Balance in the Whole Domain

Integrating the y -momentum equation (2.33) over the integration area S (containing the western boundary current) bounded by $ABCD$ (Fig. 2.10), and assuming

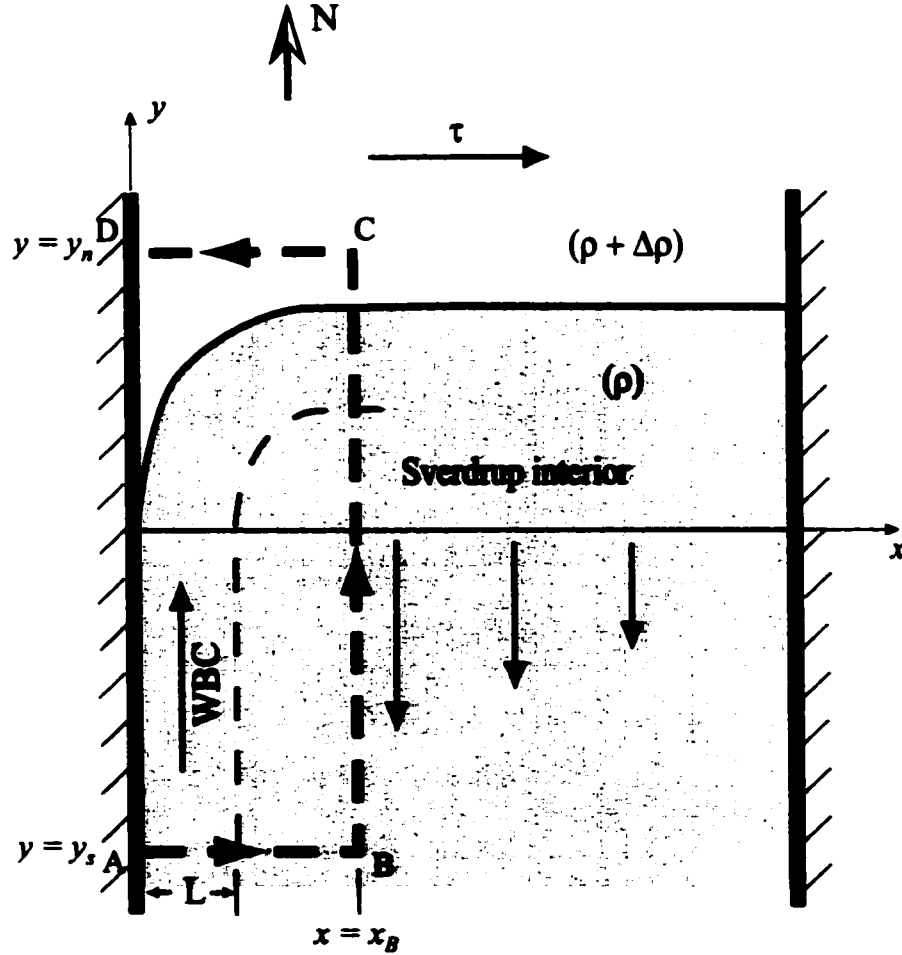


Figure 2.10. Schematic representation of the linear limit, i.e., here we take the boundary current to be a linear frictional current rather than inertial. The shaded area represents the region where the lighter layer is present. The circulation is established by the wind stress τ ; in the basin interior the slow southward Sverdrup flow takes place, while in the narrower western boundary layer (of width L) a stronger northward western boundary current (WBC) closes the anticyclonic gyre. In this linear limit the boundary current leaves the coast by vanishing the upper layer thickness (à la Parsons 1969).

that $\psi = 0$ on the bounds of the region containing the upper layer, we find,

$$\int_0^{x_B} \left[\frac{g'}{2} h^2 - (f_0 + \beta y) \psi \right] dx - \beta \iint_S \psi dx dy - \kappa \int_{y_s}^{y_n} \psi|_{x=L} dy = 0, \quad (2.35)$$

where L is the boundary current width, $\psi|_{x=L}$ is the stream function at $x = L$, x_B is the x -component of B and y_s and y_n are the y -components of A and D respectively (Fig. 2.10). We shall now leave (2.35) aside for a moment and discuss the interior.

2.4.2 The Interior Balance

We note from (2.33) that in the inviscid ocean interior (where friction is unimportant),

$$\frac{\partial}{\partial y} \left[\frac{g'}{2} h^2 - (f_0 + \beta y) \psi \right] = -\beta \psi, \quad (2.36)$$

which can be integrated from y_s to y_n to give,

$$\left[\frac{g'}{2} h^2 - (f_0 + \beta y) \psi \right]_{y=y_s}^{y=y_n} = \beta \int_{y_s}^{y_n} \psi dy \quad (2.37)$$

for any $x > L$. Integrating (2.37) from $x = L$ to $x = x_B$, we get

$$\int_L^{x_B} \left[\frac{g'}{2} h^2 - (f_0 + \beta y) \psi \right] dx - \beta \int_L^{x_B} \int_{y_s}^{y_n} \psi dy dx = 0. \quad (2.38)$$

This balance is valid in the integration domain (S) within the ocean interior.

2.4.3 The Western Boundary Layer Balance

Subtracting (2.38) from (2.35) we obtain,

$$\int_0^L \left[\frac{g'}{2} h^2 - (f_0 + \beta y) \psi \right] dx - \beta \int_{y_s}^{y_n} \int_0^L \psi dx dy - \kappa \int_{y_s}^{y_n} \psi|_{x=L} dy = 0. \quad (2.39)$$

Neglecting the wind stress term (since its role is minor in the boundary current), it follows from (2.32) that

$$\frac{g'}{2} h^2 - (f_0 + \beta y) \psi = C \quad , \quad x \leq L, \quad (2.40)$$

where C is a constant to be determined by matching (2.40) and (2.37) at $x = L$, obtaining $C = \int_{y_*}^{y_n} \psi|_{x=L} dy$. Substituting (2.40) into (2.39), we obtain

$$\beta \int_{y_*}^{y_n} \int_0^L (\psi - \psi|_{x=L}) dx dy + \kappa \int_{y_*}^{y_n} \psi|_{x=L} dy = 0. \quad (2.41)$$

The integrand of the second term of (2.41) is positive, implying that the first term should be negative. Note that an anticyclonic eddy would make a negative contribution to the β term. By scaling (2.41), it follows that the boundary current by itself produces a β -force that is able to balance the friction dissipation [second term in (2.41)] as long as $L \sim O(\kappa/\beta)$ (which is the well known Stommel boundary layer scale).

We see that (2.41) represents a balance between the β -force in the western boundary current and the frictional dissipation of the integrated wind stress curl over the entire basin. Under these conditions, no eddy is necessary for the required momentum balance showing that the establishment of the intrusion eddy is due to inertia (nonlinearities) and β .

2.5 Conclusions

Taking into account that the western boundary current in the JES is forced to separate from the coast by an outflow to the east, we derived a theory for the existence of the “intrusion eddy”. Our analytical relations and numerical simulations show that, without the generation of the eddy, the nonlinear momentum flux of the northward flowing boundary current on a β -plane could not have been balanced [on

an f-plane the situation is quite different. To balance the northward momentum force imparted by the boundary the system simply moves offshore (Fig. 2.7) producing a southward Coriolis force]. On this basis, we argue that the existence of the UWE is not related to instabilities but rather is due to β and nonlinearities (Fig. 2.6 and Fig. 2.8). Furthermore, we argue that the UWE semi-permanent characteristic is not due to topographic arrest but rather a part of the dynamics which includes the generation of a permanent eddy (Fig. 2.6a,c). For a mean transport of ~ 1.5 Sv for the EKWC, we find a Rossby radius of 16.3 km, and an $\epsilon^{1/6}$ of 0.39. Our predicted value for the UWE diameter from (2.30) is then 141 km, which agrees fairly well with the observed 150 km radius (Fig. 2.2) suggesting that its generation is related with the mechanism proposed here.

The present theory cannot be applied to the Gulf stream and Brazil-Malvinas confluence for three reasons. First, in both cases there are strong opposing (cold) currents (Labrador current in the first case and the Malvinas current in the second) whose momentum fluxes cannot be neglected. Second, there is a marked difference in density between the two colliding currents so that the denser (colder) current would slide under the less dense current and even separate from the coast in a different latitude. Third, there is a coastline tilt in both cases that could cause significant change in the momentum balance.

CHAPTER 3

THE MINDANAO AND HALMAHERA EDDIES ARE DUE TO THE BENDING OF THEIR PARENT CURRENTS, NONLINEARITIES AND β

3.1 Introduction

The western equatorial Pacific has been the subject of increasing attention in the last few decades. It plays a key role in the establishment of El Niño and Southern Oscillation (e.g., Webster and Lukas 1992) and, it may also be an important part of the so-called “great conveyor belt” (e.g. Gordon 1986) because of the Pacific-to-Indian throughflow (ITF). The eddies and the low-latitude western boundary currents addressed here (**Fig. 3.1**) are important aspects of these processes.

The equatorward flowing western boundary currents (WBC) provide the closure to two Sverdrup asymmetrical gyres relative to the equator (Kessler and Taft 1987). One gyre is entirely in the Northern Hemisphere whereas the other (which is mostly in the Southern Hemisphere) crosses the equator. The North Equatorial Countercurrent (NECC) forms the boundary between these two gyres at about 5°N. North of the NECC the westward flowing North Equatorial Current (NEC) bifurcates as it encounters the Philippines (Toole et al. 1990) into the northward flowing Kuroshio and the southward flowing Mindanao Current (MC). A similar situation takes place in the Southern Hemisphere where the westward flowing South Equatorial Current (SEC) bifurcates around 15°S into a branch flowing northwestward and a branch

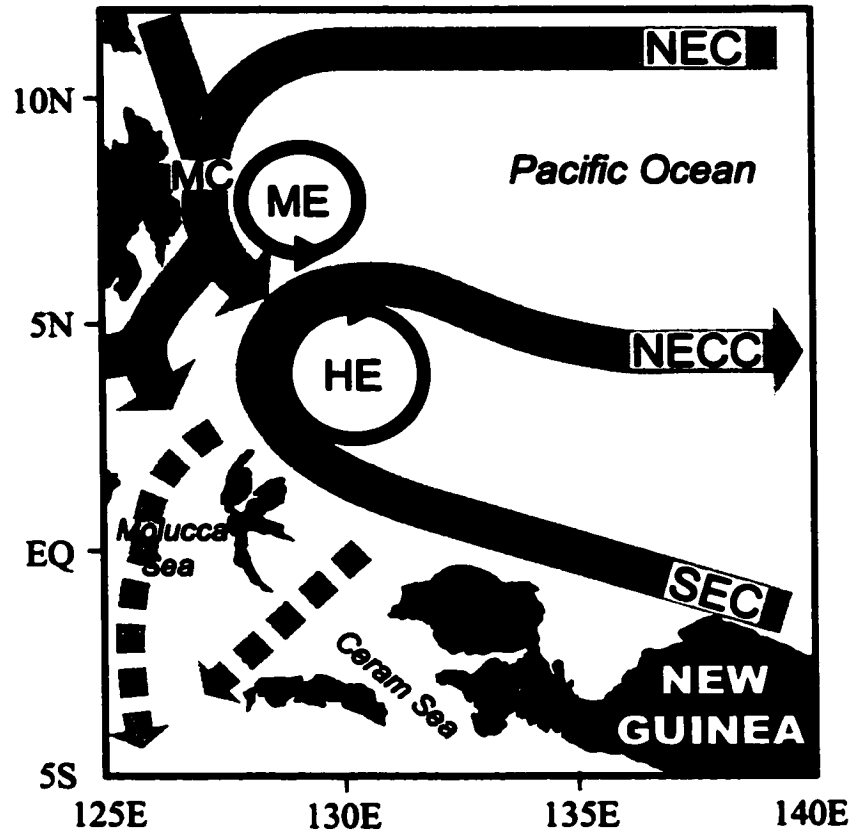


Figure 3.1. The flow pattern in the western equatorial Pacific (adapted from Field and Gordon 1992). The Mindanao eddy (ME) and the Halmahera eddy (HE) are semi-permanent and do not usually drift away from their generation area. Dashed arrows denote the southern part of the Indonesian throughflow (ITF).

flowing southward. Along the New Guinea coast the northwestward flowing branch of the SEC is usually recognized as a subsurface current, the New Guinea Coastal Under-Current (NGCUC), and a surface current, the New Guinea Coastal Current (NGCC). The SEC which retroflects to the east of the Halmahera Island joins the retroflected flow of the MC and flows eastward as the NECC.

There are two semi-permanent eddies in the retroflection area of the MC and SEC (Fig. 3.1). The first, the Mindanao eddy (ME), is situated north of the NECC (near 7°N, 128°E) and has cyclonic circulation, whereas the second, the Halmahera eddy (HE), which is situated south of the NECC (near 4°N, 130°E) has anticyclonic

circulation (Wyrтки 1961). We shall now briefly describe the two colliding boundary currents (MC and SEC), the Mindanao and Halmahera eddies, and the Indonesian throughflow (ITF) which plays a secondary (but still important) role in the dynamics of the eddies.

3.1.1 The Mindanao Current

The Mindanao Current extends to a depth of 600 m and a distance 100 km offshore (Wyrтки 1961, Masuzawa 1968). Wyrтки (1956, 1961) estimated a baroclinic transport ranging from 8 to 12 Sv ($1 \text{ Sv} = 10^6 \text{ m}^2 \text{ s}^{-1}$) in the upper 200 m and 25 Sv in the upper 1000 m. Masuzawa (1969) estimated a transport from 13 to 29 Sv relative to 600 dbar. Kendall (1969) used historical hydrographic data to argue that the MC carries 14 Sv which is half of the NECC estimated transport (43 Sv). From two synoptic sections separated by 180 km, Cannon (1970) estimated a geostrophic transport of 18 to 31 Sv relative to 1000 dbar and a surface current speed of $1.0\text{--}1.2 \text{ m s}^{-1}$. Toole et al. (1988) estimated a transport of 17-18 Sv for waters warmer than 12°C relative to 1000 dbar. Using direct current measurements, Lukas et al. (1991) calculated a transport in the upper 300 m increasing from 13 Sv to 33 Sv between 10°N and 5.5°N . Acoustic Doppler Current Profiler (ADCP) measurements along 8°N analyzed by Wijffels et al. (1995) show the Mindanao Current as an intense 200 km wide coastally trapped jet with typical inshore velocity maximum of 1 m s^{-1} .

3.1.2 Mindanao Eddy

Takahashi (1959) noted the existence of “a cold region of distorted elliptic form” east of Mindanao in observations made in the early 1950s, and related this feature to the cyclonic circulation inferred from dynamic topography. This closed circulation is named “Mindanao eddy” after Wyrтки (1961). Wyrтки noted that the ME is a quasi-permanent eddy associated with the turning of the NEC waters at the coast

of the Philippines and their subsequent flow to the east in the NECC. Lukas et al. (1991) reported that drifters launched in the ME described closed loops with a diameter of about 250 km. Using a climatology of the circulation near the Philippine Coast (derived from historical hydrographic data combined with recent cruises), Qu et al. (1999) identified the ME as a depression (of less than 130 m) in the $24.5 \sigma_\theta$ isopycnal surface centered at 7°N , 129°E .

3.1.3 The South Equatorial Current

As mentioned, the westward flowing SEC bifurcates near 15°S . The equatorward branch is the Great Barrier Reef Undercurrent (Church and Boland 1983), which flows into the NGCUC (Tsuchiya et al. 1989). Using a vertical section along 133.5°E and 137°E during January-February, Masuzawa (1968) observed the existence of a shallow eastward and northwestward monsoonal current (the NGCC) overlying the strong northwestward flow of the NGCUC. Cantos-Figuerola and Taft (1983) found a transport of 11 Sv in the SEC over 2°S to 2°N during the Hawaii-Tahiti Shuttle Experiment. The mean SEC transport poleward of 2°S is 35.1 Sv with a standard deviation of 5.1 Sv. Using profiling current meter data between 2°S and the equator, Wyrтки and Kilonsky (1984) estimated a SEC transport of about 40 Sv. Using data collected between January 1994 and July 1991, Gouriou and Toole (1993) found, a SEC transport (at 165°E) of 24.8 Sv from direct measurements, 37.7 Sv from geostrophy relative to 600 dbar, and 41.7 Sv from geostrophy relative to 1000 dbar. At 142°E they found 23.8 Sv from direct measurements and 31 Sv from geostrophy relative to 600 dbar.

3.1.4 The Halmahera Eddy

As the Mindanao eddy, the Halmahera eddy appears in the dynamic topography maps of Takahashi (1959) and was named by Wyrтки (1961). It is well developed only

during the summer monsoon, when the South Pacific water from the SEC recurves into the NECC. Lukas et al. (1991) released drifters (between June and July 1998) into the HE. They executed closed loops of about 300 km diameter (with overall size appearing to be about 470 km) and velocity about 50 cm s^{-1} . Using current measured by shipboard ADCP during June 1995 and July 1996, Kashino et al. (1999) located the center of the Halmahera eddy to be east of 130°E and the horizontal scale of about 500 km (at 50 m). Using data from drifters released in the HE during summer and fall of four different years, Waworuntu (1999) showed that the HE has large relative vorticity suggesting that its core contains mainly south Pacific water.

3.1.5 The Indonesian Throughflow

The convergence of the strong equatorward flows in the western equatorial Pacific is compensated by strong eastward flows which are part of the equatorial Pacific circulation (e.g., the NECC) and also by the loss of some water to the Indian Ocean via the ITF. Observational estimates of the throughflow range from 2 to 20 Sv but the most up-to-date estimate is of 6-12 Sv (Wyrtki 1961; Piola and Gordon 1984; Fine 1985; Fu 1986; Toole et al. 1988; Murray and Arief 1988; Murray et al. 1990; Meyers et al. 1996; Fieaux et al. 1994; Cresswell et al. 1993; Wijffels 1993; Aung 1998; Gordon et al. 1999; Molcard et al. 2000; Sprintall et al. 2002; Wijffels et al. 2002). Computational estimates based on numerical modeling are in the same range (Cox 1975; Godfrey 1989; Godfrey and Golding 1981; Godfrey et al. 1993; Semter and Chevin 1988, 1992; Kindle et al. 1987, 1989; Inoue and Welsh 1993; Hist and Godfrey 1993). For observational and theoretical studies about the ITF composition (i.e., the question of whether the ITF carries south or north Pacific water) the reader is referred to Fine (1985), Godfrey (1989), Field and Gordon (1992), Godfrey et al. (1993), Wajsowicz (1993a,b), Fine et al. (1994), Gordon (1995), Nof (1995a,b), Wajsowicz (1998), Waworuntu (1999), and Waworuntu et al. (2000,2001) among others.

It is straightforward to show that the ITF is very important for the existence of the cross equatorial flow of the SEC, for its retroflection, and for the eddies under discussion. Without the ITF there would not be any collision of boundary currents in the western Pacific and, consequently, there would not be any eddies. To see this we note that, in a reduced gravity scenario the thickness at the offshore edge of the western boundary currents (H) can be computed from the familiar vertically integrated x -momentum equation,

$$-fV = -\frac{g'}{2} \frac{\partial(h^2)}{\partial x} + \frac{\tau^x}{\rho}, \quad (3.1)$$

where V is the meridional transport and τ^x is the x -component of the wind stress. (For convenience variables are defined both in the text and in the Appendix.) Eq. (3.1) holds in the sluggish ocean interior away from the boundaries, as well as in the intense western boundary currents where the flow is geostrophic in the cross-stream direction. To obtain the desired thickness H , the Sverdrup relation [$\beta V = -(1/\rho) \partial \tau^x / \partial y$] which holds only in the interior, is substituted into (3.1) and the resulting equation is integrated from the eastern edge of the boundary current to the eastern boundary of the Pacific Ocean. Following the observations of Collin et al. (1971), it is further assumed that the upper layer thickness along the eastern boundary vanishes. One then finds

$$H = \left(\frac{2}{g'} \right)^{1/2} \left[\frac{f}{\beta \rho} \int_0^{L_P} \frac{\partial \tau^x}{\partial y} dx - \int_0^{L_P} \frac{\tau^x}{\rho} dx \right]^{1/2}, \quad (3.2)$$

where L_P is the width of the basin (much greater than R_d).

Using the Hellerman and Rosenstein (1983) mean wind stress and $g' = 0.02 \text{ ms}^{-2}$, the calculated value [from (3.2)] for the offshore depth is 235.32 m at 1°N and 97.83 m at 9°N . Taking f_0 at 5°N , the associated NECC geostrophic transport [$g'(H_s^2 - H_n^2)/2f_0$] is about 36 Sv which is in good agreement with observations

(Kessler and Taft 1987). Note that what we have done so far is independent of the WBC structure which we will now tend to.

Integrating (3.1) from the western to the eastern boundary and temporarily assuming no net meridional transport, i.e, a WBC with a transport equal and opposite to the interior Sverdrup transport which is equivalent to saying that there is no ITF, we find,

$$h_{wb} = \left(\frac{2}{g'} \right)^{1/2} \left[- \int_0^{L_P} \frac{\tau^x}{\rho} dx \right]^{1/2}, \quad (3.3)$$

where h_{wb} is the upper layer thickness on the western boundary. Using the Hellerman and Rosenstein (1983) mean wind stress the calculated values of h_{wb} from (3.3) are 235.24 m at 1°N and 301.57 m at 5°N. In view of the earlier calculated offshore values (235.32 m at 1°N and 97.83 m at 9°N), this means that, in the above conditions of no ITF, there is essentially no SEC at 1°N and the southward MC transport at 5°N is 35.7 Sv. This leads to the important conclusion that, in the absence of the ITF, there would be no collision and no eddies. It also shows the importance of the ITF in establishing the cross equatorial flow of the SEC. This completes the demonstration that the ITF is critical to our problem and we shall now return to our general introduction.

As mentioned our goal is to examine the nonlinear collision of opposing western boundary currents on a β -plane. We shall see that it is the curving of the retroflecting currents and β which are responsible for the generation of the eddies. The presentation is organized as follows: In Section 2 we formulate the problem of a western boundary current in a concave solid corner. In Section 3 we analyze numerical model simulations for the above the problem of a western boundary in a concave solid corner. In Section 4 we present analytical eddy radius estimates for the problem of a western boundary current in a concave solid corner on a β -plane. In Section 5 we focuses on the collision problem. In Section 6 we apply the results

of the previous sections to the equatorial western Pacific and suggests the physical mechanism responsible for the existence of the Mindanao and Halmahera eddies. In section 7 we present our conclusions.

3.2 Flow in a Concave Solid Corner

Before attacking the full collision problem it is useful to first examine the behavior of currents in a concave solid corner formed by a solid boundary. We shall do so by using the momentum flux approach introduced in Chapter 1.

3.2.1 Formulation

As the WBC (Fig. 3.2) flows northward it encounters a zonal wall that forces it to turn the corner and flows eastward. We place the origin of our coordinate system at the corner and assume that, far away from the western boundary and a few Rossby radii south of the zonal wall, the upper layer thickness is H . We shall later expand the boundary current dependent variables around an f-plane solution with potential vorticity depth H .

Assuming a steady state and integrating (after multiplying by h) the steady and inviscid nonlinear y -momentum equation,

$$u \frac{\partial v}{\partial x} + v \frac{\partial v}{\partial y} + fu + g' \frac{\partial h}{\partial y} = 0,$$

over the fixed region S bounded by the dashed line $ABCD$ shown in the upper left panel in Fig. 3.2, we get

$$\iint_S (hu \frac{\partial v}{\partial x} + hv \frac{\partial v}{\partial y}) dx dy + \iint_S (f_0 + \beta y) uh dx dy + \frac{g'}{2} \iint_S \frac{\partial(h^2)}{\partial y} dx dy = 0, \quad (3.4)$$

which, by using the continuity equation and stream function ψ , can be reduced to

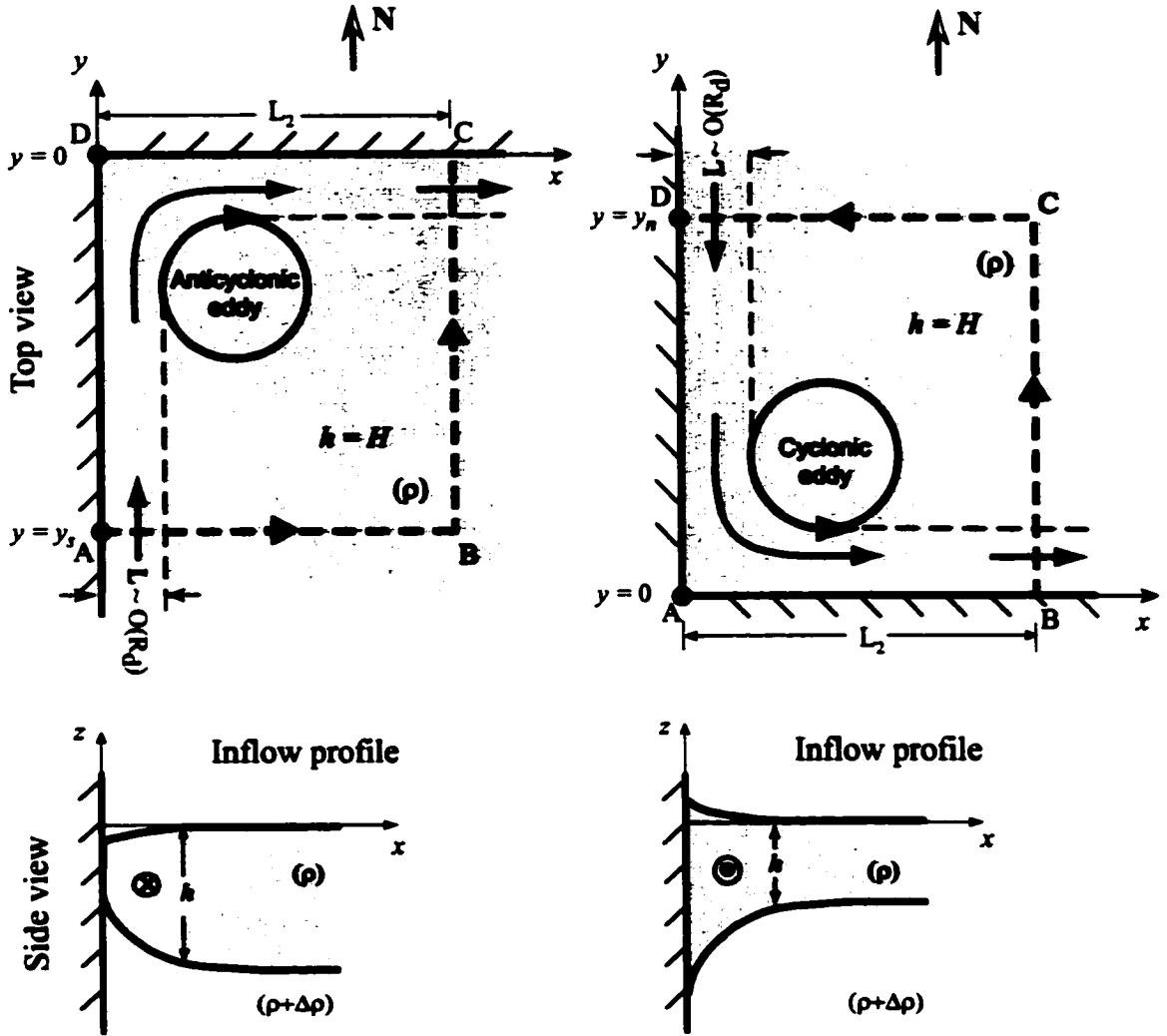


Figure 3.2. Schematic diagram of the model. Upper panels: A northward (southward) flowing western boundary current (WBC) encountering a zonal wall. H is the upper layer far east from the western boundary on a latitude a few Rossby radius away from the zonal wall; Lower panels: Vertical cross-section of the approaching northward (southward) flowing WBC.

$$\iint_S \left[\frac{\partial(huv)}{\partial x} + \frac{\partial(hv^2)}{\partial y} \right] dx dy - \iint_S (f_0 + \beta y) \frac{\partial \psi}{\partial y} dx dy + \frac{g'}{2} \iint_S \frac{\partial(h^2)}{\partial y} dx dy = 0, \quad (3.5)$$

where g' is the reduced gravity, $g\Delta\rho/\rho$.

Eq. (3.5) can be rewritten as,

$$\begin{aligned} & \iint_S \left[\frac{\partial(huv)}{\partial x} + \frac{\partial(hv^2)}{\partial y} \right] dx dy - \iint_S f_0 \frac{\partial \psi}{\partial y} dx dy \\ & - \iint_S \left[\frac{\partial(\beta y \psi)}{\partial y} - \beta \psi \right] dx dy + \frac{g'}{2} \iint_S \frac{\partial(h^2)}{\partial y} dx dy = 0, \end{aligned} \quad (3.6)$$

and application of Green's theorem gives,

$$\oint_{\partial S} huv dy - \oint_{\partial S} \left[hv^2 + \frac{g'h^2}{2} - (f_0 + \beta y)\psi \right] dx + \beta \iint_S \psi dx dy = 0, \quad (3.7)$$

where ∂S is the boundary of S .

Next, we assume that $\psi = 0$ along the wall and note that at least one of the velocity components vanishes on every portion of the boundary ∂S . It then follows from (3.7) that

$$\int_A^B \left[hv^2 + \frac{g'h^2}{2} - (f_0 + \beta y)\psi \right] dx - \int_C^D \frac{g'h^2}{2} dx - \beta \iint_S \psi dx dy = 0. \quad (3.8)$$

Assuming now that, away from the corner, the flow is geostrophic in the cross-current direction, we get [after multiplying the geostrophic relation $(f_0 + \beta y)v = g'\partial h/\partial x$ by h and integrating on the segment AB],

$$(f_0 + \beta y)\psi + C = \frac{g'}{2} h^2, \quad (3.9)$$

where C is the constant to be determined. Evaluating (3.9) at $y = 0$, we get $C = g'h^2(0, y_s)/2$. Combining (3.8) and (3.9) we get our desired expression,

$$\boxed{
\begin{aligned}
& \underbrace{\int_0^L h v^2 dx}_{\text{WBC mom. flux}} + \underbrace{\frac{g'}{2} \int_0^{L_2} (h^2(0, y_s) - h^2(x, 0)) dx}_{\text{Pressure term}} \\
& \quad - \underbrace{\beta \iint_S \psi dx dy}_{\beta \text{ term}} = 0,
\end{aligned}
} \tag{3.10}$$

where L is the boundary current width and L_2 is the zonal extent of our region S . The terms denominations will be discussed shortly (**Fig. 3.2**). It is straightforward to show that, for a southward flowing WBC, the equivalent momentum balance in the region S (bounded by $ABCD$) is,

$$\underbrace{- \int_0^L h v^2 dx}_{\text{WBC mom. flux}} + \underbrace{\frac{g'}{2} \int_0^{L_2} (h^2(x, 0) - h^2(0, y_n)) dx}_{\text{Pressure term}} - \underbrace{\beta \iint_S \psi dx dy}_{\beta \text{ term}} = 0, \tag{3.11}$$

Relations (3.10) and (3.11) show that, on a β -plane, the momentum balance is composed of three terms. The first is the momentum flux imparted by the WBC as it enters the region S . The second is a pressure force and the third is a β -force; together these two forces balance the momentum force of the WBC. It is opportune to point out the various limits of (3.10) and (3.11). The f-plane and β -plane situations are treated separately because, all we shall see shortly, the balance of forces on a β -plane is very different from that on an f-plane.

3.2.2 The f-plane Limit

On an f-plane the pressure force should balance the WBC momentum flux if a steady state is to be established. We shall now show quantitatively that this indeed possible. To see this, as we approach the corner, the magnitude of the velocity along the walls gradually decreases to zero (see Kundu 1990, Chapter 4). Since the walls are a streamline, the Bernoulli function [$B = g'h + (u^2 + v^2)/2$] implies that, the

upper layer thickness increases to a maximum in the corner (**Fig. 3.3** upper panel). Consequently, the pressure force in (3.10) and (3.11) points in the opposite direction

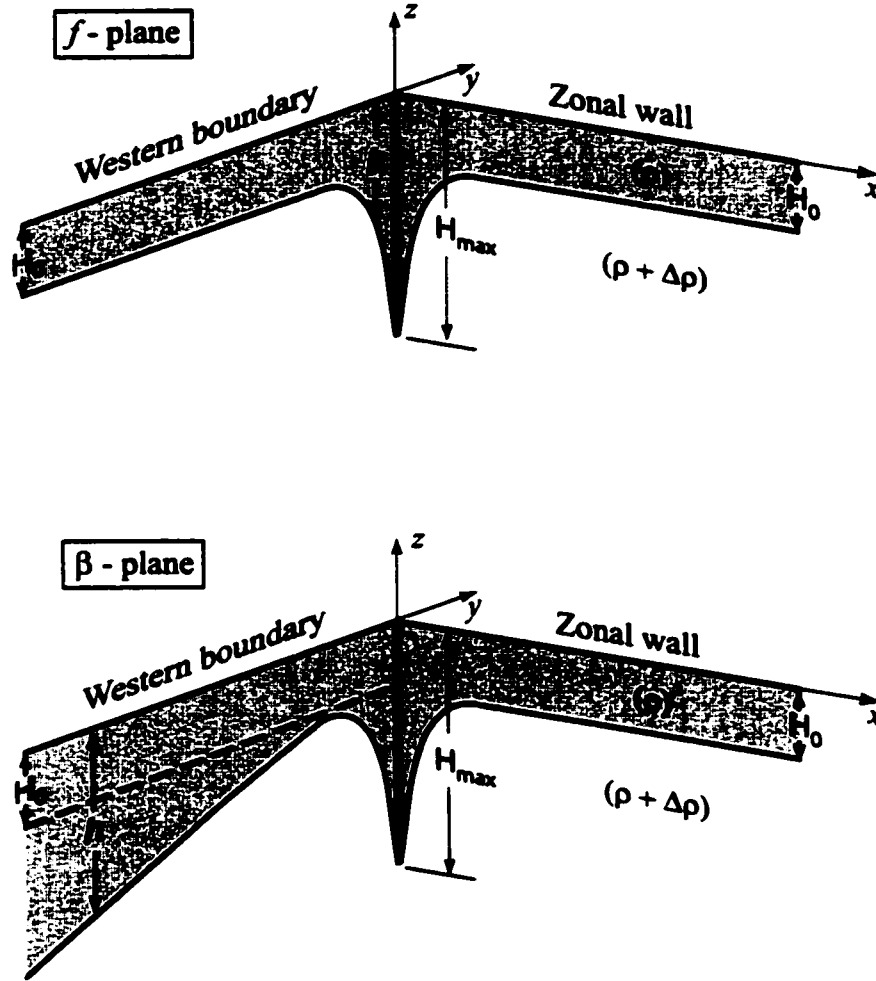


Figure 3.3. Schematic three-dimensional diagram of the upper layer thickness on the boundaries of a northward flowing western boundary current on an f -plane (upper panel) and on a β -plane (lower panel). Note that the upstream near wall thickness is greater in the β -plane case. This is why the eddy is established (see text).

to that of the WBC momentum force and a balance without an eddy appears to be possible. Numerical simulations will later verify this outcome. Note that, in the case of no zonal wall (i.e., the WBC separates due to a vanishing upper layer thickness), the pressure term vanishes (since $h = 0$ on the western boundary and on

the outcropping streamline). As a result, the WBC momentum flux is unbalanced and the f-plane system cannot reach an steady state (see Arruda et al. 2002).

3.2.3 The β -plane Limit

The geostrophic transport relationship $[T = g'(H^2 - h_w^2)/2f]$, where H and h_w are the thicknesses off and on the wall] implies that on a β -plane the near wall thickness of a northward flowing WBC decreases as we proceed downstream along the western boundary (Fig. 3.3 lower panel). We shall shortly see that it is this shallowness which is responsible for the eddy generation. To show this we temporarily assume that no eddy is associated with the turning boundary current on a β -plane and then show that this scenario is impossible. We note that the region where the speed on the zonal wall decreases dramatically near the corner is confined to a very small area (Page and Johnson 1991). In view of this, the average value of h^2 on the zonal wall is much closer to H_0^2 (where H_0 is the value of h as $x \rightarrow \infty$ on $y = 0$) than to H_{max}^2 (i.e., $h^2(0, 0)$).

Consequently, without an eddy, the pressure force points in the same direction as the WBC momentum force and cannot balance it. Taking the zonal extent of S to be $O(R_d)$ we see that the β -term in (3.10) and (3.11) is negligible compared to the WBC momentum flux so that it cannot balance the WBC momentum flux either. The no eddy scenario therefore is impossible. The above conclusion also applies to the case when there is no zonal wall (i.e., and the northward flowing WBC separates from the coast by vanishing the upper layer thickness). This leads to the establishment of the intrusion eddy (Arruda et al. 2002).

3.3 Numerical Simulations for a Flow in a Concave Solid Corner

In this section we shall analyze numerical model simulations to validate the analytical momentum balance (3.10) and (3.11).

3.3.1 Numerical Model Description

We use a reduced gravity version of the isopycnic model developed by Bleck and Boudra (1981,1986) and later improved by Bleck and Smith (1990). This model is suitable for our study since it allows isopycnic outcropping by using the "Flux-Corrected Transport" algorithm (Boris and Book 1973; Zalesak 1979) in the continuity equation.

The equations of motion are the two momentum equations,

$$\begin{aligned}\frac{\partial u}{\partial t} + u \frac{\partial u}{\partial x} + v \frac{\partial u}{\partial y} - (f_0 + \beta y)v &= -g' \frac{\partial h}{\partial x} + \frac{\nu}{h} \nabla \cdot (h \nabla u) \\ \frac{\partial v}{\partial t} + u \frac{\partial v}{\partial x} + v \frac{\partial v}{\partial y} + (f_0 + \beta y)u &= -g' \frac{\partial h}{\partial y} + \frac{\nu}{h} \nabla \cdot (h \nabla v),\end{aligned}$$

and the continuity equation

$$\frac{\partial h}{\partial t} + \frac{\partial(hu)}{\partial x} + \frac{\partial(hv)}{\partial y} = 0,$$

where ν is the friction coefficient.

The model uses the Arakawa (1966) C-grid where the u -velocity points are shifted one-half grid step to the left from h points, the v -velocity points are shifted one-half grid step down from the h points, and vorticity points are shifted one-half grid step down from the u -velocity points. On open boundaries the Orlanski (1976) second-order radiation boundary condition was implemented.

3.3.2 Northward Flowing WBC in a Concave Solid Corner

The parameters for the f -plane experiment E1 and the β -plane experiment E5 are given in Table 3.1.

The Rossby radius of deformation R_d is 26.8 km and the integration domain is a rectangle with the dimensions 750 km \times 1125 km ($28 R_d \times 42 R_d$). The walls

Table 3.1. List of of experiments. The parameters $f_0 = 0.8573 \times 10^{-4} \text{ s}^{-1}$, $g' = 0.014 \text{ m}^2 \text{ s}^{-1}$, $\Delta x = \Delta y = 7.5 \text{ km}$ (horizontal resolution), and $\Delta t = 12 \text{ min}$ (time step) are common for all experiments.

Exp.	Parameters	Figure
E1	$\beta = 0, \nu = 50 \text{ m}^2 \text{ s}^{-1},$ $H = 360 \text{ m}, H_0 = 270.3 \text{ m}$	Figs. 3.4, 3.5, 3.6
E2	$\beta = 0, \nu = 50 \text{ m}^2 \text{ s}^{-1},$ $H = 200 \text{ m}, H_0 = 270.3 \text{ m}$	Figs. 3.7, 3.8, 3.9
E3	$\beta = 1.849 \times 10^{-11} \text{ m}^{-1} \text{ s}^{-1}, \nu = 500 \text{ m}^2 \text{ s}^{-1},$ $H = 360 \text{ m}, H_0 = 270.3 \text{ m}$	
E4	$\beta = 1.849 \times 10^{-11} \text{ m}^{-1} \text{ s}^{-1}, \nu = 500 \text{ m}^2 \text{ s}^{-1},$ $H = 200 \text{ m}, H_0 = 270.3 \text{ m}$	
E5	$\beta = 1.849 \times 10^{-11} \text{ m}^{-1} \text{ s}^{-1}, \nu = 1500 \text{ m}^2 \text{ s}^{-1},$ $H = 360 \text{ m}, H_0 = 270.3 \text{ m}$	Figs. 3.4, 3.5, 3.6
E6	$\beta = 1.849 \times 10^{-11} \text{ m}^{-1} \text{ s}^{-1}, \nu = 1500 \text{ m}^2 \text{ s}^{-1},$ $H = 200 \text{ m}, H_0 = 270.3 \text{ m}$	Figs. 3.7, 3.8, 3.9
E7	$\beta = 1.849 \times 10^{-11} \text{ m}^{-1} \text{ s}^{-1}, \nu = 3000 \text{ m}^2 \text{ s}^{-1},$ $H = 360 \text{ m}, H_0 = 270.3 \text{ m}$	
E8	$\beta = 1.849 \times 10^{-11} \text{ m}^{-1} \text{ s}^{-1}, \nu = 3000 \text{ m}^2 \text{ s}^{-1},$ $H = 200 \text{ m}, H_0 = 270.3 \text{ m}$	
E9	$\beta = 1.849 \times 10^{-11} \text{ m}^{-1} \text{ s}^{-1}, \nu = 1500 \text{ m}^2 \text{ s}^{-1}$ $H_n = 200 \text{ m}, H_s = 360 \text{ m}, H_0 = 270.3 \text{ m}$	Figs. 3.12, 3.13, 3.14

are slippery, and we impose an inflow of 4.8 Sv on the southern boundary (and an outflow with an equal transport on the eastern boundary). **Fig. 3.4** shows the upper layer thickness and streamfunction for the f-plane experiment E1 and and β -plane experiment E5 (Table 3.1) at day 2500, and **Fig. 3.5** shows the upper layer thickness along the western boundary and along the zonal wall.

We see that, as mentioned, on an f-plane the upper layer thickness increases to a maximum near the corner, producing a southward pressure force. The downstream upper layer thickness along the zonal wall (for the f-plane experiment E1) is 270.7 m which is in excellent agreement with our specified value of 270.3 for H_0 as should be

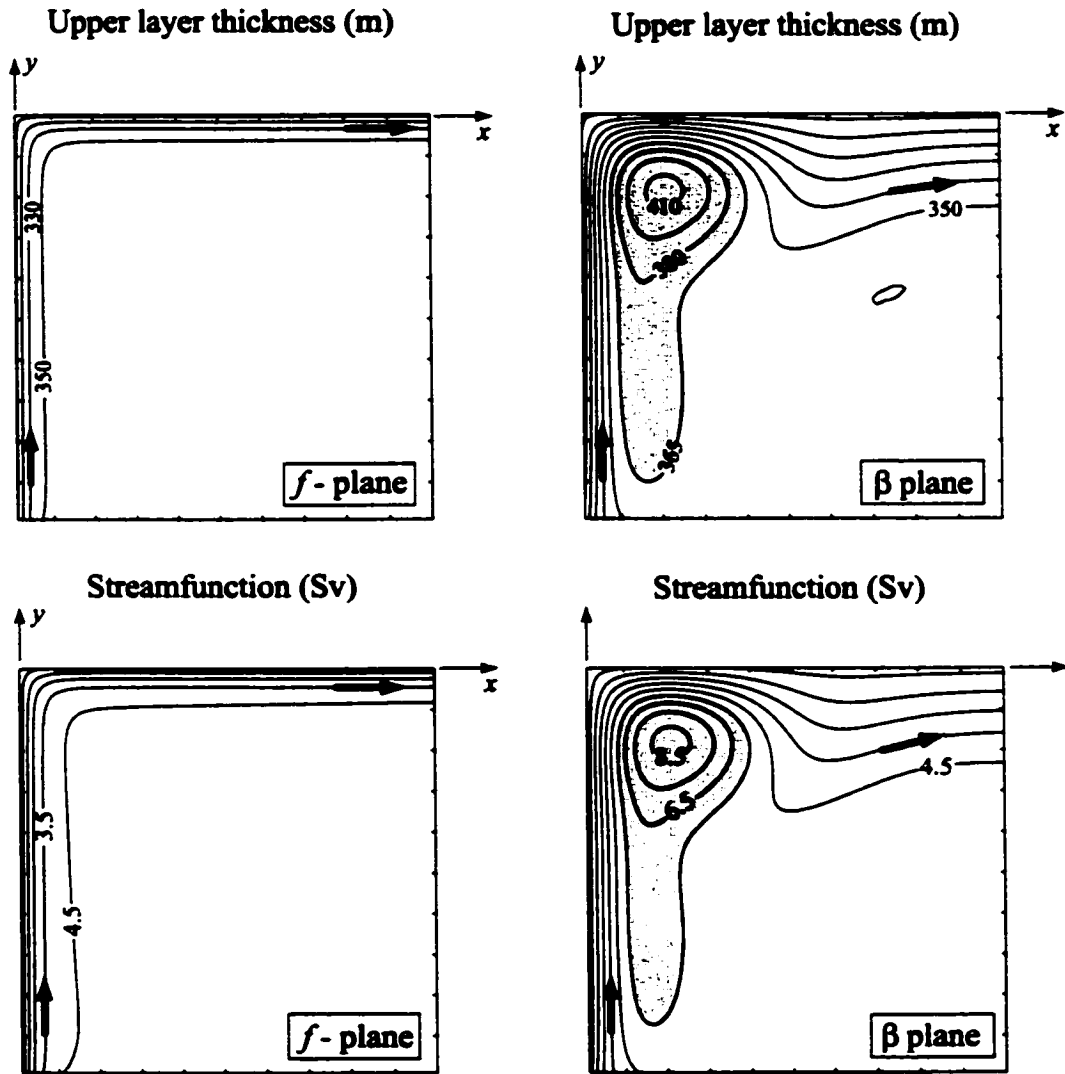


Figure 3.4. Upper layer thickness contours (upper left) and streamfunction contours (lower left) for the f -plane experiment E1 (Table 3.1) at day 2500; Upper layer thickness contours (upper right) and streamfunction contours (lower right) for the β -plane experiment E3 (Table 3.1) at day 25000. The contour spacing is 20 m for the upper layer thickness and 15 Sv for the stream function. The axis marks are 10 grid points (75 km) apart. Areas within the closed contours are shaded.

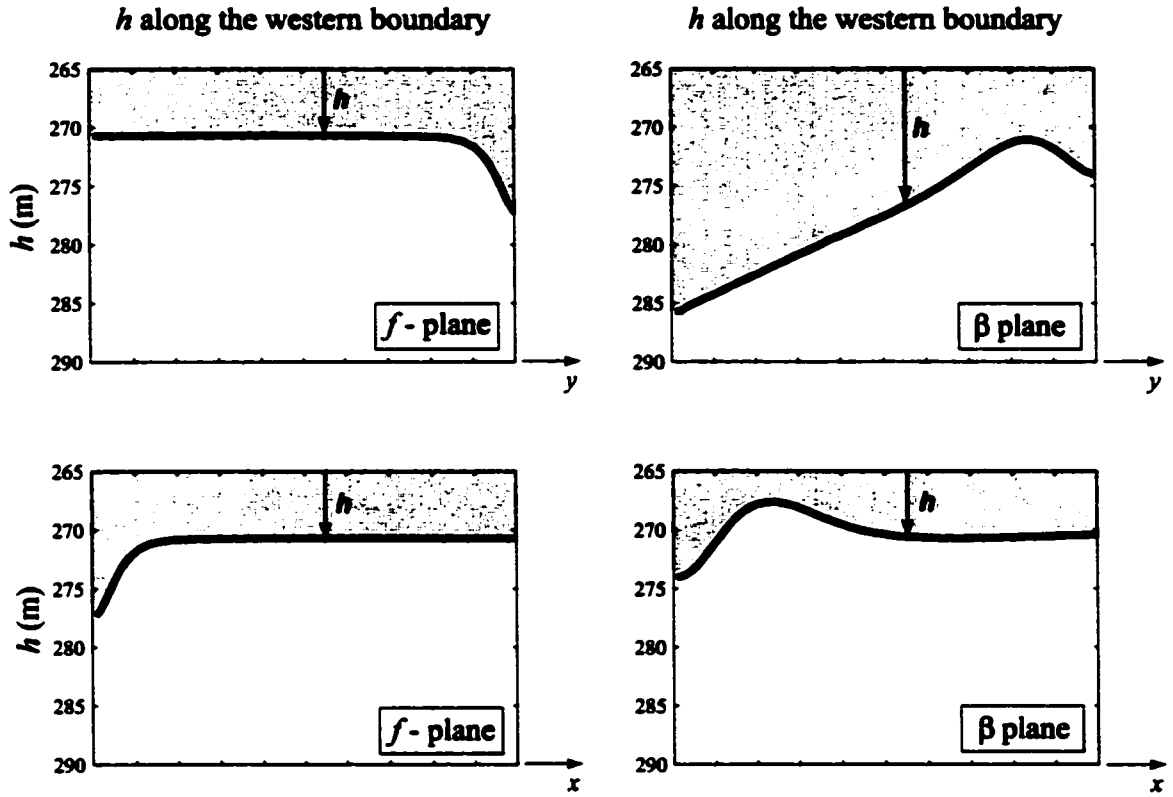


Figure 3.5. f -plane upper layer thickness h (in meters) along the western boundary (upper left) and along the zonal wall (lower left) at day 2500; β -plane upper layer thickness h (in meters) along the western boundary (upper right) and along the zonal wall (lower right) at day 25000. Shaded area is the upper layer. The horizontal axis marks are 10 grid points (75 km) apart.

the case. (Recall that the values of H and H_0 set the WBC inflow.) It is opportune to point out that, since the numerical model is implemented on a C-grid there is no h -points on the boundaries. Hence, we estimate the upper layer thickness on the boundaries by geostrophy using the values of h and velocity component parallel to the boundary at half grid size away from the boundary.

Fig. 3.6 shows the terms in (3.10) for the f -plane experiment E1 (Table 3.1). We see that the pressure force points southward and balances the northward momentum flux of the WBC [showing that the inviscid balance (3.10) is attained]. We also

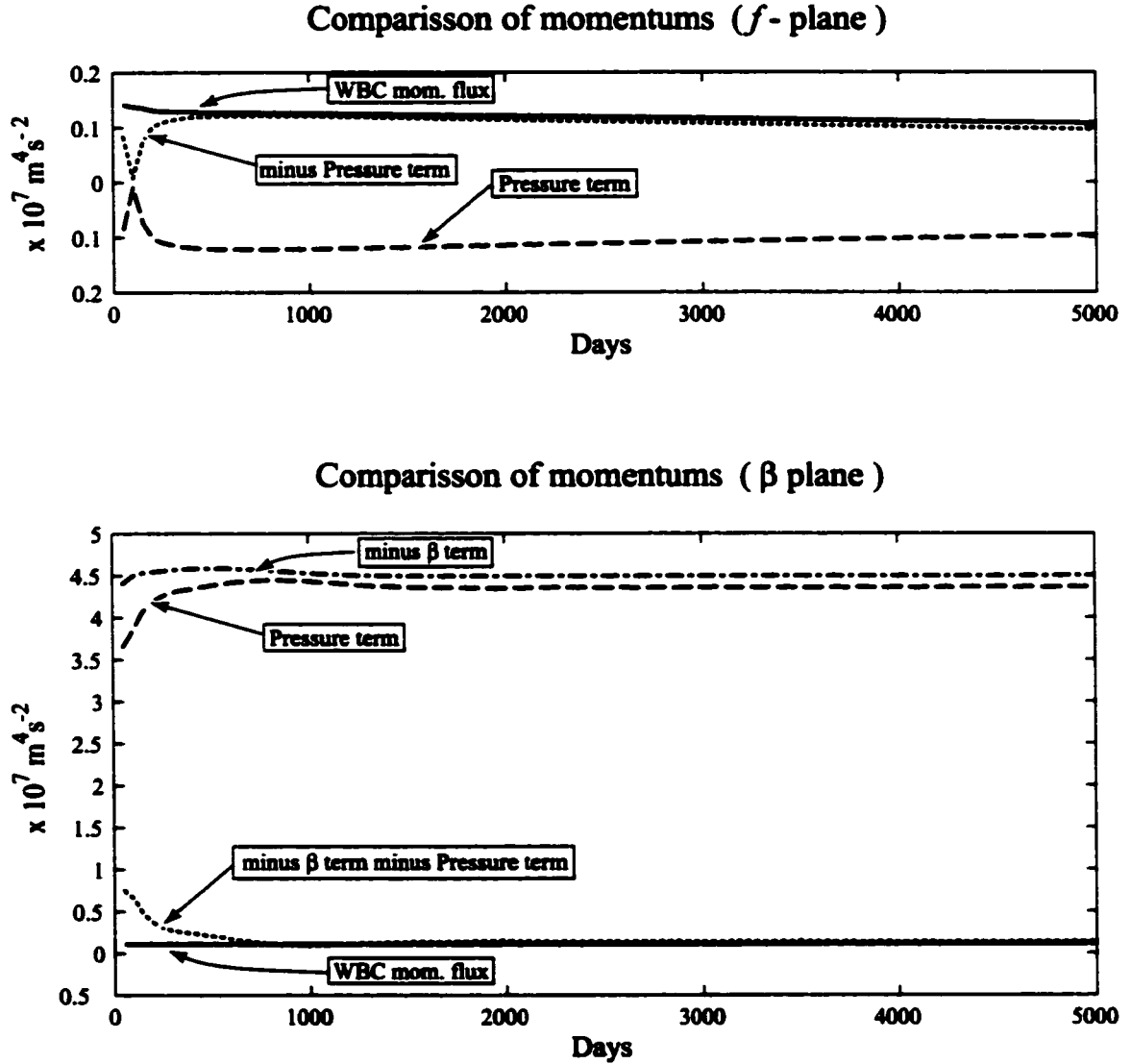


Figure 3.6. Terms of the momentum balance (3.10) computed from the f -plane experiment E1 (upper panel), and the β -plane experiment E3 (lower panel). Note that by day 500 for the f -plane run and day 800 for β -plane run the steady state balance holds.

see that, as mentioned, in this f-plane case, no eddy is necessary to achieve the momentum balance.

When β is introduced (**Fig. 3.4**) an anticyclonic eddy (attached to the curving flow) is generated. Also, as seen in **Fig. 3.5**, the pressure force points northward since the upper layer thickness along the western boundary is larger than its average value on the zonal wall (270.2 m). In addition, note that the thickening of the upper layer at the corner is compensated by the eddy so that the average value of the upper layer thickness on the zonal wall is 270.2 m, which is indistinguishable from the initial value for H_0 (270.3 m). This numerical observation will be used shortly in our detailed analytical derivations. **Fig. 3.6** shows that, the combination of β and the pressure terms is a southward force which balances the northward momentum force of the WBC. With the aid of (3.12) and a scale analysis that we shall perform later, we shall show that the eddy is the main contributor to the combined β and pressure terms. The eddy's β -force is due to the particles circulation within the anticyclonic eddy which causes a greater Coriolis force on the northern portion of the eddy than on the southern.

To investigate the role of friction in the β -plane simulations we run experiments E3 and E7 (not shown) with lower and higher friction coefficients. In the first case, the system did not reach an steady state while in the second case friction smoothed out the eddy, making it weaker and meridionally elongated.

3.3.3 Southward Flowing WBC in a Concave Solid Corner

The parameters for the f-plane experiment E2 and the β -plane experiment E6 are given in Table 3.1. The Rossby radius of deformation R_d is 20 km and the integration domain is a rectangle with the dimensions 750 km \times 1125 km ($37.5 R_d \times 56.3 R_d$). As before, the walls are slippery, and we impose an inflow of 2.9 Sv on the northern boundary (and leave the western boundary open).

Fig. 3.7 shows contour plots of the upper layer thickness and streamfunction at

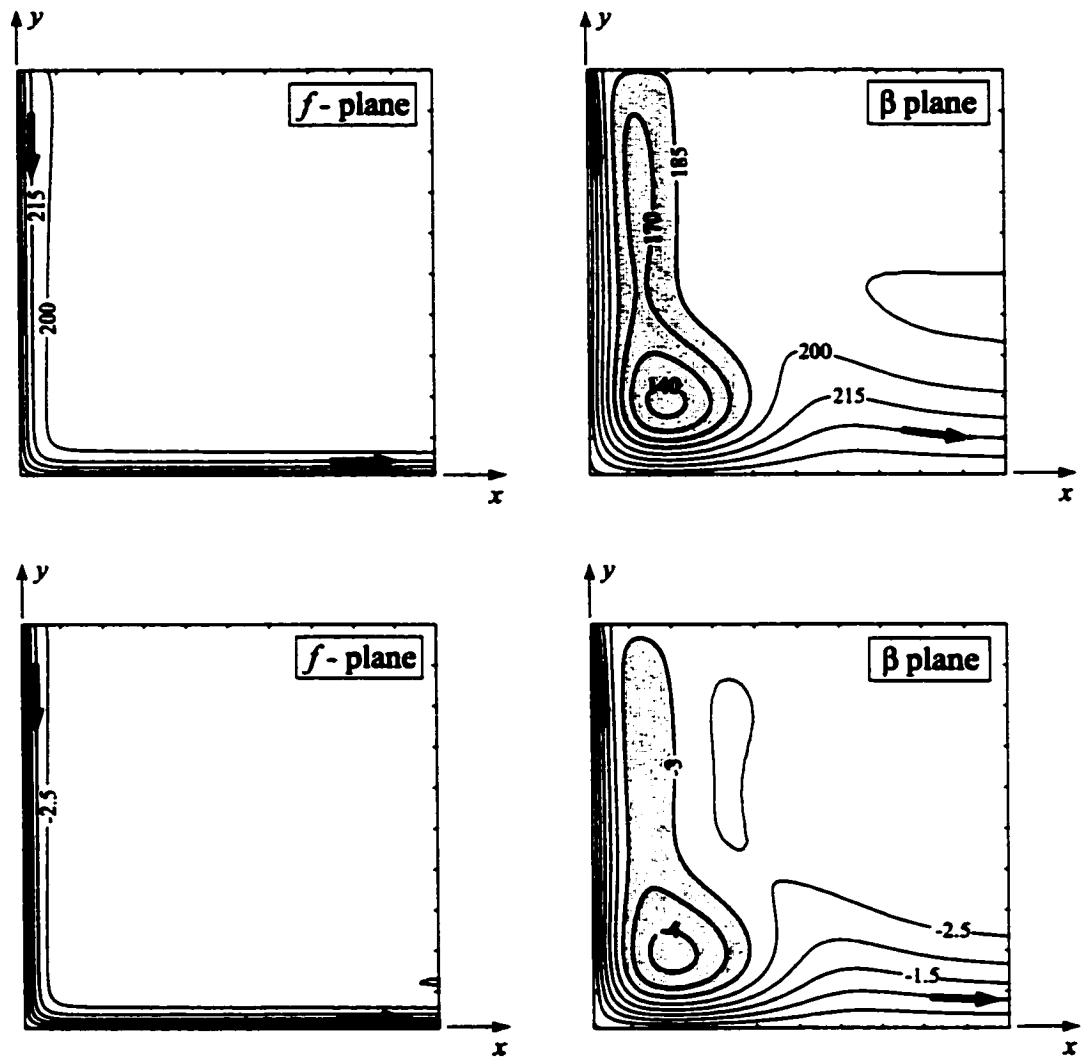


Figure 3.7. Upper layer thickness contours (upper left) and streamfunction contours (lower left) for the f -plane experiment E2 (Table 3.1) at day 2500; Upper layer thickness contours (upper right) and streamfunction contours (lower right) for the β -plane experiment E4 (Table 3.1) at day 25000. The contour spacing is 20 m for the upper layer thickness and 15 Sv for the stream function. The axis marks are 10 grid points (75 km) apart. Areas within the closed contours are shaded. Note the diagonal symmetry of the f -plane runs and the diagonal asymmetry of the β -plane runs.

day 2500 for the f -plane experiment (E2) and the β -plane experiment (E6). Similarly, **Fig. 3.8** displays the upper layer thickness along the western boundary and along

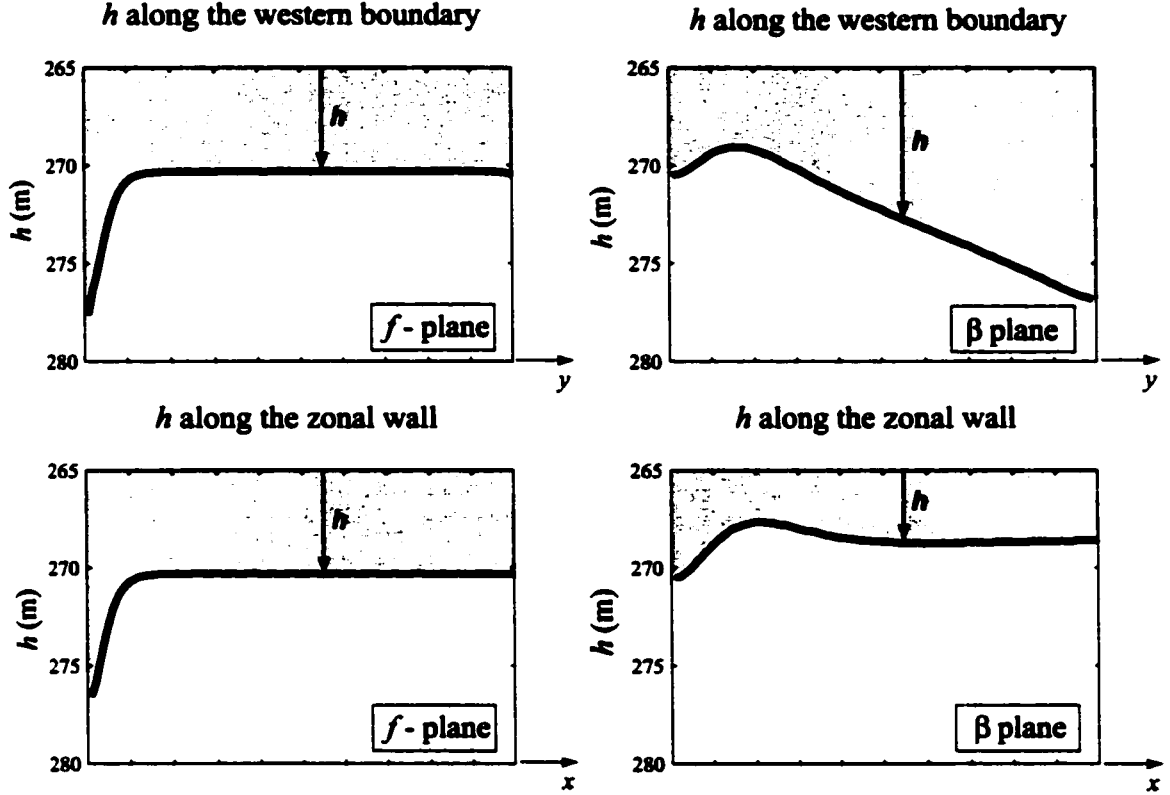


Figure 3.8. f -plane upper layer thickness h (in meters) along the western boundary (upper left) and along the zonal wall at day 2500; β -plane upper layer thickness along the western boundary (upper right) and the zonal wall (lower right) at day 25000. Shaded area is the upper layer. The horizontal axis marks are 10 grid points (75 km) apart.

the zonal wall at the same day. In the f -plane situation, the upper layer thickness increases to a maximum in the corner, producing a northward pressure force which, according to **Fig. 3.9**, balances the southward momentum force of the WBC. This indicates that the inviscid balance (3.11) is attained.

When β is introduced (**Fig. 3.7**), a cyclonic eddy (attached to the curving flow) is formed. Also, as seen in **Fig. 3.8**, the pressure force points southward since the upper layer thickness along the western boundary is larger than its average value

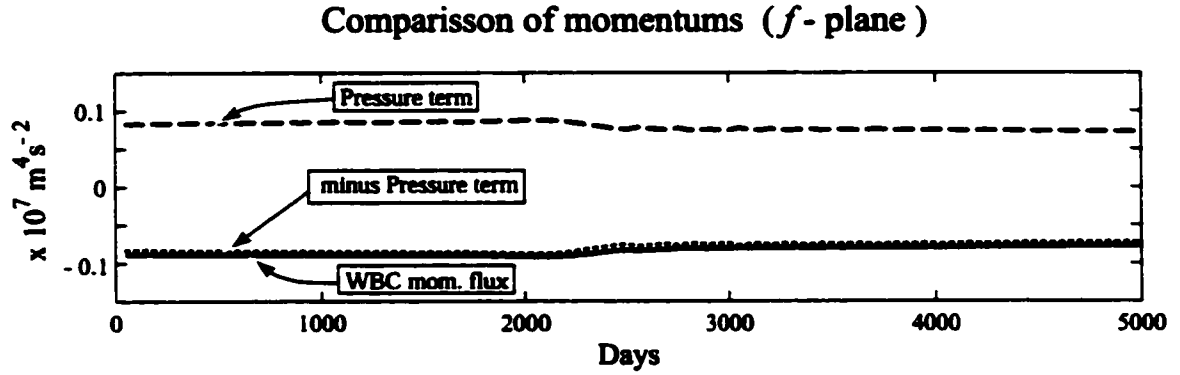


Figure 3.9. Terms of the momentum balance (3.11) computed from the f -plane experiment E2 (upper panel), and the β -plane experiment E4 (lower panel). Note that the f -plane run reaches a steady state right away [whitin a period of $O(f^{-1})$] while the β -plane run takes 500 days to reach a steady state.

on the zonal wall (268.6 m). The average value of the upper layer thickness along the zonal wall is 268.6 m which coincides with its average value at the last 50 grid points, showing that the thickening at the corner (associated with Bernoulli function conservation) is compensated by the shallowness produced by the eddy. Again, this will be used shortly in our analytical derivations. As seen in **Fig. 3.9**, the combination of the β and the pressure terms is a northward force which balances the southward momentum force of the WBC.

3.4 Estimates of the Eddy Radius Generated by a Flow in a Concave Solid Corner on a β -plane

3.4.1 Formulation

An alternative form of the momentum balance relation for a northward flowing WBC in a concave solid corner (3.10) can be derived as follows. At $x \rightarrow \infty$ the zonal flow is geostrophic in the y -direction so that,

$$(f_0 + \beta y) \frac{\partial \psi}{\partial y} = \frac{g'}{2} \frac{\partial(h^2)}{\partial y},$$

and an integration in y gives,

$$(f_0 + \beta y) \psi \Big|_{y_*}^0 - \beta \int_{y_*}^0 \psi_{\infty} dy = \frac{g'}{2} h^2 \Big|_{y=y_*}^{y=0}, \quad x \rightarrow \infty$$

where ψ_{∞} (which is a function of y) is the streamfunction at $x \rightarrow \infty$, and y_* is the y -component of point *A* (**Fig. 3.2** upper left panel). Since $\psi = 0$ at $y = 0$ it follows from the above relationship that C in (3.9) is,

$$C = \frac{g'}{2} H_0^2 + \beta \int_{y_*}^0 \psi_{\infty} dy,$$

where H_0 is the value of h along the zonal wall as $x \rightarrow \infty$. Hence, (3.8) can be written as,

$$\int_0^L h v^2 dx + \frac{g'}{2} \int_0^{L_2} (H_0^2 - h^2(x, 0)) dx - \beta \iint_S (\psi - \psi_\infty) dx dy = 0, \quad (3.12)$$

It is straightforward to show that, for a southward flowing WBC,

$$-\int_0^L h v^2 dx + \frac{g'}{2} \int_0^{L_2} (h^2(x, 0) - H_0^2) dx - \beta \iint_S (\psi - \psi_\infty) dx dy = 0. \quad (3.13)$$

In the next two subsections we shall use (3.12) and (3.13) to derive analytical expressions for the eddy radius. We shall treat the cases of a northward and a southward flowing WBC separately (because the scales are different).

3.4.2 Northward Flowing WBC

As pointed out earlier, the numerical simulations indicate that the average value of the upper layer thickness on the zonal wall is approximately H_0 (the value of h on the zonal wall as $x \rightarrow \infty$). Although we cannot come up with any argument explaining why this should be so, we shall use this info for our calculations and neglect the second term in (3.12). Recall that, on an f-plane, the pressure term is negative and that a neglect of a negative term would overestimate the eddy size. With the above neglect, the momentum balance (3.12) reduces to,

$$\int_0^L h v^2 dx = \beta \iint_S \hat{\psi} dx dy, \quad (3.14)$$

where L is the boundary current width, $\hat{\psi} = \psi - \psi_\infty$ and ψ_∞ is the streamfunction at $x \rightarrow \infty$.

Note that the integrand of the second integral vanishes as $x \rightarrow \infty$ and, consequently, the integral does not change when the zonal extent of S is increased (as should be the case).

3.4.2.1 Scaling Assuming nonlinear dynamics we take the following scales:

$$L \sim O(R_d); \quad \Delta H = (H - H_0) \sim O(H); \quad v \sim O((g'H)^{1/2});$$

$$\hat{\psi} \sim O\left(\frac{g'H^2}{f_0^2}\right) \text{ in the current;}$$

$$\hat{\psi} \sim O\left(\frac{g'H_e^2}{f_0^2}\right) \text{ in the eddy,}$$

where $R_d = (g'H)^{1/2}/f_0$ and H_e is the depth scale for the eddy. Note that the second term in (3.14) is non zero only in the eddy and the boundary current (because the streamfunction ψ coincides with ψ_∞ in the interior). Note that the assumption $\Delta H \sim O(H)$ implies that the momentum flux of the boundary current is non negligible (otherwise the quasi-geostrophic dynamics would take place and the momentum flux goes to zero).

Using the above scales, each term of (3.14) can be scaled as,

$$\int_0^L hv^2 dx \sim O(f_0^2 H R_d^3) \quad (3.15)$$

$$\beta \iint_{WBC} \hat{\psi} dx dy \sim O(\beta f_0 H R_d^3 |y_s|) \quad (3.16)$$

$$\beta \iint_{eddy} \hat{\psi} dx dy \sim O(\beta f_0 H_e R_{de}^4), \quad (3.17)$$

where y_s is the y -component of point A (Fig. 3.2 upper left panel), and $R_{de} = (g'H_e)^{1/2}/f_0$. Taking

$$R_{de} \sim O\left(\frac{R_d}{\epsilon^{1/6}}\right), \text{ and} \quad (3.18)$$

$$|y_s| \sim O(R_{de}), \quad (3.19)$$

where $\epsilon = \beta R_d / f_0 \ll 1$, we see that there is a balance between (3.15) and (3.17) and that the ratio between (3.16) and the two other terms is $O(\epsilon^{5/6})$. Two additional comments should be made with regard to (3.18). First, as is frequently the case, the

scaling may conceal potentially large numbers such as powers of the known $2\sqrt{2}$ ratio between the eddy radius and the Rossby radius (see, e.g. Nof 1981; Killworth 1983). Second, the $1/6$ power of ϵ implies that, for most cases, R_{de} will be comparable to R_d (though it will be larger). Note that similar scales were found by Pichevin and Nof (1996) and Nof and Pichevin (1999).

Given the above scales we now introduce the following nondimensional parameters. For the WBC entering the integration area S through AB (Fig. 3.2 upper left panel), the scaled variables are,

$$\begin{aligned} x^* &= x/R_d; & y^* &= y/R_{de}; & v^* &= v/(f_0 R_d) \\ h^* &= h/H; & R_d &\equiv (g'H)^{1/2}/f_0, \end{aligned} \quad (3.20)$$

while for the eddy they are,

$$\begin{aligned} x_e^* &= x/R_d; & y_e^* &= y/R_{de}; & h_e^* &= \frac{h}{H \left(\frac{R_{de}}{R_d} \right)^2}; & \psi_e^* &= \frac{\hat{\psi}}{(g'H_e^2/f_0)}; \\ R_{de} &= R_d/\epsilon^{1/6}; & \epsilon &= \beta R_d/f_0. \end{aligned} \quad (3.21)$$

3.4.2.2 Expansions Substitution of (3.20) and (3.21) into (3.14) (noting that, according to our scales analysis, the second integral is calculated only over the eddy) gives,

$$\int_0^{L^*} h^* (v^*)^2 dx^* = \iint_{S_e} \psi_e^* dx_e^* dy_e^*, \quad (3.22)$$

where S_e is the closed region encompassed by the eddy. Each dependent variable is expanded in a power series of the small parameter $\epsilon^{1/6}$, implying that the basic states for the WBC and the eddy are subject to perturbations of $O(\epsilon^{1/6})$. For simplicity we assume that the eddy's basic state has a circular shape.

From (3.22), the leading order balance is,

$$\int_0^{L^{(0)}} h^{(0)} (v^{(0)})^2 dx^* = \iint_{S_e} \psi_e^{(0)} dx_e^* dy_e^*, \quad (3.23)$$

where $h^{(0)}$, $(v^{(0)})$, $\psi_e^{(0)}$, and $L^{(0)}$ are the zeroth-order approximations of the respective dependent variables.

3.4.2.3 Basic state for the northward flowing WBC and anticyclonic eddy Taking the flow in to have zero potential vorticity (i.e., the highly nonlinear case) we find that the solutions are straightforward despite the nonlinearity. Note that, with this assumption, the interior of the basin is motionless with thickness H because the velocity is zero along the bounding streamline of the current offshore (Anderson and Moore 1979). As we shall see later, in this limit, the obtained estimate will be a lower bound on the eddy radius.

Zero potential vorticity current For a zero-potential vorticity northward flowing boundary current,

$$v = \begin{cases} f(L-x) & , \quad x \leq L \\ 0 & , \quad x > L \end{cases} \quad (3.24)$$

$$h = \begin{cases} H - \frac{f^2(L-x)^2}{2g'} & , \quad x \leq L \\ H & , \quad x > L \end{cases} \quad (3.25)$$

where L is the width of the current.

Since the transport of the geostrophic boundary current through the zonal segment AB must be the same as the transport of the separated geostrophic current through the meridional segment BC (Fig. 3.2 upper left panel), we have,

$$\frac{g'}{2f} (H^2 - h^2(0, y_*)) = \frac{g'}{2f_0} (H^2 - H_0^2). \quad (3.26)$$

From (3.25) it follows that along the wall ($x = 0$),

$$h(0, y) = H - \frac{f^2 L^2}{2g'}, \quad y < 0. \quad (3.27)$$

Combining (3.26) and (3.27), we get an expression for the upstream boundary current width L ,

$$L = 2^{1/2} R_d \left\{ 1 - \left[1 - \frac{f}{f_0} \left(\frac{H^2 - H_0^2}{H^2} \right) \right]^{1/2} \right\}^{1/2}. \quad (3.28)$$

Non-dimensionalizing (3.28) and using our scales, it follows that, at leading order,

$$L = 2^{1/2} R_{dc}, \quad (3.29)$$

where $R_{dc} = [g'(H - H_0)]^{1/2}/f_0$ is the (upstream) boundary current Rossby radius.

So, at leading order for the zero potential vorticity boundary current

$$v = \begin{cases} f_0(L - x) & , \quad x \leq L \\ 0 & , \quad x > L \end{cases} \quad (3.30)$$

$$h = \begin{cases} H - \frac{f_0^2(L - x)^2}{2g'} & , \quad x \leq L \\ H & , \quad x > L, \end{cases} \quad (3.31)$$

Zero potential vorticity eddy Since the eddy's upper layer thickness scale is $H_e = H(R_{de}/R_d)^2 = \epsilon^{-1/3}H$, we can take $h_e = 0$ along the eddy's boundary. Then, for the zero potential vorticity eddy,

$$v_\theta = -\frac{f_0 r}{2}, \quad r \leq R \quad (3.32)$$

$$h_e = \hat{h} \left(1 - \frac{r^2}{R^2} \right), \quad r \leq R, \quad (3.33)$$

$$\psi_e = \frac{f_0^3}{2^6 g'} (R^2 - r^2)^2, \quad r \leq R. \quad (3.34)$$

where v_θ is the orbital speed, r is the radial distance from the center of the eddy, h_e is the eddy's upper layer thickness, \hat{h} is the eddy's layer thickness at the center, and $R = (8g'\hat{h})^{1/2}/f_0$.

Radius of anticyclonic eddy in a concave solid corner on a β -plane Substituting (3.29)-(3.34) into (3.23), the desired zeroth-order anticyclonic eddy radius is found to be,

$$R = 2 \left(\frac{2^{3/2}}{\pi} \right)^{1/6} \left(\frac{H - H_0}{H} \right)^{1/2} \left(\frac{H}{H - H_0} - \frac{3}{5} \right)^{1/6} \frac{R_d}{\epsilon^{1/6}} \quad (3.35)$$

Relation (3.35) is an analytical estimate for the eddy radius based on the momentum balance approach [note that the parameter $(2^{3/2}/\pi)^{1/6} \cong 1$]. It relates the eddy size to the known upstream parameters. It is a lower bound, because the zero potential vorticity eddy has the strongest nonlinearity (due to the highest steepness) and, as a consequence, it also has the smallest radius.

To validate the analytical relation (3.35) we determine analitically the numerical eddy radius using the parameters of numerical experiment E5 (Table 3.1), getting $\epsilon^{1/6} = 0.42$ and $R = 2.84 R_d$. Taking the 6.5 Sv streamline as the eddy boundary (**Fig. 3.4**) we find that $3.7 R_d$ is the average numerical radius between days 1500 and 5000, which is in very good agreement with the above analytical estimate ($2.84 R_d$).

In the next subsection we shall derive the radius estimate for the cyclonic eddy formed as a southward flowing WBC in a concave solid corner on a β -plane.

3.4.3 Southward Flowing WBC

For a southward flowing current in a concave solid corner, we proceed in a similar fashion to that of the previous section, pointing out that in this case the eddy upper layer thickness scales with H , so that the obtained eddy size scale is $R_d/\epsilon^{1/2}$. We take the zeroth-order (basic state) boundary current and eddy to have uniform

potential vorticity and use the Csanady (1979) solution for a uniform potential vorticity cyclonic eddy (**Fig. 3.10**). Specifically, the current is expanded around

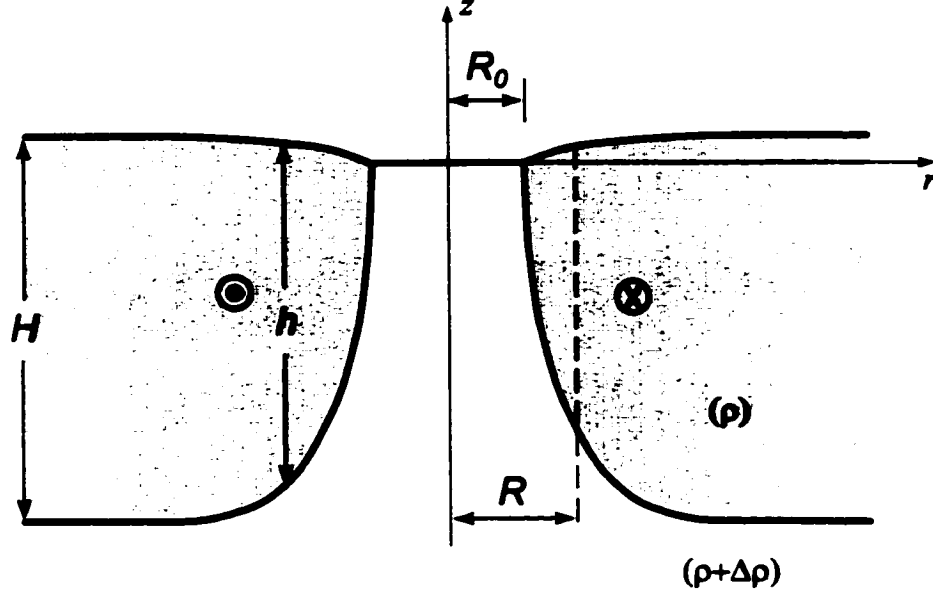


Figure 3.10. Schematic representation of a radial section of the Csanady (1979) cyclonic eddy. R_0 is the radius of the outcropped region and R is the eddy mean radius. H is the undisturbed thickness at $r \rightarrow \infty$.

the f-plane solution with potential vorticity depth H . Doing so, we get

$$\frac{\epsilon}{2} \left(\frac{R_0}{R_d} \right)^2 + \int_{R_0/R_d}^{\infty} \epsilon \left[1 - \left(1 - \frac{K_0(r/R_d)}{K_0(R_0/R_d)} \right)^2 \right] r' dr' = \frac{1}{6\pi} \left(\frac{H_0 - H}{H} \right)^2 \left(\frac{g'(H + 2H_0)/f_0^2}{R_d^2} \right), \quad (3.36)$$

where K_0 and K_1 are Bessel functions of second kind and R_0 is the radius of the outcropped region. By solving (3.36) we can obtain R_0 . If we replace the two terms on the left hand side of (3.36) by $\frac{\epsilon}{2} \left(\frac{R}{R_d} \right)^2$ where R is defined as the mean eddy radius [it larger than R_0 , because K_0 is a positive decaying function, so that the integrand in the second tem of (3.36) is positive], we get

$$R = \left(\frac{1}{3\pi} \right)^{1/2} \left(\frac{H_0 - H}{H} \right) \left(\frac{H + 2H_0}{H} \right)^{1/2} \frac{R_d}{\epsilon^{1/2}}. \quad (3.37)$$

This eddy radius is compatible with our scales where the eddy streamfunction scales with $g'H^2/f_0$. As in the anticyclonic case, (3.37) is a lower bound, because the uniform potential vorticity eddy outcrops along a contour of radius R_0 (where the streamfunction reaches the minimum value of $-g'H^2/2f_0$). From there the streamfunction increases to zero very rapidly with a concentrated contribution of the β -term in a small region.

To validate (3.37) we estimate the eddy radius using the parameters of the numerical experiment E6 (Table 3.1), obtaining $\epsilon^{1/2} = 0.06$, $R_0 = 1.92 R_d$, and $R = 3.35 R_d$. Taking the minus 3.5 Sv streamline as the eddy boundary in E6 (Fig. 3.7) we estimate $4.28 R_d$ as the average numerical radius between days 1500 and 5000. This is in good agreement with the analytical estimate ($3.35 R_d$). Estimates of the eddy radius generated by a flow in a concave

3.5 The Collision Problem

In this section we will examine the full collision problem of opposing western boundary currents on a β -plane. Recall that, as in the earlier case mentioned above, the variation of the Coriolis parameter is very important here as, for an analogous f-plane situation, Agra and Nof (1993) showed that net momentum flux of the colliding currents is balanced, i.e., no eddy is necessary for the momentum balance to hold.

3.5.1 Formulation

Consider two opposing WBCs (Fig. 3.11). We shall denote the northward flowing current as the "main current" and the southward flowing one as the "counter

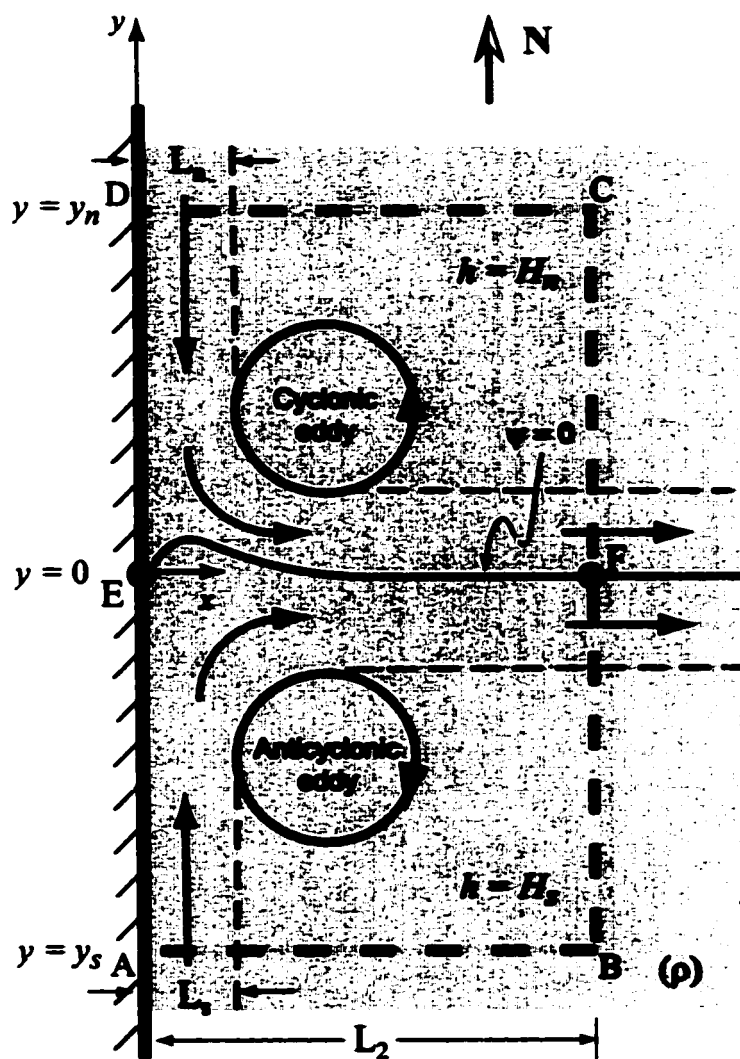


Figure 3.11. Schematic diagram of the collision between a northward flowing boundary current (Main current) and a southward flowing boundary current (Counter current) on a β -plane. After the collision the two currents merge into a joined offshore current. All the currents are embedded in the upper layer of density ρ . Far east of the western boundary and a few Rossby radius away from the dividing streamline ($\psi = 0$) the upper layer the thickness has value of H_s in the main current side and H_n in the counter current side.

current". At some point on the western boundary the currents collide and veer offshore as a joined current. We place the origin of our coordinate system at the collision (stagnation) point on the western boundary and assume that, far east of the western boundary and a few Rossby radius away from the dividing streamline the upper layer thickness has value of H_s in the main current side and H_n in the counter current side.

Assuming a steady state and integrating (after multiplying by h) the steady, inviscid nonlinear y -momentum equation over the fixed region S bounded by $ABCD$, we get

$$\boxed{
 \underbrace{\int_0^{L_s} h v^2 dx - \int_0^{L_n} h v^2 dx}_{\text{Net mom. flux}} + \underbrace{\frac{g'}{2} \int_0^{L_2} (h^2(0, y_s) - h^2(0, y_n)) dx}_{\text{Pressure term}} - \underbrace{\beta \iint_S \psi dx dy}_{\beta \text{ term}} = 0, \quad (3.38)$$

where L_s and L_n are the main current and counter current widths, S is the integration region bounded by $ABCD$ (Fig. 3.11), L_2 is the zonal width of S , and y_s and y_n are the y -coordinates of the southern and northern boundaries of S .

As before, (3.38) represents three forces, the net momentum flux (first two terms combined) imparted by the boundary currents as they enter the integration domain S through AB and CD (Fig. 3.11), a pressure force (third term) which is due to the difference in the upper layer thickness A and D and a β -force (last term).

To apply our previous analytical approach to the collision problem, we divide the momentum balance (3.38) into the two sub-dominans S^+ and S^- , north and south of $\psi = 0$, respectively. After some algebra we obtain,

$$\boxed{
\underbrace{\int_0^{L_s} h v^2 dx}_{\text{Main current mom. flux}} + \underbrace{\frac{g'}{2} \int_0^{L_2} (h^2(0, y_s) - h^2(x, \phi)) dx}_{\text{Pressure term}} - \underbrace{\beta \iint_{S^-} \psi dx dy}_{\beta \text{ term}} = 0, \quad (3.39)
}$$

and

$$\boxed{
\underbrace{- \int_0^{L_n} h v^2 dx}_{\text{Counter current mom. flux}} + \underbrace{\frac{g'}{2} \int_0^{L_2} (h^2(x, \phi) - h^2(0, y_n)) dx}_{\text{Pressure term}} - \underbrace{\beta \iint_{S^+} \psi dx dy}_{\beta \text{ term}} = 0, \quad (3.40)
}$$

which, as expected, have a mutual term $\frac{g'}{2} \int_0^{L_2} h^2(x, \phi) dx$ where $y = \phi(x)$ is cartesian representation of the curve $\psi = 0$. Eqs. (3.39) and (3.40) can also be written as,

$$\int_0^{L_s} h v^2 dx + \frac{g'}{2} \int_0^{L_2} (H_0^2 - h^2(x, \phi)) dx - \beta \iint_{S^-} (\psi - \psi_\infty) dx dy = 0, \quad (3.41)$$

and

$$- \int_0^{L_n} h v^2 dx + \frac{g'}{2} \int_0^{L_2} (h^2(x, \phi) - H_0^2) dx - \beta \iint_{S^+} (\psi - \psi_\infty) dx dy = 0, \quad (3.42)$$

where H_0 is the value of the upper layer thickness on $\psi = 0$ as $x \rightarrow \infty$, and ψ_∞ (a function of y only) is the limit of ψ as $x \rightarrow \infty$.

We shall see in the next subsection that the second term in (3.41) and (3.42) is approximately zero and that, consequently our solid corner solutions will also be valid here.

3.5.2 Numerical Simulations for the Collision Problem

The parameters for the collision experiment E9 on a β -plane (Table 3.1) are identical to those used for experiments E5 and E6 for the concave corner. The Rossby radius of deformation R_d is 20 km for the counter current and 26.8 km for the main current. The integration domain is a rectangle with the dimensions of 1500 km \times 1125 km. The walls are slippery and we impose inflows of 4.8 Sv in the southern boundary (main current) and 2.9 Sv in the northern boundary (counter current). On the western boundary we impose an outflow that matches the inflow total transport.

Fig. 3.12 shows contour plots of the upper layer thickness and streamfunction for experiment E9 at day 2500. It is evident that an anticyclonic eddy is formed south of the joined offshore current and a cyclonic eddy north of it. **Fig. 3.13** shows the upper layer thickness along the western boundary (upper panel) and along the $\psi = 0$ streamfunction (lower panel). Note the similarity with **Figs. 3.5** and **3.8** for the β -plane experiments E5 and E6. The pressure force points in the same direction than the momentum flux (in each of the individual sub-domains). Therefore, the eddies are necessary in order to reach the integrated momentum balances in S^- and S^+ individually. The average value for the upper layer thickness on the zero streamfunction is 270.8 m while the mean value outside the eddy influence area is 271 m (**Fig. 3.13**), showing that, even in the collision problem, the assumption that the second term in (3.41) and (3.42) vanishes agrees with the numerical simulations.

Fig. 3.14 shows the numerical estimates for the terms in (3.38) (upper panel), (3.39) (middle panel), and (3.40) (lower panel). In all the cases the inviscid momentum balances hold. The analytical estimates for the flow inside a concave corner can also be used here, by considering the $\psi = 0$ streamfunction as a “wall” dividing the basin in two parts (the main current side and the counter current side). Taking the minus 4 Sv streamline as the boundary of the cyclonic eddy and the

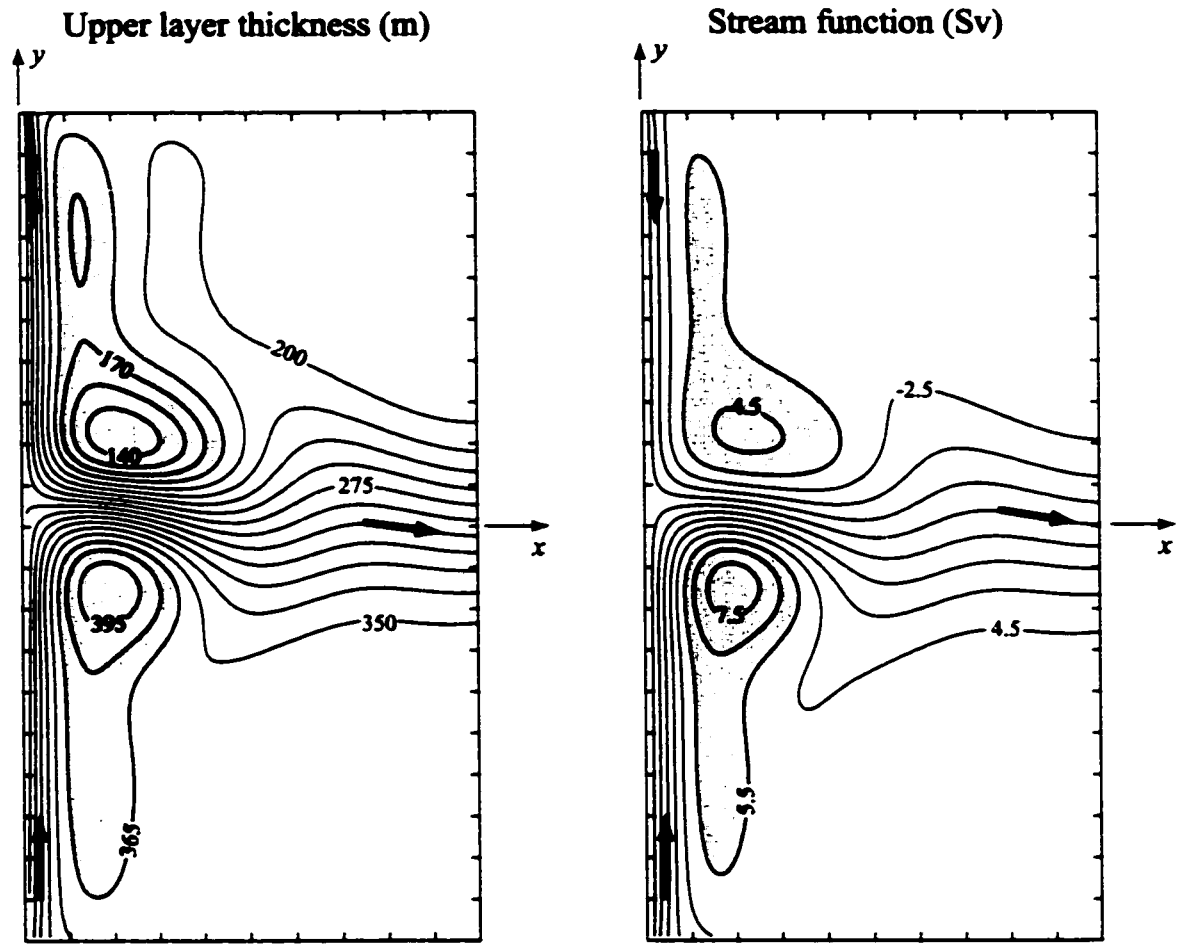


Figure 3.12. Upper layer thickness contours (left panel) and streamfunction contours (right panel) for the collision experiment E8 (Table 3.1) on a β -plane at day 2500. As before, the contour interval is 20 m for the upper layer depth and 15 Sv for the stream function. The axis marks are 10 grid points (75 km) apart. Area within closed contours are shaded. Recall that no eddies are produced in the f-plane case (see Fig. 5 in Lebedev and Nof 1997).

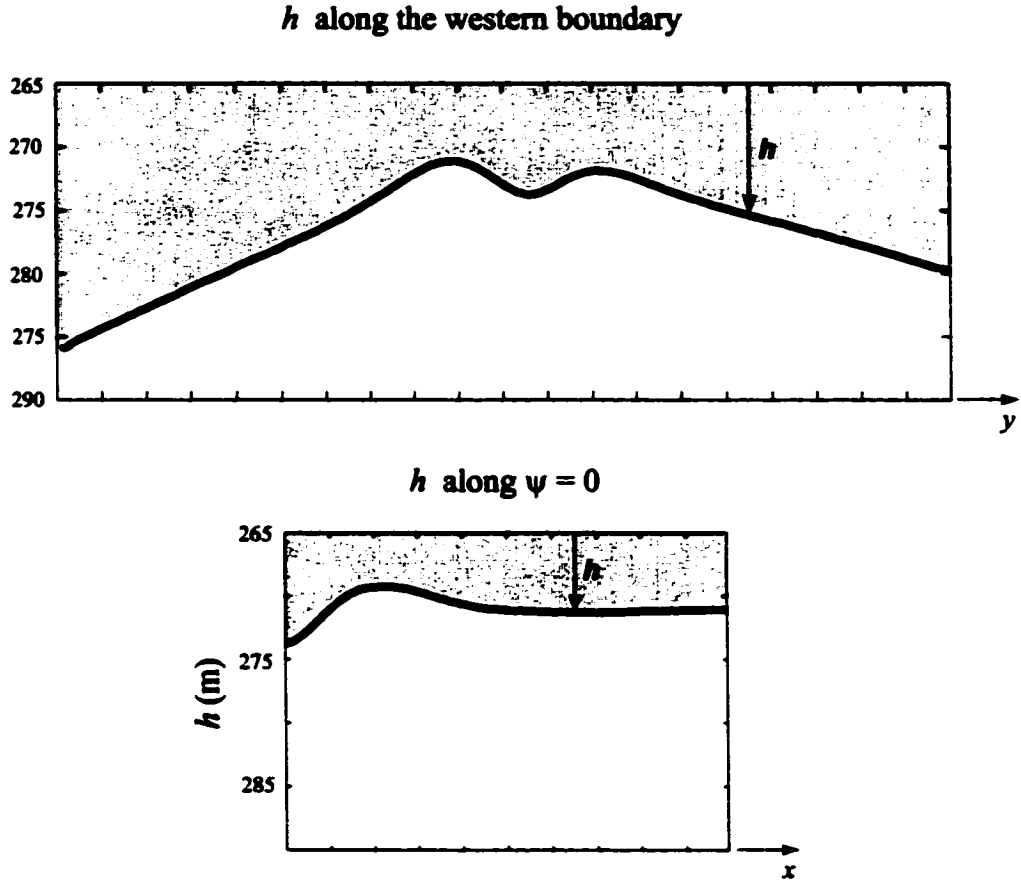


Figure 3.13. Upper layer thickness h (in meters) along the western boundary (upper panel) and along the offshore branch of $\psi = 0$ (lower panel) for the collision experiment E8 at day 2500.

6.5 Sv streamline as the boundary of the anticyclonic eddy (**Fig. 3.12**) we estimate (from the numerics) an average radius of $4.5 R_{dn}$ [where $R_{dn} = (g'H_n)^{1/2}/f_0$] and $3 R_{ds}$ [where $R_{ds} = (g'H_s)^{1/2}/f_0$]. These are in decent agreement with the analytical estimates [derived from (3.35) and (3.37)] of $3.35 R_{dn}$ and $2.84 R_{ds}$, respectively. Recall that these analytical estimates neglect the second term in (3.39) and (3.40).

In the next section we shall apply the theory of the collision of opposing flowing western boundary currents on a β -plane to the equatorial western Pacific. In this scenario, the South Equatorial Current is the “main current” and the Mindanao

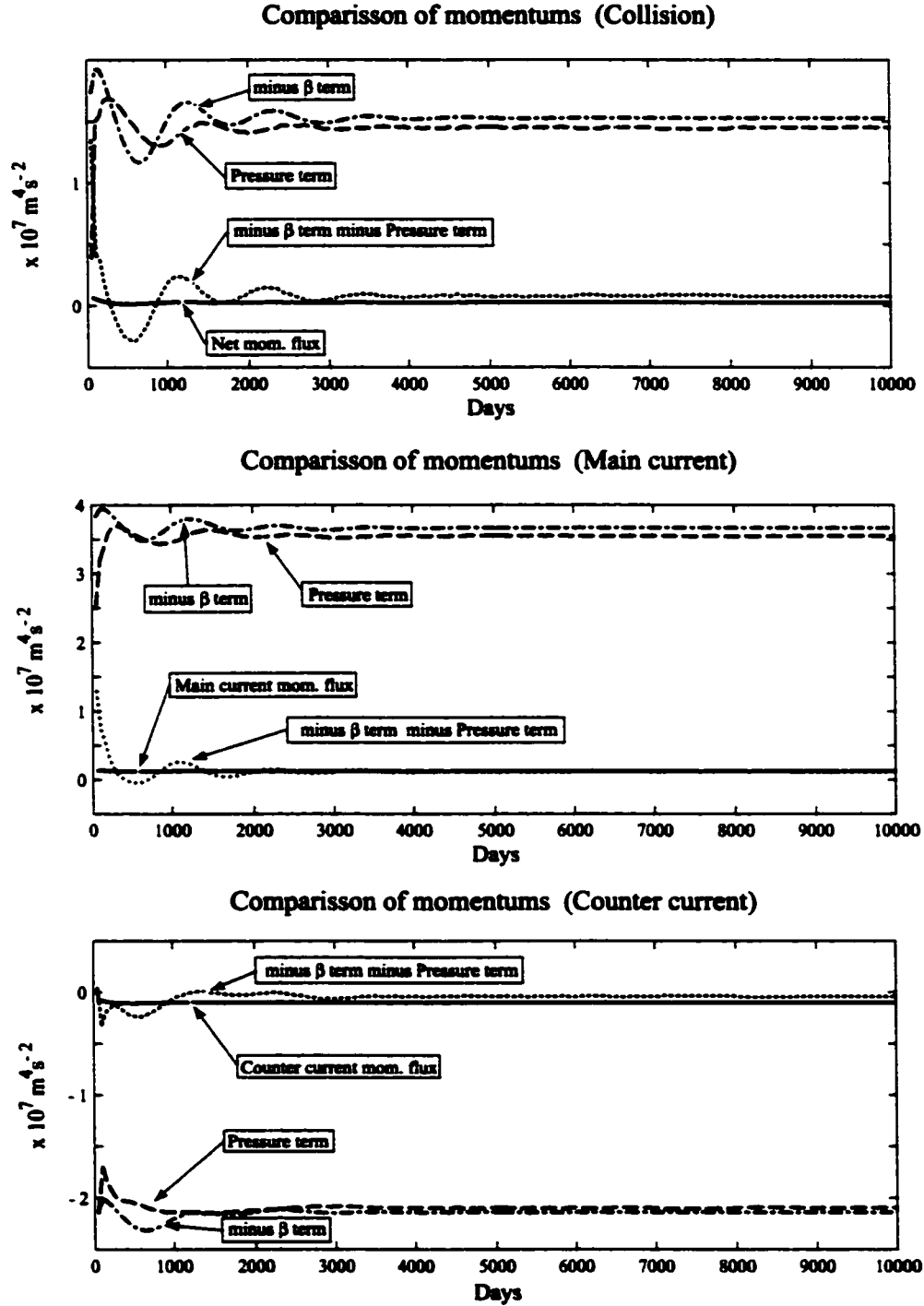


Figure 3.14. Momentum balance (3.38) for area containing both colliding currents (upper panel); Momentum balance (3.39) for the area south of the zero stream-function (middle panel); Momentum balance (3.40) for the area north of the zero streamfunction (lower panel). All terms were computed from experiment E8.

Current is the “counter current”. As is expected by now, the collision would lead to the formation of the cyclonic Mindanao eddy and the anticyclonic Halmahera eddy.

3.6 The Western Equatorial Pacific

Considering the scheme in **Fig. 3.15** showing the northward flowing SECC colliding with the southward flowing MC. Most of the fluid transported by the currents flows into the (eastward flowing) NECC and a small amount forms the ITF. (As we pointed out earlier even though the transport of the ITF is small its existence is essential for the establishment of the SEC.) The streamline $\psi = 0$ divides the amount of fluid in each current that flows into the NECC.

Considering the integration region bounded by $ABCD$ in **Fig. 3.15**, it is easily seen that the momentum balance for this situation follows immediately from the collision problem without the ITF. Note that the momentum fluxes of each one of the colliding currents must be calculated by considering only the part of each current that effectively flows into the NECC.

Since our main goal is to study the eddies, we use observed values for the total transports of the MC and SEC and the respective amounts flowing through the Indonesian passages in order to estimate H_0 . We take 26 Sv for the MC transport and 22 Sv for the SEC transport. Around 11 Sv from MC and 1 Sv from SEC flow into the ITF. Using the previously calculated values of the offshore upper layer thicknesses for the colliding currents ($H_n = 97.83$ m for the MC and $H_s = 235.32$ m for the SEC) we obtain $H_0 = 270$ m. Substituting the values of H_s , H_n , and H_0 into (3.35) and (3.37), we get a radius of $1.144 R_{d_n}$ for the Mindanao eddy (where $R_{d_n} = 110$ km and $\epsilon_n = 0.2$) and a radius of $1.52 R_{d_s}$ for the Halmahera eddy (where $R_{d_s} = 171$ km and $\epsilon_s = 0.3$). The estimated radius compares very well with the observations (Lukas et al. 1991; Kashino et al. 1999) of $1.136 R_{d_n}$ (175 km) for the Mindanao eddy and between $1.37 R_{d_s}$ and $1.46 R_{d_s}$ (between 235 and 250 km) for the Halmahera eddy.

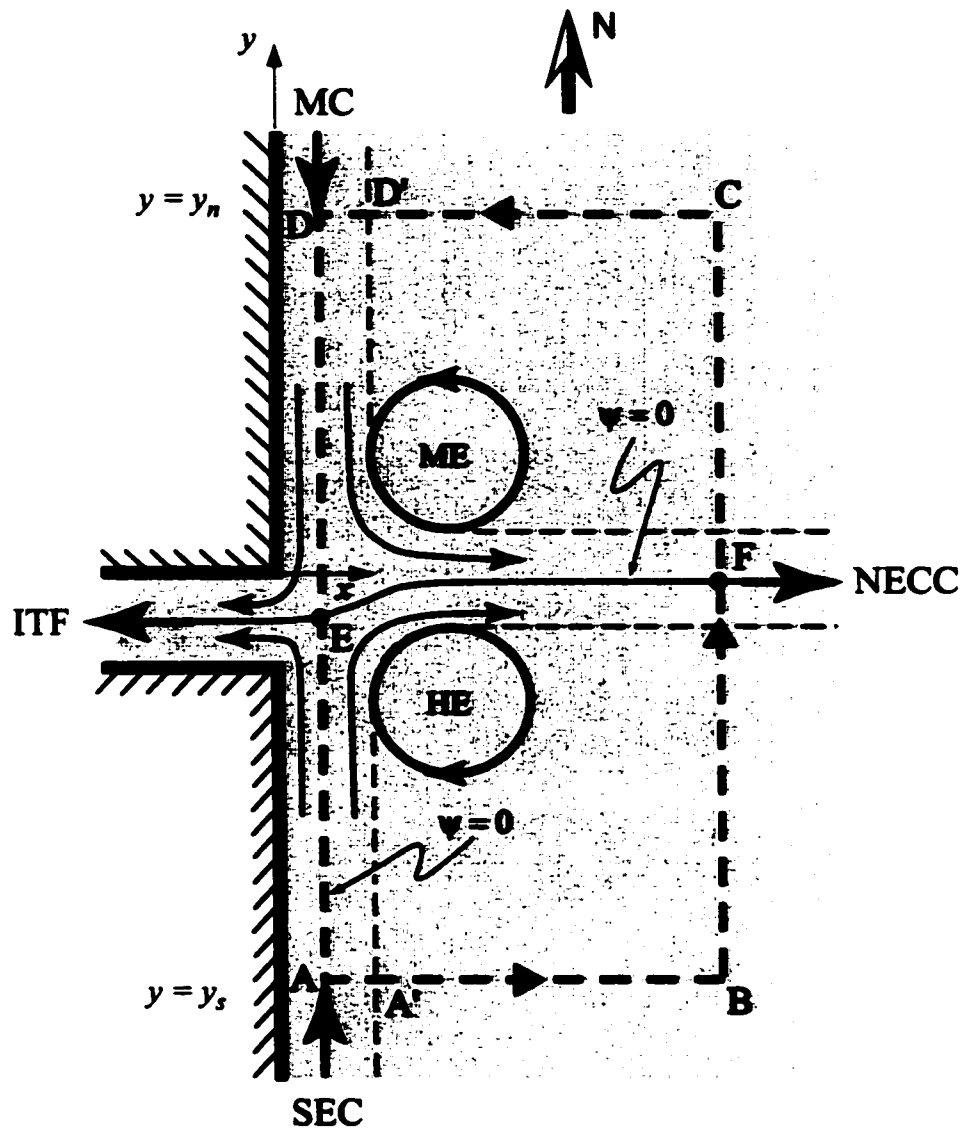


Figure 3.15. Schematic representation of the convergence of the Mindanao Current (MC) and South Equatorial Current (SEC). The currents collide such that most of the water transported from each current form the eastward flowing North Equatorial Counter Current (NECC) and a small part flows into the Indonesian throughflow. The area bounded by $ABCD$ is the integration region S and the segment AD is on the streamline $\psi = 0$. The portions of the MC and the SEC which effectively participate in the collision process are responsible for the formation of the Mindanao eddy (ME) and Halmahera eddy (HE). Point E is an stagnation point.

Because the value of H_s (235.32 m) and H_n (97.83 m) are estimated from the observed mean wind stress, we consider them good representatives of the mean thicknesses. Variations in the composition of the throughflow would, of course, lead to changes in H_0 , and consequently, to variations in the relative sizes of the eddies.

3.7 Conclusions

Figs. 3.4 and 3.7 are the most elucidating of our analysis because they highlight the profound difference between an f-plane and a β -plane flow in a concave solid corner. In the f-plane case there is no eddy and the flow is diagonally symmetric while in the β -plane case there is a lack of symmetry and a stationary eddy is attached to the curving flow. The momentum balance relations (3.10)-(3.13) for a nonlinear WBC in a concave solid corner shows that, on an f-plane, no eddy is necessary because a pressure force (produced by the difference between the upper layer thickness) balances the current's momentum flux. On a β -plane, on the other hand, the pressure force and the boundary current momentum force point in the same direction. Consequently, a permanent eddy is necessary to produce an opposing β -force leading to the required momentum balance. It is opportune to point out that the nonlinearities play a fundamental role in this theory because in the linear limit the boundary current momentum flux approaches zero [as well as the pressure force (since $\Delta H \sim H$)] so no eddy is established.

We expanded all the dependent variables in Taylor series of a small parameter around a basic state, and neglected the second term in (3.12) on the basis of the numerics. This provides a lower bound estimate on the radius of the anticyclonic eddy (3.35) formed when a northward flowing WBC turns in a concave solid corner,

$$R = 2 \left(\frac{2^{3/2}}{\pi} \right)^{1/6} \left(\frac{H - H_0}{H} \right)^{1/2} \left(\frac{H}{H - H_0} - \frac{3}{5} \right)^{1/6} \frac{R_d}{\epsilon^{1/6}}.$$

Similarly, we obtain a lower bound estimate for the cyclonic eddy (3.37) formed when a southward flowing WBC turns in a concave solid corner,

$$R = \left(\frac{1}{3\pi} \right)^{1/2} \left(\frac{H_0 - H}{H} \right) \left(\frac{H + 2H_0}{H} \right)^{1/2} \frac{R_d}{\epsilon^{1/2}}$$

These eddy radii estimates are in very good agreement with the ones obtained from the numerical experiments.

For the collision of opposing western boundary currents, we derive momentum balance relations (3.39-3.42) using the separating streamline as a divider between the integration domains. Comparison with numerical model simulations indicates that the nonlinear inviscid momentum balance for the solid corner also holds for the fluid collision problem (**Fig. 3.14**) and that the analytical estimates for the eddy radii in solid corners [(3.35) and (3.37)] are in good agreement with those of the numerical simulation of colliding currents.

Applying the collision theory for the Mindanao Current and South Equatorial Current in the western equatorial Pacific taking into account only the effective part of each current that participates in the collision process, we estimate [from (3.35) and (3.37)] a diameter of 252 km for the Mindanao eddy and 520 km for the Halmahera eddy. These are in excellent agreement with the observed values of 250 km and between 470 and 500 km (Lukas et al. 1991; Kashino et al. 1999). We also point out that, although the ITF plays a secondary role in our theory, its existence is essential for the formation of the cross equatorial flow of the SEC. Without the ITF there would be no collision and no eddies. Consequently, it is not surprising that variations in the ITF transport lead to variations of the relative sizes of the ME and the HE.

The above arguments shows that the physical mechanism proposed here (i.e., that eddies are necessary to balance the momentum flux of their parent currents, the

southward flowing Mindanao Current and the northward flowing South Equatorial Current) are responsible for the formation of the Mindanao and Halmahera eddies.

CHAPTER 4

CONCLUSIONS

We have presented two self-contained studies for eddies along western boundaries. In Chapter 1 we presented a nonlinear theory for the generation of the Ulleung Warm eddy (UWE). It was shown that the UWE was established in order to balance the northward momentum flux exerted by the separating East Korea Warm Current. Consequently, the UWE formation is not due to instabilities, instead it is an integral part of the steady stable solution. In Chapter 2 we presented a nonlinear theory for the generation of the Mindanao and Halmahera eddies associated with the collision of the southward flowing Mindanao Current and the northward flowing South Equatorial Current in the western equatorial Pacific. It was shown that these eddies are established in order to balance the momentum fluxes exerted by their colliding parent currents. In both chapters analytical eddy radius estimates were derived. These estimates compared very well with the observed eddy radius.

APPENDIX

LIST OF SYMBOLS AND ACRONYMS

B	Bernoulli function, $g'h + (u^2 + v^2)/2$
f	Coriolis parameter ($f_0 + \beta y$)
g'	Reduced gravity, $g\Delta\rho/\rho$
h	Upper layer thickness
h_e	Eddy upper layer thickness
H	Interior upper layer thickness at a fixed latitude
H_0	Upper layer thickness on the zonal wall as $x \rightarrow \infty$ (Fig. 3.3)
H_e	Upper layer thickness at the eddy center
H_{max}	Upper layer thickness at the corner (Fig. 3.3)
H_n, H_s	Upper layer thicknesses at fixed latitudes in the counter current side and main current side (Fig. 3.11)
K_0, K_1	Bessel functions of the first kind
L	Boundary current width (Figs. 2.4 and 2.10)
L_2	Width of square domain S (Fig. 2.4 and 3.2)
L_e	Basin zonal width (Fig. 2.10)
L_n	Counter current width (Fig. 3.11)
L_s	Main current width (Fig. 3.11)
Q	Boundary current transport
R	Eddy radius
R_1	Parameter defined as $8(g'H_e)^{1/2}/f_0$
R_0	Radius of the outcropped region in the cyclonic eddy (Fig. 3.10)

R_d	Rossby radius of deformation, $(g'H)^{1/2}/f_0$
R_{dn}	Rossby radius of deformation, $(g'H_n)^{1/2}/f_0$
R_{ds}	Rossby radius of deformation, $(g'H_s)^{1/2}/f_0$
R_{de}	Rossby deformation radius of the eddy, $(g'H_e)^{1/2}/f_0$
S	Integration area bounded by dashed rectangle in Figs. 2.4, 2.10, and 3.2,
S^+, S^-	Subsets of S such that $y \geq 0$ and $y \leq 0$ respectively
u, v	Velocity components in Cartesian coordinates
\bar{v}	Current's mean speed
v_θ	Orbital velocity in the eddy
y_s, y_n	Latitudes of the southern and northern boundaries of S (Figs. 2.4, 2.10, 3.2, and 3.11)
x_B	x -coordinate of point B in Fig. 2.10
β	Variation of the Coriolis parameter with latitude
ϵ	Small parameter equal to $\beta R_d/f_0$
ϕ	Cartesian representation of the dividing streamline in the collision problem
$\rho, \Delta\rho$	Density and density difference between the layers
ν	Viscosity coefficient
κ	Coefficient of interfacial friction
ψ	Streamfunction (defined by $\psi_y = -uh$; $\psi_x = vh$)
ψ_∞	Limit of ψ as $x \rightarrow \infty$
$\hat{\psi}$	$\psi - \psi_\infty$
ψ_e	Eddy stream function
τ^x	Zonal component of the wind stress
ADCP	Acoustic Doppler Current Profiler
EKWC	East Korea Warm Current
HE	Halmahera eddy
ITF	Indonesian throughflow

JES	Japan/East Sea
ME	Mindanao eddy
NKCC	North Korea Cold Current
NECC	North Equatorial Counter Current
NGCC	New Guinea Coastal Current
NGCUC	New Guinea Coastal Undercurrent
SEC	South Equatorial Current
TWC	Tsushima Warm Current
UWE	Ulleung Warm Eddy
WBC	Western Boundary Current

REFERENCES

- [1] Agra, C., and D. Nof, 1993: Collision and separation of boundary currents. *Deep Sea Res.*, **40**, 2259-2282.
- [2] Anderson, D. L. T., and D. W. Moore, 1979: Cross-equatorial inertial jets with special relevance to very remote forcing of the Somali Current, *Deep-Sea Res.*, **26**, 1-22.
- [3] Arakawa, A., 1966: Computational design for long-term numerical integration of the equations of fluid motion. Two dimensional incompressible flow. Part 1. *J. Comput. Phys.*, **1** 119-143.
- [4] Aung, T. H., 1998: Indo-Pacific throughflow and its seasonal variations. In *The ASEAN-Australia Regional Ocean Dynamics Expeditions 1993-1995. Proceedings held in Lombok, Indonesia, June 1995.* Eds. G. Cresswell and G. Wells, Australian Marine Science and Technology, pp. 199-214.
- [5] Bleck, R., and D. Boudra, 1981: Initial test of a numerical ocean circulation model using a hybrid, quasi-isopycnic vertical coordinate. *J. Phys. Oceanogr.*, **11**, 755-770.
- [6] Bleck, R., and D. Boudra, 1986: Wind-driven spin-up in eddy-resolving ocean models formulated in isopycnic and isobaric coordinates. *J. Geophys. Res.*, **91**, 7611-7621.
- [7] Bleck, R., and L. Smith, 1990: A wind-driven isopycnic coordinate model of the north and equatorial Atlantic Ocean. Part I: Model development and supporting experiments. *J. Geophys. Res.*, **95**, 3273-3285.
- [8] Boris, J., and D. Book, 1973: Flux-corrected transport, I: SHASTA, a fluid transport algorithm that works. *J. Comput. Phys.*, **11**, 38-69.
- [9] Cannon, G. A., 1970: Characteristics of waters east of Mindanao, Philippine Islands, August 1965. In *The Kuroshio, A Symposium on the Japan Current*, ed. J. C. Marr, East-West Center Press, Honolulu, Hawaii, pp. 205-211.
- [10] Cantos-Figuerola, A., and B. A. Taft, 1983: The South Equatorial Current during 1979-80 Hawaii-Tahiti Shuttle. *Trop. Ocean. Atmos. Newslett.*, **19**, 6-8.

- [11] Cho, Y.-K., and K. Kim, 1996: Seasonal variation of the East Korea Warm Current and its relation with the cold water. *La Mer*, **34**, 172-182.
- [12] Chu, P. C., J. Lan, and C. W. Fan, 2001: Japan Sea circulation and thermohaline structure, Part 1, Climatology. *J. Phys. Oceanogr.*, **31**, 244-271.
- [13] Collin, C., C. Henin, P. Hisard, and C. Oudot, 1971: Le Courant de Cromwell dans le Pacifique central f/'evier, *Cah. O.R.S.T.O.M., Ser. Oceanogr.*, **9**, 724-738.
- [14] Cox, M. D., 1975: A baroclinic numerical model of the word ocean: Preliminary results. In, *Numerical Models of Ocean Circulation*, pp. 107-120, Natl. Acad. of Sci., Washington, D. C.
- [15] Cresswell, G., A. Frische, J. Peterson, and D. Quadfasel, 1993: Circulation in the Timor Sea. *J. Geophys. Res.*, **98**, 14379-14389.
- [16] Dengg, J., A. Beckmann, and R. Gerdes, 1996: The Gulf Stream Separation Problem. In *Warmwatersphere of North Atlantic Ocean*, W. Krauss (ed.), Gebr. Bornträger, Sttutgard, pp. 253-290.
- [17] Ffield, A., and A. L. Gordon, 1992: Vertical mixing in the Indonesian thermocline. *J. Phys. Oceanogr.*, **22**, 184-195.
- [18] Fieux, M., C. Andri/'e, P. Delecluse, A. G. Ilahude, A. Kartavtseff, F. Mantisi, R. Molcard, and J. C. Swallow, 1994: Measurements within the Pacific-Indian oceans throughflow region. *Deep-Sea Res.*, **41**, 1091-1130.
- [19] Fine, R., 1985: Direct evidence using tritium data for throughflow from the Pacific into Indian Ocean. *Nature*, **315**, 478-480.
- [20] Fine, R., R. Lukas, F. Bingham, M. J. Warner, and R. H. Gammon, 1994: The western equatorial Pacific: A water mass crossroads. *J. Geophys. Res.*, **99**, 25063-25080.
- [21] Fu, L., 1986: Mass, heat ans freshwater fluxes in the South Indian Ocean. *J. Phys. Oceanogr.*, **16**, 1683-1693.
- [22] Godfrey, J. S., 1989: A Sverdrup model of the depth-integrated flow for the world ocean allowing for island circulations. *Geophys. Astrophys. Fluid. Dyn.*, **45**, 89-112.
- [23] Godfrey, J. S., and T. J. Golding, 1981: The Sverdrup relation in the Indian Ocean, and the effect of Pacific-Indian Ocean throughflow on Indian Ocean circulation and on the East Autralian Current, *J. Phys. Oceanogr.*, **11**, 771-779.

- [24] Godfrey, J. S., A. C. Hirst, and J. Wilkin, 1993: Why does the Indonesian Throughflow appear originate from North Pacific? *J. Phys. Oceanogr.*, **23**, 1087-1098.
- [25] Gordon, A. L., 1986: Inter-ocean exchange of thermocline water. *J. Geophys. Res.*, **91**, 5037-5050.
- [26] Gordon, A. L., 1990: Sea of Japan. In *Marginal Seas and the Kuroshio: An Assessment of Mutual Impact*, Department of Oceanography, Florida State University, Tallahassee, Fla.
- [27] Gordon, A. L., 1995: When is "appearance" reality? Indonesian throughflow is primarily derived from North Pacific water masses. *J. Phys. Oceanogr.*, **25**, 1560-1567.
- [28] Gordon, A. L., R. D. Susanto, and A. L. Field, 1999: Throughflow within Makassar Strait, *Geophys. Res. Lett.*, **26**, 3325-3328.
- [29] Gouriou, Y., and J. Toole, 1993: Mean Circulation of the Upper Layers of the Western Equatorial Pacific Ocean. *J. Geophys. Res.*, **98**, 22495-22520.
- [30] Hellerman, S., and M. Rosenstein, 1983: Normal monthly wind stress over the world ocean with error estimates. *J. Phys. Oceanogr.*, **13**, 1093-1104.
- [31] Hirst, A. C., and J. S. Godfrey, 1993: The role of the Indonesian throughflow in the global ocean GCM. *J. Phys. Oceanogr.*, **23**, 1057-1086.
- [32] Hogan, P. J., and H. Hurlburt, 2000: Impact of upper ocean-topographical coupling and isopycnal outcropping in Japan/East Sea models with $1/8^\circ$ to $1/64^\circ$ resolution. *J. Phys. Oceanogr.*, **30**, 2535-2561.
- [33] Huang, R. X., and G. R. Flierl, 1987: Two-layer models for the thermocline and current structure in subtropical/subpolar gyres. *J. Phys. Oceanogr.*, **17**, 872-884.
- [34] Ichiye, T., and K. Takano, 1988: Mesoscale eddies in the Sea of Japan. *La Mer*, **26**, 69-79.
- [35] Inoue M., and S. E. Welsh, 1993: Modeling seasonal variability in the wind-driven upper-layer circulation in the Indo-Pacific region. *J. Phys. Oceanogr.*, **23**, 1411-1436.
- [36] Isoda, Y., and M. Nishihara, 1992: Behavior of warm eddies in the Japan Sea. *Umi to Sora*, **67** (Spec. Issue), 231-243.
- [37] Isoda, Y., and S.-I. Saitoh, 1993: The northward intruding eddy along coast of Korea. *J. Oceanogr.*, **49**, 443-458.

- [38] Jacobs, G. A., H. T. Perkins, W. J. Teague and P. J. Hogan, 2001: Summer transport through the Tsushima-Korea Strait. *J. Geophys. Res.*, **106**, 6917-6829.
- [39] Kang, H. E., and Y. Q. Kang, 1990: Spatio-temporal characteristics of the Ulleung Warm Lens. *Bull. Korean Fish. Soc.*, **203**, 407-415.
- [40] Kashino, Y., H. Watanabe, B. Herunadi, M. Aoyama, and D. Hartoyo, 1999: Current variability at the Pacific entrance if the Indonesian Throughflow. *J. Geophys. Res.*, **104**, 11021-11035.
- [41] Katoh, O., 1994: Structure of the Tsushima Current in the southwestern Japan Sea. *J. Oceanogr.*, **50**, 317-338.
- [42] Kawabe, M., 1982a: Branching of Tsushima Current in the Japan Sea. Part I. Data Analysis. *J. Oceanogr. Soc. Japan*, **38**, 95-107.
- [43] Kawabe, M., 1982b: Branching of Tsushima Current in the Japan Sea. Part II. Numerical experiment. *J. Oceanogr. Soc. Japan*, **38**, 183-192.
- [44] Kendall, T. R., 1969: Net transports in the western equatorial Pacific Ocean. *J. Geophys. Res.*, **74**, 1388-1369.
- [45] Kessler, W. S., and B. A. Taft, 1987: Dynamic heights and zonal geostrophic transports in the central Pacific during 1979-1984. *J. Phys. Oceanogr.*, **7**, 97-122.
- [46] Killworth, P. D., 1983: On the motion of isolated lenses on a beta-plane. *J. Phys. Oceanogr.*, **13**, 368-376.
- [47] Kim, C. H., and K. Kim, 1983: Characteristics and origin of the cold water mass along the east coast of Korea. *J. Oceanol. Soc. Korea*, **18**, 73-83.
- [48] Kim, K., and R. Legeckis, 1986: Branching of the Tsushima Current in 1981-83. *Prog. Oceanogr.*, **17**, 265-276.
- [49] Kim, K., K.-R. Kim, J. Chung, H. Yoo, and S. Park, 1991: Characteristics of physical properties in the Ulleung Basin. *J. Oceanol. Soc. Korea*, **26**, 83-100.
- [50] Kindle, J. C., G. W. Heburn, and R. C. Rhodes, 1987: An estimate of the Pacific to Indian throughflow from a global numerical model. In *Further Progress in Equatorial Oceanography*, eds. E. J. Katz and J. M. Witte, pp. 317-321, Nova Univ. Press, Fort Lauderdale, Fla.
- [51] Kindle, J. C., H. E. Hurlburt, and E. J. Metzger, 1989: On the seasonal and interannual variability of the Pacific to Indian Ocean throughflow, paper presented at Western Pacific International Meeting and Workshop on TOGA COARE, Inst. Fr. de Rech. Sci. pour le Dev. en coop., (ORSTOM), Nouméa, New Caledonia.

- [52] Kundu, P. K., 1990: *Fluid Mechanics*. Academic Press, 638 pp.
- [53] Lebedev, I., and D. Nof, 1997: Collision of boundary currents: beyond a steady state. *Deep-Sea Res. I*, **44**, 771-791.
- [54] Lie, H.-J., 1984: Coastal current and its variation along the east coast of Korea. In *Ocean Hydrodynamics of the Japan and East China Seas*, T. Ichiye ed., Elsevier, Amsterdam, pp. 399-408.
- [55] Lie, H.-J., and S.-K. Byun, 1985: Summertime southward current along the east coast of Korea. *J. Oceanol. Soc. Korea*, **20**, 22-27.
- [56] Lie, H.-J., S.-K. Byun, I. Bang, and C.-H. Cho, 1995: Physical structure of eddies in the southwestern East Sea. *J. Korean Soc. Oceanogr.*, **30**, 170-183.
- [57] Lim, B., and K. Kim, 1995: A numerical study on the interaction of Ulleung Warm Eddy with topography and lateral boundary. *J. Oceanol. Soc. Korea.*, **30**, 565-583.
- [58] Lukas, R., E. Firing, P. Hacker, P. L. Richardson, C. A. Collins, R. Fine, and R. Gammon, 1991: Observations of the Mindanao Current During the Western Equatorial Pacific Ocean Circulation Experiment Study. *J. Geophys. Res.*, **96**, 7089-7104.
- [59] Masuzawa, J., 1968: Second cruise for CSK, Ryofu Maru, January to March 1968. *Oceanogr. Mag.*, **20**, 173-185.
- [60] Masuzawa, J., 1969: The Mindanao Current. *Bull. Jpn. Soc. Fish. Oceanogr.*, 99-104.
- [61] Matsuyama, M., Y. Kurita, T. Senjyu, Y. Koike, and T. Hayashi, 1990: The warm eddy observed east of Oki Islands in the Japan Sea (2). *Umi to Sora*, **66**, 67-75.
- [62] Meyers, G., R. J. Bailey, and A. P. Worby, 1995: Geostrophic transport of Indonesian Throughflow, *Deep-Sea Res.*, Part I, **42**, 1163-1174.
- [63] Miyao, T., 1994: The fractal dimension analysis applied to eddies in the Sea of Japan. *Oceanogr. Mag.*, **44**, 13-30.
- [64] Molcard, R., M. Fieux, and F. Syamsudin, 2001: The throughflow within Ombai Strait, *Deep-Sea Res.*, Part I, **48**, 1237-1253.
- [65] Murray, S. P., and D. Arief, 1988: Throughflow into the Indian Ocean through the Lombok Strait, January 1985-January 1986. *Nature*, **333**, 444-447.

- [66] Murray, S. P., and D. Arief, J. C. Kindle and H. E. Hurlburt, 1990: Characteristics of circulation in an Indonesian Archipelago strait from Hydrography, current measurements and modelling results, In: *The Physical Oceanography of Sea Straits*, ed. L. J. Pratt, 129-163.
- [67] Nof, D., 1981: On the dynamics of equatorial outflows with application to Amazon's basin. *J. Mar. Res.*, **39**, 1-29.
- [68] Nof, D., 1995a: Choked flows and wind-driven interbasin exchange, *J. Mar. Res.*, **53**, 23-48.
- [69] Nof, D., 1995b: Choked flows from Pacific to Indian Ocean, *J. Phys. Oceanogr.*, **25**, 1369-1383.
- [70] Nof, D., 1996: What controls the origin of the Indonesian throughflow? *J. Geophys. Res.*, **101**, 12301-12314.
- [71] Nof, D., and T. Pichevin, 1999: The establishment of the Tsugaru and the Alboran Gyres. *J. Phys. Oceanogr.*, **29**, 39-54.
- [72] Nof, D., and T. Pichevin, 2001: The ballooning outflows. *J. Phys. Oceanogr.*, **31**, 3045-3058.
- [73] Olson, D. B., 1991: Rings in the ocean. *Annu. Rev. Earth Planet. Sci.*, **19**, 283-311.
- [74] Orlanski, I., 1976: A simple boundary condition for unbounded hyperbolic flows. *J. Comput. Phys.*, **21**, 251-269.
- [75] Ou, H. S., 2001: A model of buoyant throughflow: With application to branching of the Tsushima Current. *J. Phys. Oceanogr.*, **31**, 115-126.
- [76] Parsons, A. T., 1969: A two-layer model for Gulf Stream separation. *J. Fluid Mech.*, **39**, 511-528.
- [77] Perkins, H., W. J. Teague, G. A. Jacobs, K. I. Change, and M.-S. Suk, 2000: Currents in Korea-Tsushima Strait during summer 1999: *Geophys. Res. Lett.*, **27**, 3033-3036.
- [78] Pichevin, T., and D. Nof, 1997: The momentum imbalance paradox. *Tellus*, **49A**, 298-319.
- [79] Piola, A. R., and A. L. Gordon, 1984: Pacific and Indian Ocean upper-layer salinity budget. *J. Phys. Oceanogr.*, **14**, 747-753.

- [80] Preller, R., and P. Hogan, 1998: Oceanography of the Sea of Okhotsk and the Japan/East Sea coastal segment. In *The Sea 11*, ed. A. Robinson and K. Brink, John Willey and Sons, pp. 429-481.
- [81] Qu, T., H. Mitsudera, and T. Yamagata, 1999: A Climatology of the Circulation and Water Mass Distribution near the Philippine Coast. *J. Phys. Oceanogr.*, **29**, 1488-1505.
- [82] Ramp, S. R., F. L. Bahr, C. J. Ashjian, and L. D. Talley, 2002: The Upper-Ocean Circulation in the Ulleung Basin During June-July 1999, submitted to *Deep-Sea Research II*.
- [83] Rostov, I., G. I. Yurasov, N. I. Rudyh, V. V. Moroz, E. V. Dmitreva, A. A. Nabiullin, F. F. Khrapchenkov and V. M. Bunim, 2001: Oceanographic Atlas of Bering Sea, Okhotsk Sea, and Japan/East Sea. CD-ROM, POI FEBRAS, Vladivostok, Russia.
- [84] Semter, A. J., and R. M. Chevin, 1988: A simulation of the global ocean circulation with resolved eddies. *J. Geophys. Res.*, **93**, 15502-15552.
- [85] Semter, A. J., and R. M. Chevin, 1992: Ocean general circulation from a general eddy-resolving model. *J. Geophys. Res.*, **97**, 5493-5550.
- [86] Sprintall, J., S. Wijffels, T. Chereskin, and N. Bray, 2002: The JADE and WOCE 110/IR6 Throughflow sections in the southeastern Indian Ocean, Part 2: velocity and transports. *Deep-Sea Res.*, Part II, **49**, 1363-1389.
- [87] Suda, K., and K. Hidaka, 1932: The results of the oceanographical observations on board R.M.S. Syunpu Maru in the southern part of the Sea of Japan in the summer of 1929, part I. *J. Oceanogr. Imp. Mar. Observ.*, **3**, 291-375 (in Japanese).
- [88] Sugimoto, T., and H. Tameishi, 1992: Warm-core rings, streamers and their role on the fishing ground formation around Japan. *Deep-Sea Res. I*, **39** (Suppl. 1), S183-S201.
- [89] Takahashi, T., 1959: Hydrographical researches in the western equatorial Pacific. *Mem. Faculty Fish. Kagoshima Univ.*, **7**, 141-147.
- [90] Tameishi, H., 1987: Applications of NOAA/AVHRR images to fisheries around Tsushima Strait. *Bull. Fish. Oceanogr.*, **51**, 238-244.
- [91] Tanioka, K., 1968: On the East Korean Warm Current (Tosen Warm Current). *Oceanogr. Mag.*, **20**, 31-38.

- [92] Toba, T., K. Tomizaga, Y. Kurasawa, and K. Hanawa, 1982: Seasonal and year to year variability of the Tsushima-Tsugaru Currents system with its possible cause. *La Mer*, **20**, 41-51.
- [93] Toole, J. M., E. Zou, and R. C. Millard, 1988: On the circulation of the upper waters in the western equatorial Pacific Ocean. *Deep Sea Res.*, **35**, 1451-1482.
- [94] Toole J. M., R. C. Millard, Z. Wang, and S. Pu, 1990: Observations of the Pacific North Equatorial Current Bifurcation at the Philippine Coast. *J. Phys. Oceanogr.*, **20**, 307-318.
- [95] Tsuchiya, M., R. Lukas, R. Fine, E. Firing, and E. Lindstrom, 1989: Source waters of Pacific Equatorial Undercurrent. *Progr. Oceanogr.*, **23**, 101-147.
- [96] Uda, M., 1934: The results of simultaneous oceanographical investigations in the Japan Sea and its adjacent waters in May and June 1932. *J. Imp. Fish. Exp. Stn.*, **5**, 57-190 (in Japanese).
- [97] Veronis, G., 1973: Model of world ocean circulation: I. Wind driven, two-layer. *J. Mar. Res.*, **31**, 228-288.
- [98] Wajsowicz, R. C., 1993a: The circulation of the depth-integrated flow around an island with application to the Indonesian throughflow. *J. Phys. Oceanogr.*, **23**, 1470-1484.
- [99] Wajsowicz, R. C., 1993b: A simple model of the Indonesian throughflow and its composition. *J. Phys. Oceanogr.*, **23**, 2683-2703.
- [100] Wajsowicz, R. C., 1999: Variations in Gyre Closure at the Water Mass Crossroads of the Western Equatorial Pacific Ocean. *J. Phys. Oceanogr.*, **29**, 3002-3024.
- [101] Waworuntu, J., 1999: Water mass transformations and throughflow variability on the Indonesian seas. Ph.D. dissertation, 98 pp., University of Miami, Miami, Fla.
- [102] Waworuntu, J., R. Fine, D. B. Olson, and A. L. Gordon, 2000: Recipe for Banda Sea water. *J. Mar. Res.*, **58**, 547-569.
- [103] Waworuntu, J., S. L. Garzoli, and D. B. Olson, 2001: Dynamics of the Makassar Strait. *J. Mar. Res.*, **59**, 313-325.
- [104] Webster, P. J., and R. Lukas, 1992: The Tropical Ocean/Global Atmosphere Coupled Ocean Atmosphere Response Experiment (COARE). *Bull. Amer. Meteor. Soc.*, **73**, 1377-1416.

- [105] Wijffels, S. E., 1993: Exchanges between hemispheres and gyres: A direct approach to the mean circulation of equatorial Pacific, Ph.D. dissertation, 267 pp., Woods Hole Oceanogr. Inst., Woods Hole, Mass.
- [106] Wijffels, S. E., E. Firing, and J. Toole, 1995: The mean structure and variability of the Mindanao Current at 8°N. *J. Geophys. Res.*, **100**, 18421-18435.
- [107] Wijffels, S. E., J. Sprintall, M. Fieux and N. Bray, 2002: The JADE and WOCE 110/IR6 Throughflow sections in the southeastern Indian Ocean, Part 1: water mass distribution and variability. *Deep-Sea Res. II*, **49**, 1341-1363.
- [108] Wyrtki, K., 1956: The subtropical lower water between the Philippines and Iran (New Guinea). *Mar. Res. Indonesia*, **1**, 21-52.
- [109] Wyrtki, K., 1961: Physical oceanography of the southeast Asian waters. *Naga Rep.*, **2**, 195 pp.
- [110] Wyrtki, K., and B. Kilonsky, 1984: Mean water and current structure during Hawaii-to-Tahiti Shuttle Experiment. *J. Phys. Oceanogr.*, **14**, 242-254.
- [111] Zalesak, S. T., 1979: Fully multidimensional flux-corrected transport algorithms for fluids. *J. Comput. Phys.*, **31**, 335-362.

BIOGRAPHICAL SKETCH

Wilton Zumpichiatti Arruda

Wilton Zumpichiatti Arruda was born in Rio de Janeiro, Brazil on February 4, 1966. Wilton graduated with a B.A. in computer science (Universidade Federal do Rio de Janeiro) in 1990, with a M.S. in mathematics (Universidade Federal do Rio de Janeiro) in 1991, and with Ph.D. in mathematics (Universidade Federal do Rio de Janeiro) in 1996. In June, 1995 Wilton started as a professor in the Department of Mathematics, Universidade Federal do Rio de Janeiro. In January, 1998 was awarded with a scholarship from the brazilian government to pursuit the Ph.D. in physical oceanography at Florida State University.

Publications:

Arruda, W. Z., and R. Cipelatti, 1999: On the existence and regularity of ground states for a nonlinear system of coupled Schrödinger equations in R^N , *Comput. Appl. Math.*, **18**, 15-29.

Arruda, W. Z., and R. Cipelatti, 2000: Orbitally stable standing waves for a system of coupled nonlinear Schrödinger equations. *Nonlinear Anal-Theor.*, **42**, 445-461.

Arruda, W. Z., D. Nof, and J. J. O'Brien, 2002: The Ulleung eddy owes its existence to nonlinearities and β . *Submitted to Deep-Sea Res. II*.

Arruda, W. Z., and D. Nof, 2002: The Mindanao and Halmahera eddies are due to the bending of their parent currents, nonlinearities and β . *Submitted to J. of Phys. Oceanogr.*